2007

Numerical simulation of steady state and transient heat transfer in microchannels

Phaninder Injeti
University of South Florida

Numerical Simulation of Steady State and Transient Heat Transfer in Microchannels

by

Phaninder Injeti

A thesis submitted in partial fulfillment
of the requirements for the degree of
Master of Science in Mechanical Engineering
Department of Mechanical Engineering
College of Engineering
University of South Florida

Major Professor: Muhammad Mustafizur Rahman, Ph.D.
Autar K Kaw, Ph.D.
Frank Pyrtle, III, Ph.D.

Date of Approval:
July 13th 2007

Keywords: microtubes, protrusions, laminar flow, flow restrictions, magnetic refrigeration

Dedication

To my Parents for their support and patience. To my Friends for their untiring help and belief.

Acknowledgements

I would like to thank Dr. Rahman for his guidance, support, belief, and patience. I also would like to thank the committee members and faculty members of the Mechanical Engineering Department at the University of South Florida for their teaching and support. I also would like to thank my colleagues who worked with me under Dr. Rahman's supervision for their cooperation and help. Last but not the least would like to thank my friends Hari Patel, Apurva Panchal, Shivali Vyas, Saurabh Jagirdar, John Daly, Daniel Vilcius, Cesar Hernadez and Shon Ho for their enormous support in every way.

Table of Contents

List of Figures

List of Nomenclature

B	Channel height, m
b	Width of rectangular or triangular restriction, m
bc	Width of semicircular restriction, m
C_p	Constant pressure specific heat, J/kg-K
C_Q	Dimensionless pumping power, $(P_{in}–P_{out})Q/\rho(v_{in})^3(2B)^2$
D	Tube diameter, m
d	Half of diameter of the tube or height of the channel at the peak of restriction, m
e	Height of the restriction, m
g_0	Heat generation rate within the solid, W/m^3
G	Magnetic Field, Tesla
H_{fl}	Height of fluid, m
H_{gd}	Height of gadolinium slab, m
H_{si}	Half of distance between channels, m
k	Thermal conductivity, W/m-K
L	Tube or channel length, m
Nu	Local peripheral average Nusselt number, (q"w D)/(k (Tw-Tb))[tube],(2q"w B)/(k (Tw-Tb))[channel]
P	Pressure, N/m^2

Pr	Prandtl number, ν/α
q”	Heat flux, W/m^2
Q	Volume flow rate, m^3/s
Re	Reynolds number, $(w_{in}D)/\nu)$[tube],$(2w_{in}B)/\nu)$[channel]
r	Radial coordinate, m
t	Time, Sec
T	Temperature, ^oC
u	Velocity in x-direction, m/s
v	Velocity in the vertical direction, m/s
v_r	Velocity in the radial direction, m/s
w	Velocity in the horizontal direction, m/s
y	Vertical coordinate, m
z	Axial coordinate, m

Greek symbols

α	Thermal diffusivity, $k/ (\rho C_p)$, m^2/s
μ	Dynamic viscosity, Kg/m-s
ν	Kinematic viscosity, m^2/s
ξ	Length along the wall, m
ρ	Density, kg/m^3

Subscripts

avg	Average value
b	Bulk

g	Gadolinium
in	Inlet
out	Outlet
s	Silicon
w	Wall

Numerical Simulation of Steady State and Transient Heat Transfer in Microchannels

Phaninder Injeti

ABSTRACT

In this project we studied the effect of different parameters on heat transfer in two-dimensional microchannels, microtubes and also tube-in-block heat exchangers for various engineering applications. These included the use of flow restrictions to enhance local heat or mass transfer rate, enhancement of conjugate heat transfer with discrete heating and magnetic coolers (or heaters) associated with magnetic refrigeration system. The results of this research will help in designing the heating or cooling systems and selection of their appropriate geometrical dimensions and materials for specific applications. Types of problems studied in this project are: steady state analysis of forced convection around a restricted flow passage in a micro channel, effect of protrusions in a microtube or microchannel for conjugate heat transfer with uniform or discrete heating and transient analysis of heat transfer in trapezoidal microchannels under time varying heat source. For each of these problems a numerical simulation model was developed. The mass, momentum, and energy conservation equations were solved in the fluid region and energy conservation in the sold region to arrive at the velocity and the temperature distributions. Detailed parametric study was carried out for each problem. The parameters were shape and size of the restriction/protrusion, number of restrictions/protrusions, wall thickness, Reynolds number, solid materials and working fluids. The results showed that

in microtubes the local value of Nusselt number increases at the restriction/protrusion and the global value for the whole tube is somewhat lower. For a two-dimensional microchannel, both the local Nusselt number at the restriction/protrusion as well as the global Nusselt number for the entire channel is higher. In the trapezoidal channels the results showed that with the increase in Reynolds number, the outlet temperature decreased and the average heat transfer coefficient increased. With an increase in magnetic field there was an increase in the solid fluid interface temperature and in turn the average heat transfer coefficient increased. With a decrease in the channel height and width there was an increase in the average Nusselt number in the channel.

Chapter 1 Introduction and Literature Review

1.1 Introduction

Micron size mechanical devices are today encountered both in commercial and in scientific applications. As a rule of thumb all devices with characteristic dimensions between 1 μm and 1 mm are called micro-devices. The steady demand for continuous enhancement in the performance of electronic products requires the development of efficient and compact heat dissipation devices. An innovative method for removing large amounts of heat from small areas is the micro-channel heat sink which is made from a conductive solid (e.g., silicon or copper) with micro-channels machined in it and used as flow passages for the cooling fluid. Effects of restricted flow passage on the heat transfer in microtubes and two-dimensional microchannels were investigated for various shapes and sizes of the restriction/protrusion. The shapes considered were rectangular, triangular, and semicircular restrictions/protrusions.

Tube-in-block is the most popular heat exchanger design in the industry. Some of the applications that use this type of heat exchanger are: Magnetic refrigeration and electronic cooling systems. Magnetic refrigeration and electronic cooling use tube-in-block heat exchangers at a microscopic scale. Magnetic refrigeration profits from the fact that the temperatures of certain materials increase when placed in a magnetic field, and likewise decrease when the magnetic field is removed. This phenomenon is known as the

"magnetocaloric effect". This study is concerned with the magnetocaloric beds only. The magnetocaloric beds are microchannels fabricated in a magnocaloric material substrate. The material used in this project is gadolinium. When a microchannel consisting of Gadolinium substrate is exposed to a magnetic field, it generates heat in the Gadolinium substrate. This heat generation in the system is dissipated with fluid flowing through the microchannels.

This paper reports exploration of the steady state analysis of forced convection around a restricted flow passage in a micro channel, effect of protrusions in a microtube or microchannel for conjugate heat transfer with uniform or discrete heating and transient analysis of heat transfer in trapezoidal microchannels under time varying heat source.

1.2 Literature Review

1.2.1 Analysis of convection around a restricted flow passage in a microchannel

A considerable amount of research activity has been devoted to the understanding of fluid flow and heat transfer in micro-devices. A review of experimental data has been presented by Morini [1] and a review of micro-fabrication techniques has been reported by Kandlikar and Grande [2]. One major issue that received considerable attention in the recent literature is whether the continuum/classical model (the conventional Navier-Stokes equations and the conventional energy equation) are valid at the microscale. Adams et al. [3] reported experimental data for turbulent, forced convection of water in circular microchannels with diameters of 0.76 and 1.09 mm. They noted that the classical correlations for Nusselt number under-predicted the measured values and they proposed a specialized correlation for microchannels. More recently, a similar experiment was

performed by Owhaib and Palm [4] in which turbulent forced convection of R-134a was investigated in a single microtube (0.8, 1.2, or 1.7 mm internal diameter). Their results showed good agreement with the classical correlations, while none of the specialized correlations, including the one in [3], agreed with the test data. Guo and Li [5] argued that discrepancies between the experimental results for microchannels and the classical correlations might be due to measurement errors and should not be misinterpreted as being caused by novel phenomena at the microscale.

Harms et al. [6] carried out experiments on single phase forced convection in deep rectangular micro channels. Two configurations were tested, a single channel system and a multiple channel system. The results showed that decreasing the channel width and increasing the channel depth provide better fluid flow and heat transfer performance. The experimentally obtained local Nusselt number agreed reasonably well with classical developing channel flow theory. Quadir et al. [7] applied a finite element method to evaluate the performance of microchannel heat exchangers. The finite element method was proved satisfactory to predict the surface temperature, the fluid temperature and thus the total thermal resistance of the microchannel heat sink. Bendib and Olivier [8] studied microchannels, fabricated by micromachining technology. Results from simulation as well as analytical study were presented. Tunc and Bayazitoglu [9] investigated convection heat transfer in a rectangular microchannel where the flow was assumed to be thermally and hydrodynamically fully developed.

Kroeker et al. [10] investigated the pressure drop and thermal characteristics of heat sinks with circular microchannels using the continuum model consisting of the conventional Navier-Stokes equations and the energy conservation equations. A

comparison between circular and rectangular channels at the same Reynolds number and hydraulic diameter showed that sinks with rectangular channels have lower thermal resistance, while sinks with circular channels dissipate more heat per unit pumping power. Lelea et al. [11] conducted experimental and numerical research on microtube heat transfer and fluid flow for diameters of 0.1, 0.3 and 0.5mm for laminar flow with Reynolds numbers ranging up to 800 with distilled water as the working fluid. They confirmed that the classical or conventional theories are applicable for water flow through microchannels when the entrance effects are considered.

Liu et al. [12] conducted a numerical investigation for fluid flow and heat transfer in microchannel cooling passages taking into account the effects of viscosity and thermal conductivity variations on characteristics of fluid flow and heat transfer for low Reynolds numbers in a 100μm channel with localized heat flux boundary conditions. It was found that the velocity field was highly coupled with distribution of temperature and got distorted by variation of viscosity and thermal conductivity. It was also found that the induced cross flow contributed to heat transfer.

Cheng and Wang [13] experimentally examined the forced convective flow over two sequentially heated blocks mounted on one principal wall of a channel. In the experiments the various block spacing were used and the Reynolds numbers were set at 1300 and 10000 which correspond to the laminar and turbulent flow cases, respectively. Mahapatra et al. [14] solved numerically unsteady Navier-Stokes equations by finite-difference technique for a flow through a channel with locally symmetric and asymmetric constrictions.

Chang and Yang [15] numerically investigated electrokinetically driven flow mixing in microchannels by incorporating pattered rectangular blocks to enhance species mixing. They found that the species mixing was enhanced by creating a stronger diffusion effect due to the constriction in the bulk flow. They also showed that patterning heterogeneous upper surfaces on the rectangular blocks can be an effective means of enhancing the species mixing.

Lee and Garimella [16] analyzed numerically laminar flow and heat transfer in a modified microchannel heat sink containing recesses on the inner surface, which showed an augmentation of heat transfer without an added penalty of increased pressure drop. They also showed that the flow expansion into recesses and the subsequent contraction in the downstream region caused significant enhancement in heat transfer. Korichi and Oufer [17] investigated the effect of the presence of three blocks two on the lower wall and one on the upper wall on laminar convective heat transfer. The effects of Reynolds number block spacing and dimensions and solid to fluid thermal conductivity ratios were studied with a uniform heat flux through the blocks. They found that as the value of Reynolds number was increased, the heat removed from the obstacles also increased with a maximum heat removal around the obstacle corners. They also showed that the temperature difference between the three obstacles decreased with increase in Reynolds number.

Croce and D'Agaro [18] investigated the roughness effect on heat transfer and pressure losses in microscale tubes and channels using a finite element CFD code. Surface roughness was explicitly modeled through a set of randomly generated peaks along the ideal smooth surface. Different peak shapes and distributions were considered;

geometrical parameters are representative of tubes in the diameter range of 50 to 150 μm. They assumed a fully developed flow in their analysis. A significant increase in Poiseuille number was detected for all the configurations considered, while the effect of roughness on the heat transfer rate was smaller and highly dependent on the tube shape.

1.2.2 Protrusions in a microtube for conjugate heat transfer with uniform or discrete heating

Lee et al. [19] conducted an experimental investigation to explore the validity of classical correlations based on conventional sized channels for predicting the thermal behavior in single-phase flow through rectangular microchannels. The microchannels considered ranged in width from 194 μm to 534 μm, with the channel depth being nominally five times the width in each case. Each test piece was made of copper and contained ten microchannels in parallel. The experiments were conducted with water, with the Reynolds number ranging from approximately 300 to 3500. Numerical predictions obtained based on a classical, continuum approach were found to be in good agreement with the experimental data.

Pfund et al. [20] determined friction factors for high aspect ratio microchannels. Reynolds numbers were between 60 and 3450. Pressure drops were measured within the channel. Transitions to turbulence were observed with flow visualization. Rahman [21] presented new experimental measurements for pressure drop and heat transfer coefficient in microchannel heat sinks. Ambatipudi and Rahman [22] numerically studied conjugate heat transfer in rectangular microchannels in a silicon wafer. The effects of channel aspect ratio and Reynolds number were investigated.

Qu et al. [23] experimentally investigated heat transfer characteristics of water flowing through trapezoidal silicon microchannels with hydraulic diameters of 62-169 μm. They also carried out numerical analyses. The results indicated that the experimentally determined Nusselt number is much lower than that calculated from numerical analysis. They attributed this to surface roughness. They also developed a relationship that accounted for the roughness-viscosity effect and used it to interpret experimental results. Federov and Viskanta [24] numerically studied the steady state three-dimensional heat transfer in an asymmetric rectangular channel having laminar flow. Silicon was used as the substrate material and water was the working fluid. A uniform heat flux of 90 W/cm^2 was imposed on one of the walls. They pointed out that extremely large temperature gradients occur within the solid walls in the immediate vicinity of the channel inlet, which has the potential for significant thermal stress and structural failure of the heat sink.

Celata et al. [25] performed heat transfer experiments in capillary tubes with R-114 and water for diameters ranging from 0.13 to 0.29 mm. The transition from laminar to turbulent regime occurred at Reynolds number in the range 1900-2500. Van Male et al. [26] investigated heat and mass transfer in a square microchannel. Correlations for Nusselt and Sherwood numbers were obtained. The laminar flow results showed good agreement with experimental data.

Rao et al. [27] presented the distribution of local heat transfer coefficient for fluid flow in circular microtubes inside a rectangular substrate when a constant heat flux condition exists at one boundary of the substrate. A correlation for peripheral average Nusselt number was developed. Nilson et al. [28] presented analytical and numerical

solutions for steady evaporating flow in microchannels with rectangular cross section. Kim and Kim [29] studied modeling methods for thermal analysis of microchannel heat sinks. The solutions for velocity and temperature distributions were obtained. Ji and Peterson [30] conducted a detailed numerical simulation of heat transfer occurring in silicon based microchannel heat sinks in order to optimize the geometric structure. The effect of microchannel geometry on temperature distribution in the microchannel heat sinks was discussed. The model was validated by comparing the solution with experimental results.

Celata et al. [31] conducted an experimental investigation to characterize the diabatic behavior of single-phase laminar flow in circular microduts, ranging in diameter from 528 down to 120 μm. The vacuum environment in which experiments were carried out ensured a test section free of convective losses, hence the measurements were as precise as possible with in the geometry of the microchannel.

Shevade and Rahman [32] investigated convective heat transfer in microchannels with rectangular and square cross sections for volumetric heat generation in the substrate due to an imposed magnetic field. Gadolinium was used as the substrate material and water as the working fluid. Velocity and temperature distributions were obtained by varying channel aspect ratio, Reynolds number, and heat generation rate in the substrate.

Yang et al. [33] investigated the electroosmotic flow in T-shaped microchannel configuration with a mixing channel of width 280 μm. Computational fluid dynamics simulations and experiments were performed to investigate the mixing efficiency of various geometrical parameters. Numerical results showed that the mixing efficiency

could be enhanced to yield a fourfold improvement if two pairs of side channels were in corporate din to the mixing channels.

Shen et al. [34] experimentally investigated single phase convective heat transfer in a compact heat sink consisting of rectangular microchannels. It was found that the friction factor and Nusselt number significantly depart from those of conventional theories due to surface roughness.

Hibara et al. [35] developed a capillarity restricted method for microchannel surface for gas-liquid microchemical operations in microchips. In this method, a microstructure combining shallow and deep microchannels and the principle of capillarity were utilized for chemical modification of a restricted area of a microchannel. They demonstrated that the proposed patterning method could be used in general microfluidic gas-liquid operations.

1.2.3 Transient heat transfer in trapezoidal microchannels under time varying heat source

Peng and Peterson [36] experimentally investigated single-phase forced convective heat transfer of water in small rectangular microchannels for different diameters. The results stated that the geometry had a significant effect on the single-phase convective heat transfer. It was also found that the laminar heat transfer is dependent upon the aspect ratio. The turbulence was found to be a function of a non-dimensional variable Z, such that Z=0.5 is the optimum length regardless of the channel's aspect ratio. Empirical correlations were suggested for calculating both the heat transfer and the pressure drop. Papautsky et al. [37] described the effect of a rectangular microchannel aspect ratio on laminar friction constant. The experimental data obtained for water

showed an approximate 20% increase in the friction constant for a specified driving potential when compared to micro-scale predictions from the classical Navier-Stokes theory. Lower aspect ratio also showed a substantial increase of 20% in friction constant. The experiment data also showed a similar increase when low Reynolds numbers are used (less than 100).

Rahman and Shevade [38] studied the analysis of heat transfer processes during the heat up and cool down phases of a magnetic material substrate when subjected to a magnetic field. A computer simulation of fluid flow and heat transfer are carried out. Rectangular and square microchannels were considered where water was the working fluid and Gadolinium was the substrate material. The parametric study included heat generation, aspect ratio and Reynolds number. They found a sinusoidal behavior for the heat transfer coefficient along time.

Kohl et al. [39] experimentally examined the pressure drop in microchannels. Straight channel test section with rectangular microchannels was used. Koo and Kleinstreuer [40] investigated the effects of viscous dissipation on the temperature field and ultimately on the friction factor using dimensional analysis and computer simulation. It turned out that for microconduits, viscous dissipation is a strong function of the channel aspect ratio, Reynolds number, Eckert number, Prandtl number, and conduit hydraulic diameter.

Rahman and Shevade [41] studied the effect of using water, ammonia, and FC-77 as the possible working fluids in composite channel of trapezoidal cross-section. Velocity and temperature distribution were investigated by varying channel aspect ratio, Reynolds number, and the magnetic field. The thickness of gadolinium slab, spacing between

channels in the heat exchanger, and fluid flow rate were also varied. It was seen the peripheral average heat transfer coefficient and Nusselt number is larger near the entrance and decreases downstream because of the development of the thermal boundary layer. With increase in Reynolds number, there was a decrease in outlet temperature and there was an increase in average heat transfer coefficient.

Rao and Rahman [42] investigated the transient heat transfer for laminar flow inside a circular microchannel, embedded in a rectangular substrate, during power start-up using Silicon and Silicon Carbide as the substrate and working fluids were water and FC-72. It was determined that a larger diameter tube or a higher thermal conductivity of the substrate material results in a shorter duration of the transient. Nusselt number decreases with time and asymptotically reaches the steady state condition. It was observed that enlarging the tube from 300 μm to 1000 μm results in lowering of the fluid mean temperature at the exit. It was also found that a higher Prandtl number fluid yields higher maximum substrate temperatures and Nusselt numbers.

1.3 Objectives

From the above literature review, it appears that none of the previous studies have addressed the effect of presence of obstructions in the flow regime. In this work we focus our attention to the analysis of local restricted flow passage of various shapes such as rectangular, triangular and semicircular. The heights of these restrictions were of the order of 5% to 10% of the diameter of the microtube or width of the two-dimensional microchannel (parallel plate). Also the effect of more than one restriction was investigated by placing three and five equally spaced restrictions along the length of the

tube. The hydraulic diameter used was 700 μm and Reynolds numbers ranged from 500 to 1500. The objective is to analyze the variation of local and global Nusselt numbers with restrictions characteristic dimensions for different restriction geometries, working fluids and flow rates. A detailed analysis of local heat transfer enhancement at restricted flow passages in a microchannel or microtube geometry is currently not available and present results may be useful to design systems that need localized high transport rate.

Then a numerical analysis of fluid flow and heat transfer processes in a circular microtube and in a two-dimensional microchannel that have an obstruction in the flow path was done. The effects of heating at the location of the protrusion and also at a location away from the protrusion was studied. In this paper, the wall thickness of the microtube was taken in to consideration and also studied the effect of strategically applying heat flux at the location where the surface effects (protrusions) are located and then compared with the case where the heat flux was applied away from the protrusion. Different protrusion shapes modeled were rectangular, triangular, and semi-circular. For the rectangular one, the height and the width of the protrusions were varied from 5% to 10% of the diameter of the microtube. Also the effect of more than one protrusion in flow regime was investigated by placing three and five equally spaced protrusions in the flow. The effects of the location of the discrete heat source relative to the protrusion were studied by placing a heat source at the protrusion and away from it. Also the wall thickness of the microtube was varied from 100 μm to 700 μm for both the heating conditions. The objective was to come up with a detailed understanding of the conjugate heat transfer and the effects of protrusion dimensions, spacing between them, working fluids, flow rate and solid material properties on the variations of Nusselt number.

The main emphasis of the trapezoidal microchannel study was to develop a simulation model for fluid flow and heat transfer in trapezoidal microchannels by taking into account the heat generation in the solid due to applied magnetic field, conduction in the solid and convection of heat to the fluid. Gadolinium was chosen to be the solid substrate material and water as the working fluid. Detailed parametric study is carried out to study the effect of Reynolds number, magnetic field, height of fluid microchannel, width of fluid microchannel, and working fluid. Steady state and transient cases were studied to better understand the effect of different parameters on the performance of the system.

The main objectives of the current work are:

- To develop a numerical model for fluid flow and heat transfer in a microtube with various shapes and geometries of surface effects (obstructions) being present.
- To conduct a parametric study to understand how different parameters affect the performance of microtubes/microchannels used in heat exchangers.
- To explore both steady state and transient models to understand how time factor effects the performance of microtubes/microchannels used in heat exchangers.

Chapter 2 Analysis of Convection Around a Restricted Flow Passage in a Microchannel

2.1 Mathematical Model

A schematic diagram of the microtube or microchannel section with length "L" and diameter "D" or spacing "B" is shown in Figure 1(a). The periphery of the tube is maintained at a constant wall temperature T_w. The liquid coolant enters with a uniform velocity w_{in} and uniform temperature T_{in}. The flow is assumed to be incompressible, laminar, and steady. The fluid properties for water and R-134a were obtained from [44] and [45] respectively. The properties of the above fluids were correlated according to the following equations. For water between 293 K < T < 400 K; $Cp_f = 9.5x10^{-3}T^2 - 5.9299T + 5098.1$; $k_f = -7.0x10^{-6}T^2 + 5.8x10^{-3}T - 0.4765$; $\rho_f = -2.7x10^{-3}T^2 + 1.3104T + 848.07$; and $\ln(\mu_f) = -3.27017 - 0.0131T$. For R-134a between 230 K < T 360 K; $Cp_f = 1x10^{-4}T^2 - 0.0493T + 7.6462$; $k_f = 0.0003T^2 - 0.5937T + 234.62$; $\rho_f = -0.0224T^2 + 9.0255T + 5.18.72$; $\ln(\mu_f) = -0.014217T + 4.880646$.

Due to symmetry, the computational domain consists of half the tube or channel cross-section as shown in Figure 1(a). The height of the restriction is "e" and spacing between them is "s". Figure 1(b) shows the different shapes of the restriction (i.e., rectangular, triangular and semi-circular) considered for both two-dimensional and tubular configurations studied.

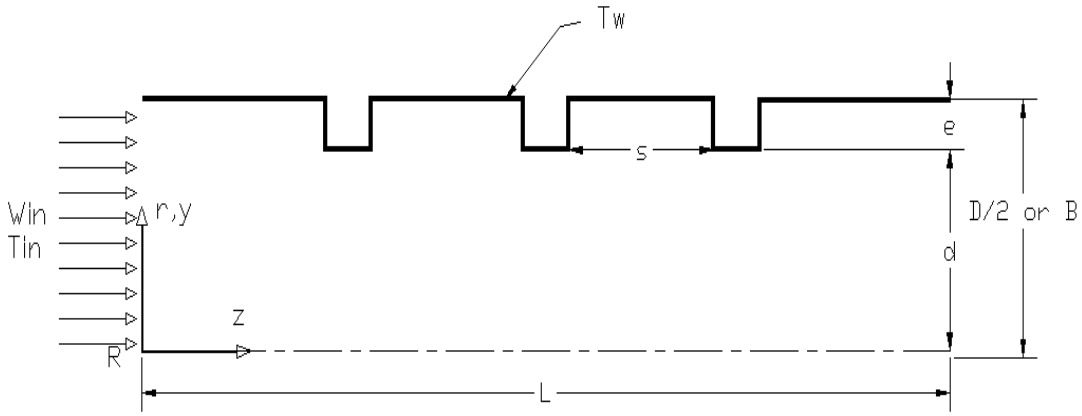

(a)

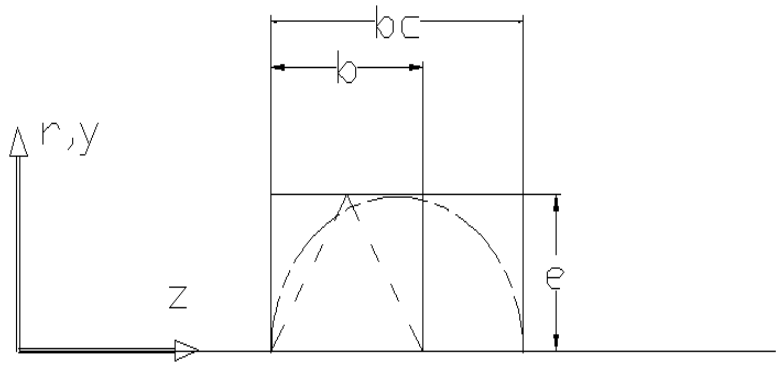

(b)

Figure 2.1 Schematic diagram of the physical problem. (a) Microchannel (microtube) cross-section, (b) Enlarged view of the various shapes of the restrictions used.

The applicable equations for the conservation of mass, momentum, and energy for in the vector form are [44],

$$\nabla .\left(\vec{V}\right) = 0 \tag{2.1}$$

$$\rho\left(\vec{V}\cdot\nabla\right)\vec{V} = -\nabla P + \mu\nabla^{2}\vec{V} \tag{2.2}$$

$$\rho C_{p}\left(\vec{V}\cdot\nabla\right)T_{f} = \nabla\cdot k\nabla T_{f} \tag{2.3}$$

The boundary conditions for the two-dimensional microchannel are:

At $z = 0$, $0 \le y < B/2$: $v = 0$, $w = w_{in}$, $T = T_{in}$ (2.4)

At $z = L$, $0 \le y < B/2$: $P = 0$ (2.5)

At $y = 0$, $0 \le z \le L$: $v = 0$, $\frac{\partial w}{\partial y} = 0$, $\frac{\partial T}{\partial y} = 0$ (2.6)

At $y = B/2$, $0 \le z \le L$: $v = w = 0$, $T = T_w$ (2.7)

The boundary conditions for the axisymmetric flow in a microtube are:

At $z = 0$, $0 \le r < D/2$: $v_r = 0$, $w = w_{in}$, $T = T_{in}$ (2.8)

At $z = L$, $0 \le r < D/2$: $P = 0$ (2.9)

At $r = 0$, $0 \le z \le L$: $v_r = 0$, $\frac{\partial w}{\partial r} = 0$, $\frac{\partial T}{\partial r} = 0$ (2.10)

At $r = D/2$, $0 \le z \le L$: $v_r = w = 0$, $T = T_w$ (2.11)

At the surface of the restriction, the velocity components are zero, the fluid temperature is equal to the wall temperature as the wall is maintained at a constant temperature through out, including the restriction part of the wall. It may be noted that viscous dissipation and pressure work terms were neglected in the energy conservation equation (3). These terms are significant when fluid velocity and Prandtl number are large. For the conditions considered in the present investigation ($w_{in} \le 0.714$ m/s and $Pr \le 6.99$), these effects are expected to be negligible.

2.2 Numerical Simulation and Parametric Study

The governing equations along with the boundary conditions were solved using the Galerkin finite element method. The finite element method is used for finding approximate solution of partial differential equations such as the heat transport equation.

The solution approach is based either on eliminating the differential equation completely (steady state problems), which is then solved using standard techniques. Four node quadrilateral elements were used in the fluid region. In each element, the velocity, pressure, and temperature fields were approximated which led to a set of equations that defined the continuum. The Newton-Raphson algorithm was used to solve the nonlinear system of discretized equations. Newton-Raphson method is a root-finding algorithm that uses the first few terms of the Taylor series of a function in the vicinity of a suspected root. This iterative procedure was used to arrive at the solution for the velocity and temperature fields. The solution was considered converged when the field values became practically constant and the relative change from one iteration to the next reduced below 10^{-6}.

The distribution of cells in the computational domain was determined from a series of tests with different number of elements. The simulations were conducted by maintaining the aspect ratio (the ratio of the element lengths in the z-direction to the r- or y-direction) was maintained greater than 1 and less than 8.

Grid independence tests were conducted by generating results for two cases the first one being the pipe containing the rectangular restriction of e=0.05D and the other for the parallel plates with the rectangular restriction of e=0.1B using different mesh sizes in each case. The number of elements were 150x8(150 axial direction x 8 radial/vertical direction), 300x16, 450x24 and 600x32. These results (corresponding to L/D=14.28, B/D=0.5, Re=500, Pr=6.99) are shown in figures 2.2 (a) and (b).

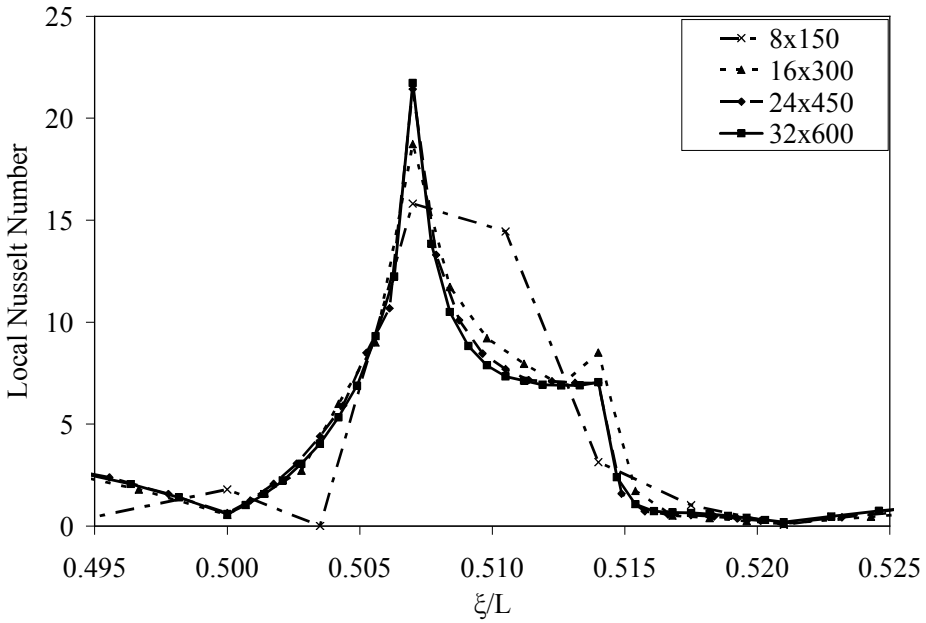

(a)

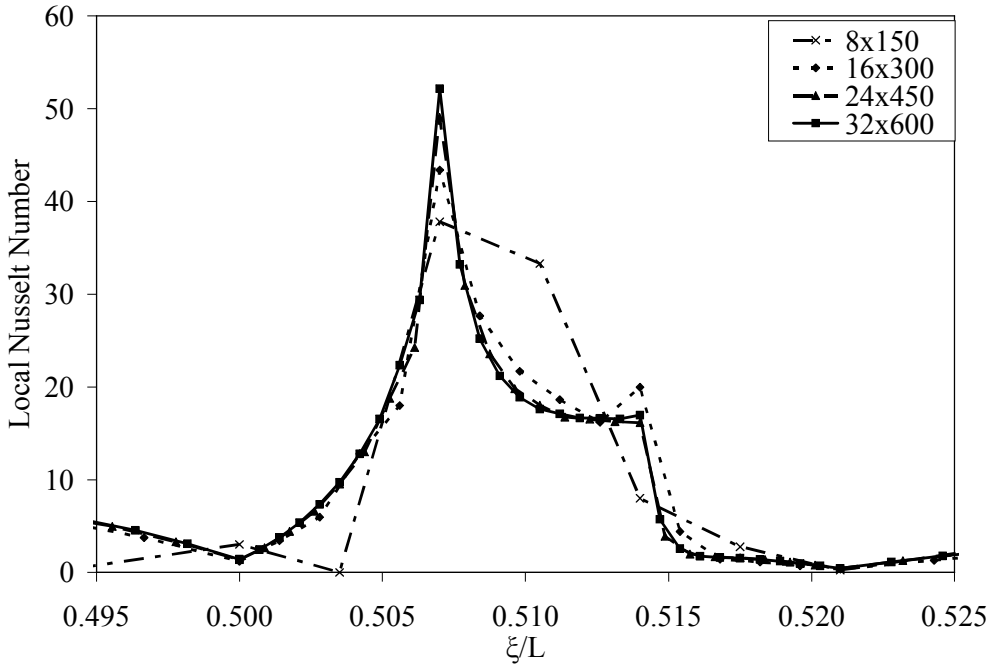

(b)

Figure 2.2 Axial variation of local Nusselt number for different mesh sizes**.** (a) Circular microtube, (b) Two-dimensional microchannel.

Figure 2.2 (a) shows the variation of local Nusselt number along the Axial coordinate for the tube with rectangular restriction. It can be seen that the difference

between the 150x8 and 300x16 meshes is significant, while the differences between the 300x16, 450x24 and 600x32 are very small. Figure 2.2 (b) similarly shows the variation of the local nusselt number along the length of the parallel plates. Again we observe the similar variation between results with different meshes. Based on these results and others it was decided to use the 300x16 mesh in all the calculations.

The axial variation of local Nusselt number for a smooth circular tube with no restriction was also calculated using the same program and the results were compared with the classical solution for developing forced convection in a tube with constant wall temperature [24] as shown in figure 2.3. This comparison provides a base line validation of the numerically computed results.

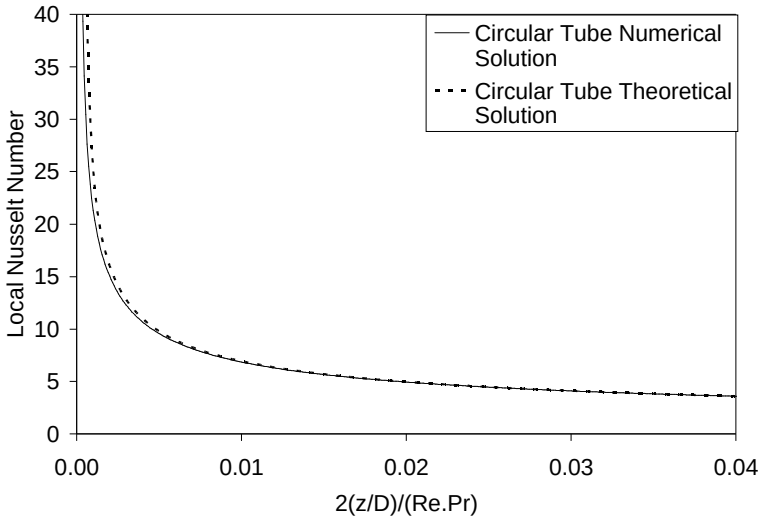

Figure 2.3 Comparison between numerical simulation and theoretical solution [44].

2.3 Results and Discussions

In the numerical computation, the temperature of the wall was kept constant at T_w = 40°C and fluid temperature entering the microtube or microchannel was maintained at T_{in} = 20°C. The diameter of the microtube (D) or the distance between walls in a two-dimensional microchannel (B) was also kept at a constant value of 700 µm. The inlet

velocity (w_{in}) was varied to provide a range of Reynolds number from 500 to 1500. The height of the restriction was e = 0.05D and the width was b = 0.05D for both rectangular and the triangular restrictions.

A plot of streamlines in the tube, obtained from a post-process solution of the stream function equations, are presented in figure 2.4 (a), (b) and (c) for the single restriction configuration. The restriction significantly perturbs the local flow. Steady state recirculation appeared at the back of the step, semi-circular restriction and triangular restriction to varying degrees. On the top of the restriction the reduced cross-sectional area induced a higher velocity. The effects of various shapes of the restriction on heat transfer in a circular tube or parallel plate can be interpreted by a comparison of the local Nusselt number.

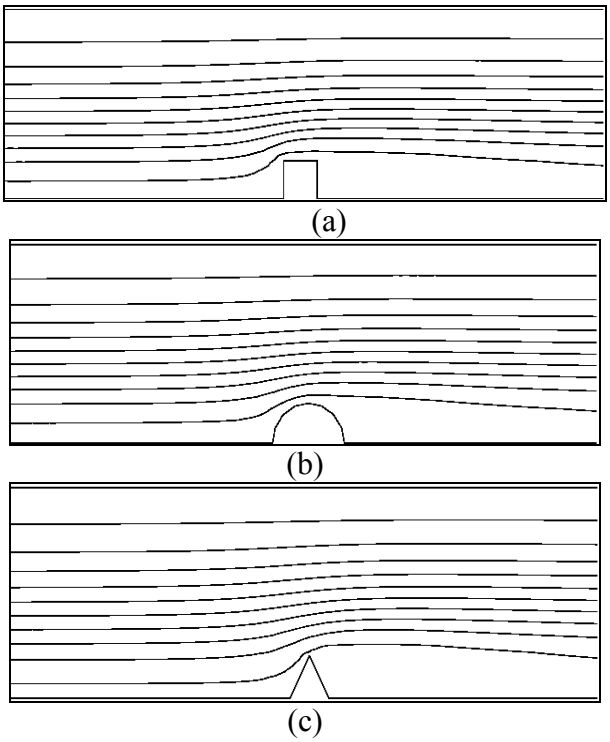

Figure 2.4 Stream lines for water (Re = 500, e =0.05D). (a) Circular microtube, rectangular restriction, (b) Circular microtube, semicircular restriction, (c) Circular microtube, triangular restriction.

2.3.1 Shape of the restriction

The effects of various shapes of the restriction on heat transfer in a circular tube or parallel plate can be interpreted by a comparison of the local Nusselt number. The local Nusselt number is plotted along the length of the wall in Figures 2.5 (a) and (b). Here the rectangular and triangular restrictions start at 0.5cm and ends at 0.507cm and the semicircular restriction starts at 0.5cm and ends at 0.514cm. In the rectangular case we see that there is a drop in the local value of Nusselt number before the beginning of the restriction because the flow is interrupted by the restriction and fluid moves away from the heated wall to go over the restriction. This creates a small recirculation region before the restriction where the heat transfer rate falls below the smooth microchannel. For the rectangular shaped restriction, there is a gradual increase of local Nusselt number along the front wall followed by an abrupt increase as we reach the top wall of the restriction. At the top front corner, the value of local Nusselt number is the highest because the momentum and the thermal boundary layers begin to form again using the corner of the restriction as the leading edge. As the boundary layer thickness increases we can see a gradual decrease of Nusselt number until the flow reaches the trailing corner where the Nusselt number slightly increases. Then at the rear wall of the restriction, we observe a gradual fall in local Nusselt number due to expansion of the flow and associated recirculation. Starting with the bottom trailing edge of the restriction, Nusselt number gradually increases downstream in the recirculating region following the restriction.

In the case of the triangular protrution we see a steady increase in the value of local Nusselt number as the cross-sectional area of the flow decreases and local fluid velocity increases in the direction of the flow. A peak is seen at the vertex of the triangle.

At the downstream side of the triangle, the Nusselt number first decreases abruptly and then gradually. The sharp corner directs the main flow to a larger distance downstream and the rear wall of the restriction is essentially occupied by the recirculating flow. A minimum is seen at a location just downstream from the restriction. Further downstream, the Nusselt number increases gradually. For the case involving the semicircular restriction, the rise and fall of local Nusselt number along the restriction is quite gradual showing much smoother transition compared to the other two shapes of the restriction. The maximum Nusselt number is seen at the tip of the semi-circle where the flow area is minimal. When the inlet velocity of the fluid was increased to obtain higher Reynolds numbers, we saw an increase in the magnitude of the Nusselt number at the location of the restriction. The distribution pattern, however, remained the same.

This above mentioned behavior can be further explained by looking at the isotherm plots for various restrictions in both circular tubes and the rectangular channel as shown in Figures 2.6 (a) - (f). It may be noted that isotherms are sparsely located at the downstream side of the restriction indicating the accumulation of hotter fluid in that region. Also the irregular shape of the isotherms suggests a strong influence of recirculation. It may be noted that isotherms are sparsely located at the downstream side of the restriction indicating the accumulation of hotter fluid in that region. Also the irregular shape of the isotherms suggests a strong influence of recirculation. Of all the three restriction shapes the triangular restriction exhibits the most perturbed isotherms downstream of the restriction. This behavior could be attributed to the fact that the flow moving over the sharp edge of the triangular restriction is directed to the largest distance downstream for reattachment that generates a recirculation We also notice that the

isotherms in the semi-circular restriction case transition in a smoother manner than the other two restriction shapes. This can be attributed to the fact that there is lesser resistance to the flow while moving over the semi-circular restriction than in any other restriction shape due to the absence of sharp edges in the flow path.

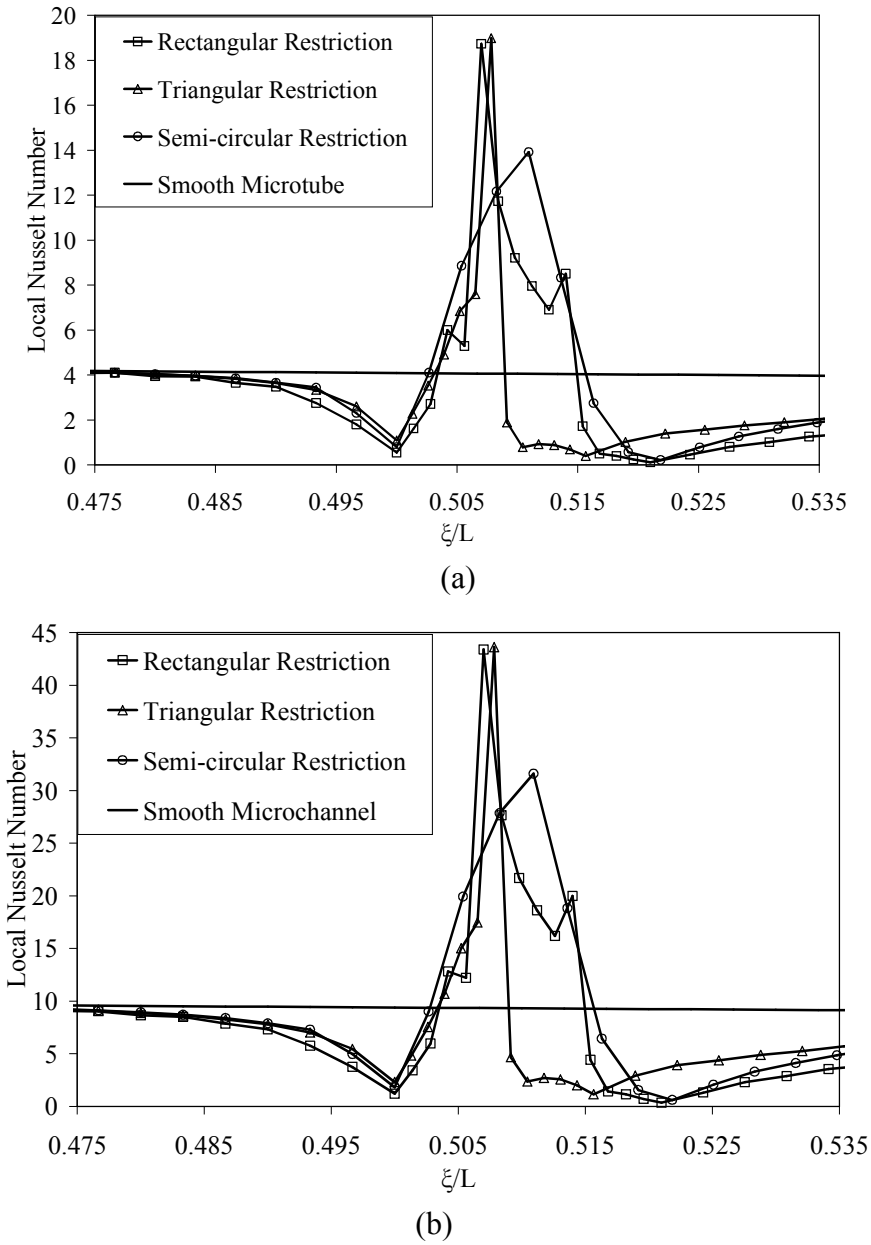

Figure 2.5 Local Nusselt number along stream wise direction for rectangular, triangular and semi-circular restriction using water as the working fluid**.** (a) Circular microtube, (b) Two-dimensional microchannel.

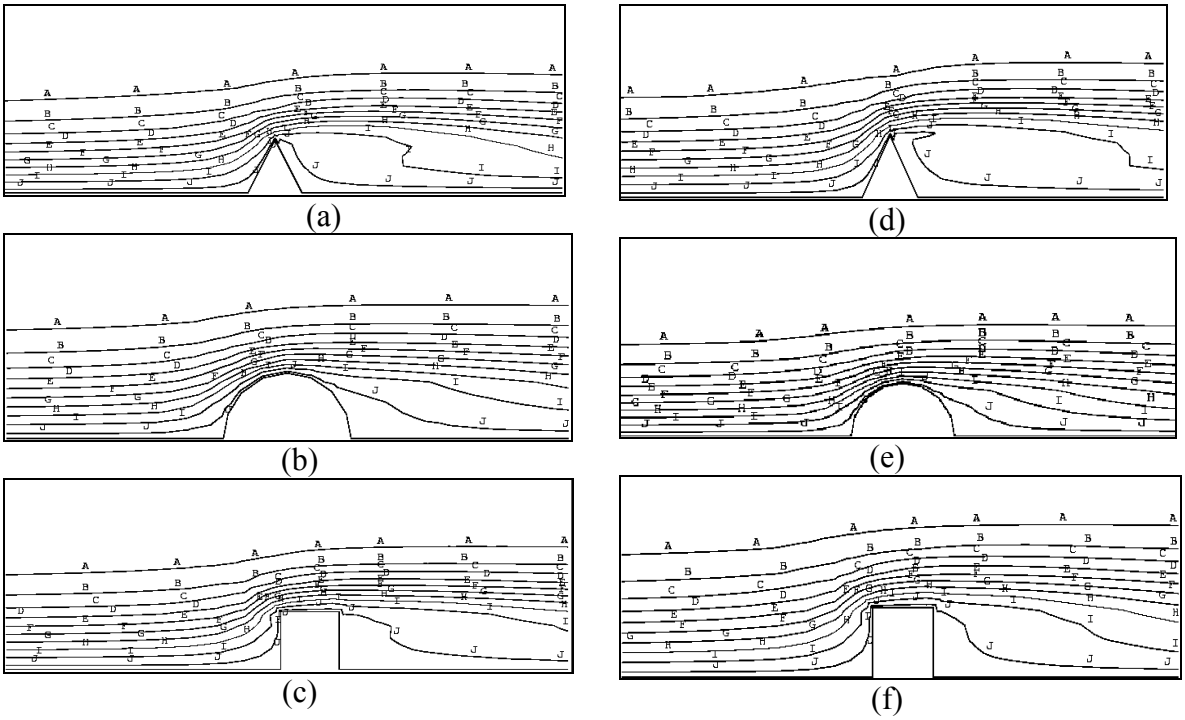

(a) (d) (b) (e) (c) (f)

A- 21°C	B- 23°C	C- 25°C	D- 27°C	E- 29°C
F- 31°C	G- 33°C	H- 35°C	I- 37°C	J- 39°C

(g)

Figure 2.6 Isothermal contours in the near wall region for water.(a) Triangular restriction in circular microtube, (b) Semi-circular restriction in circular microtube,(c) Rectangular restriction in circular microtube, (d) Triangular restriction in rectangular microchannel, (e) Semi-circular restriction in rectangular microchannel, (f) Rectangular restriction in rectangular microchannel, (g) Legends for the isothermal contours.

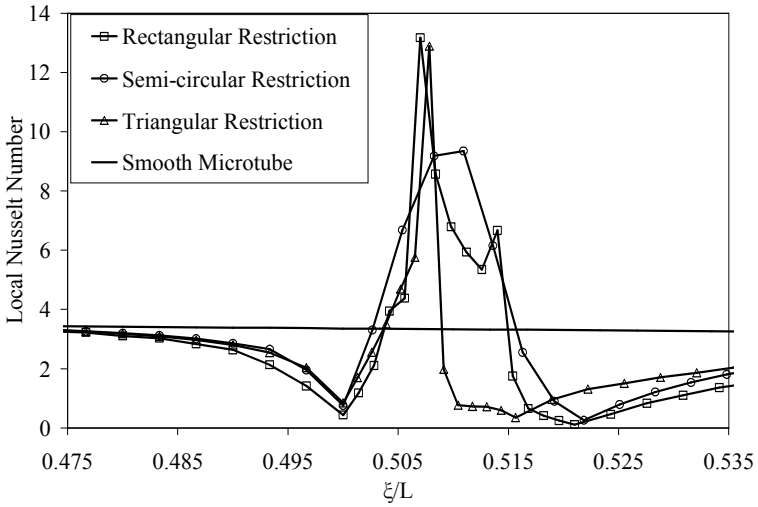

(a)

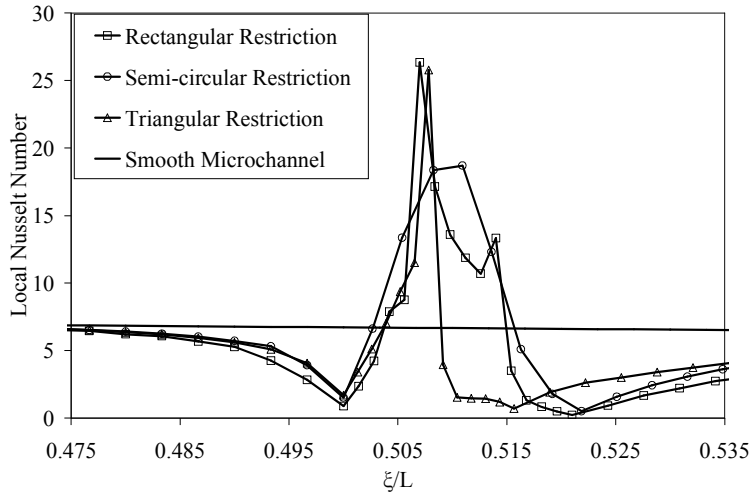

(b)

Figure 2.7 Local Nusselt number along stream wise direction for rectangular, triangular and semi-circular restrictions using refrigerant R-134a as the working fluid for Re=500. (a) Circular microtube, (b) Two-dimensional microchannel.

The above results were obtained using water as the working fluid which has a Prandtl Number of approximately 7. When the working fluid is changed from water to R-134a (Pr=4.2), we see a similar behavior for both microtube and microchannel, as shown in Figures 2.7 (a) and (b). In the rectangular restriction case, there is a drop in the local value of Nusselt number before the beginning of the restriction, then there is an increase

in the value of local Nusselt number at the upstream side of the restriction, and a drop in the value at the downstream side of the restriction, just as seen in the case of water. But the value of local Nusselt number is lower indicating that the magnitude of local Nusselt number at the restriction is primarily controlled by fluid properties (Prandtl number) where as the variation is controlled by the physical structure of the restriction.

2.3.2 Size of restriction

In order to explore the effects of the size of the restriction we varied the dimensions of height "e" and width "b" of the rectangular restriction in both the microchannel and the microtube cases. Figure 2.8 shows the effect of restriction size on local Nusselt Number for the circular microtube. Figure 2.8 (a) shows the variation of local Nusselt Number along the length of the wall for a constant width "b"=0.05B. We can observe that as the height of the restriction increases the value of local Nusselt number increases. The highest Nusselt number for each case is seen at the top front corner. This is due to the formation of both thermal and momentum boundary layers at the top of the restriction with the front top corner as the leading edge. With the increase of restriction size "e", the flow cross-sectional area reduces and causes a larger velocity of flow in the restriction area. This enhances the local convection heat transfer coefficient. A larger "e" however means a larger jump for the flow and longer recirculation region before and after the restriction. In those areas, Nusselt number decreases with increase of "e". Figure 2.8 (b) shows the variation of local Nusselt number along the length of the wall for constant height e=0.05B and for the variation of width "b" from 0.05B to 0.1B. Here we can notice that the value of local Nusselt number remains the same for all three restrictions until the trailing edge of a restriction is

approached. Different values in recirculation region downstream of the restriction are primarily due to different locations for the start of the new thermal boundary layer.

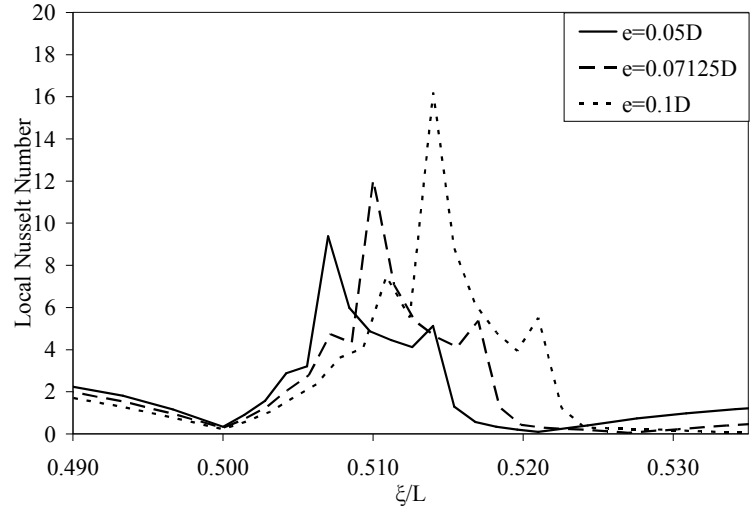

(a)

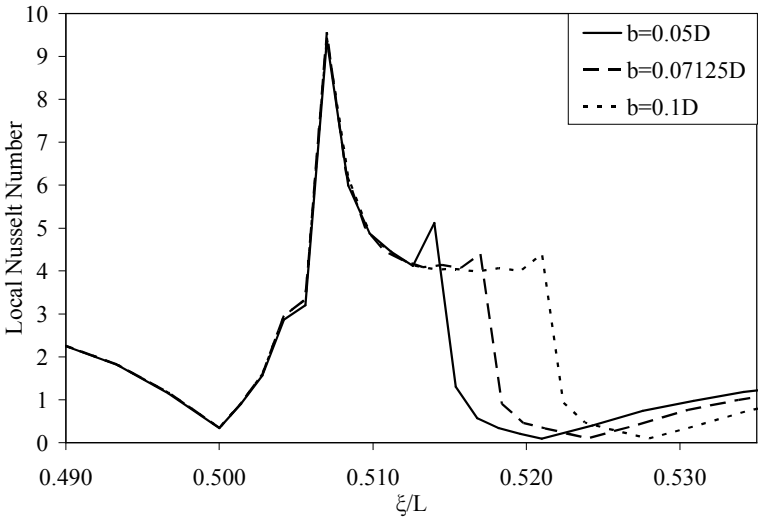

(b)

Figure 2.8 Restriction size effect for circular microtube case, rectangular restriction with water, Re=200. (a) Local Nusselt number along stream wise direction for height "e" varying from 0.05D to 0.1D and "b" =0.05D, (b) Local Nusselt number along stream wise direction for height "b" varying from 0.05D to 0.1D and "e"=0.05D.

Figure 2.9 (a) and (b) shows the variation of local Nusselt Number for two-dimensional microchannel for the same variation of the height "e" and width "b" of the

restriction. It can be observed that it follows the same trend as microtube but the values of the local Nusselt number are significantly higher. The effects of height "e" and width "b" of the restriction were also explored for the triangular and semi-circular restrictions for both microtube and microchannel geometries. In all cases, the maximum local Nusselt number increased with "e" as seen for rectangular restriction.

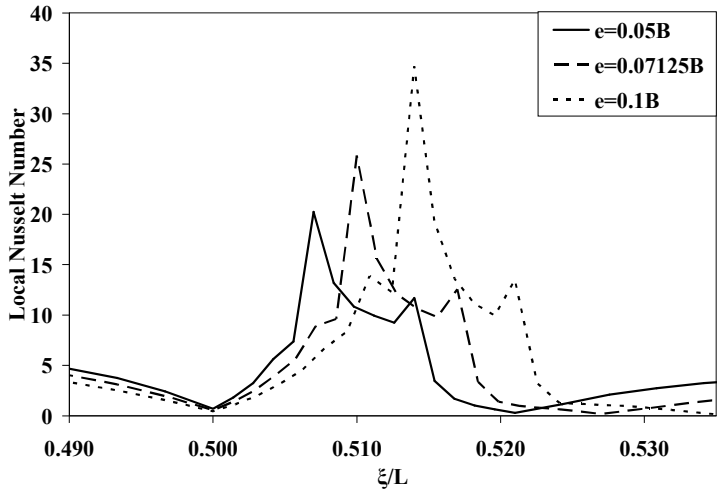

(a)

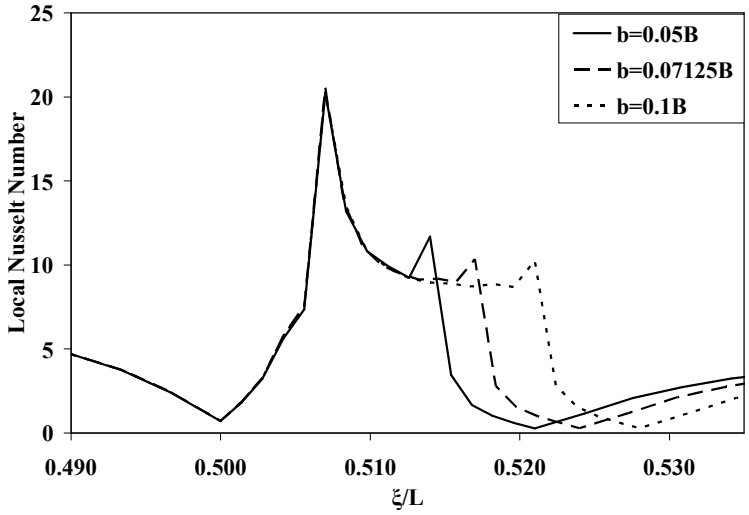

(b)

Figure 2.9 Restriction size effect rectangular microchannel case, rectangular restriction with water, Re=200. (a) Local Nusselt number along stream wise direction for height "e" varying from 0.05B to 0.1B and "b" =0.05B, (b) Local Nusselt number along stream wise direction for height "b" varying from 0.05B to 0.1B and "e"= 0.05B.

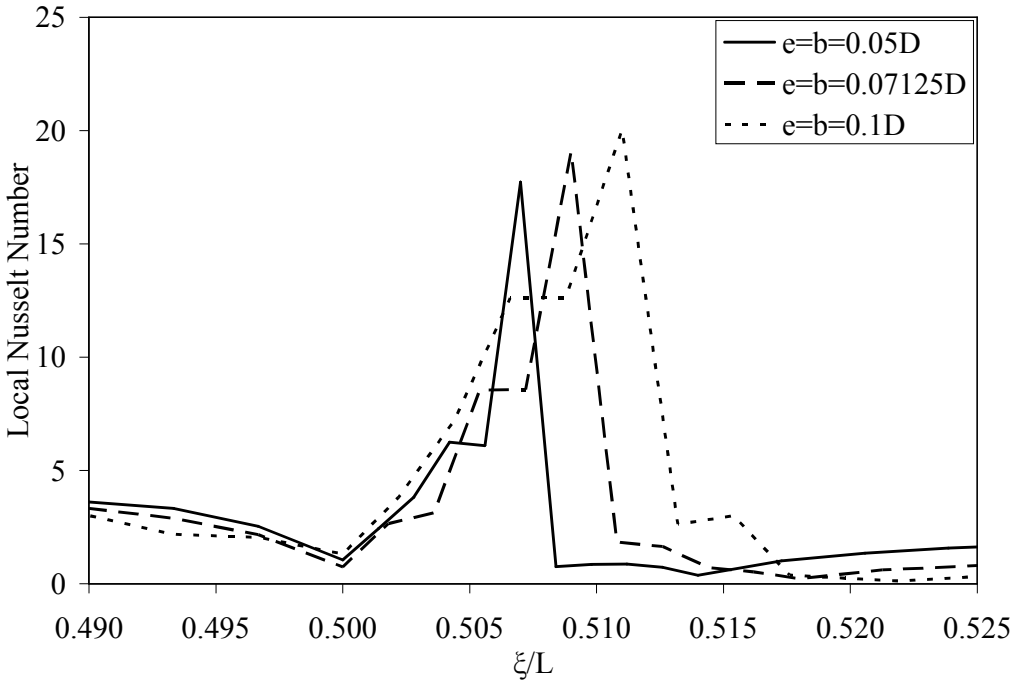

(a)

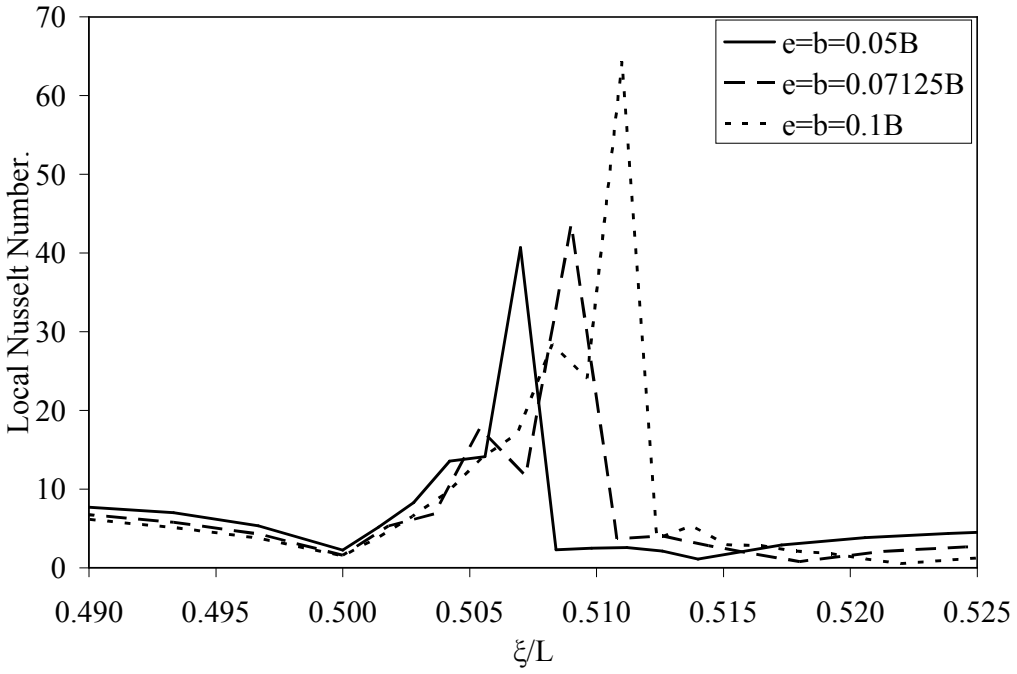

(b)

Figure 2.10 Restriction size effect for triangular restriction with water, Re=500. (a) Local Nusselt Number along stream wise direction for "e" and "b" varying from 0.05D to 0.1D in circular microtube, (b) Local Nusselt Number along stream wise direction for "e" and "b" varying from 0.05B to 0.1B in rectangular microchannel.

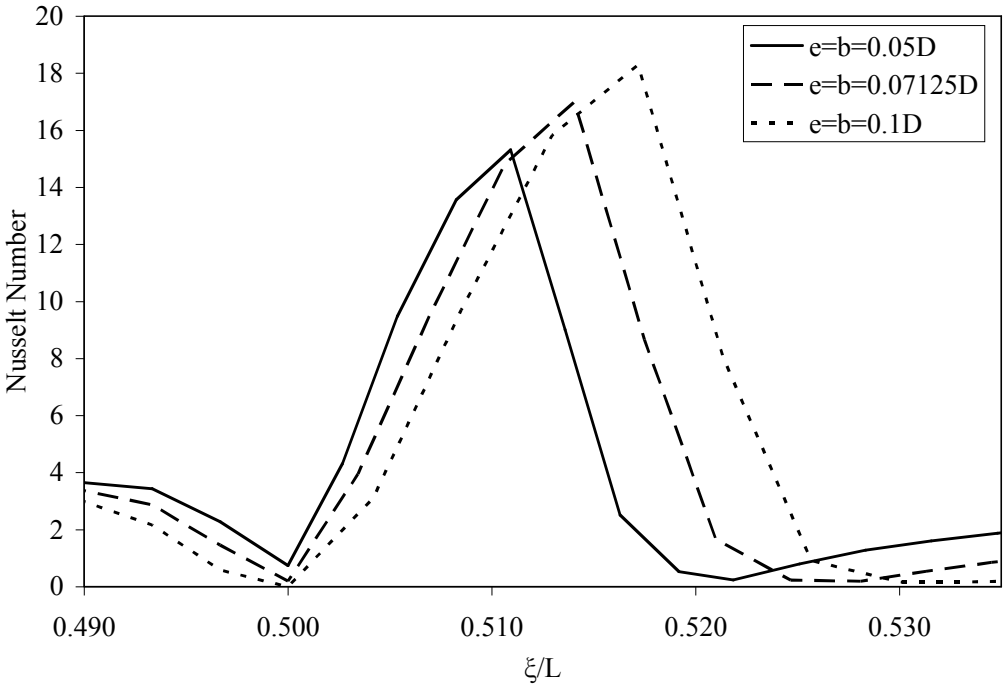

(a)

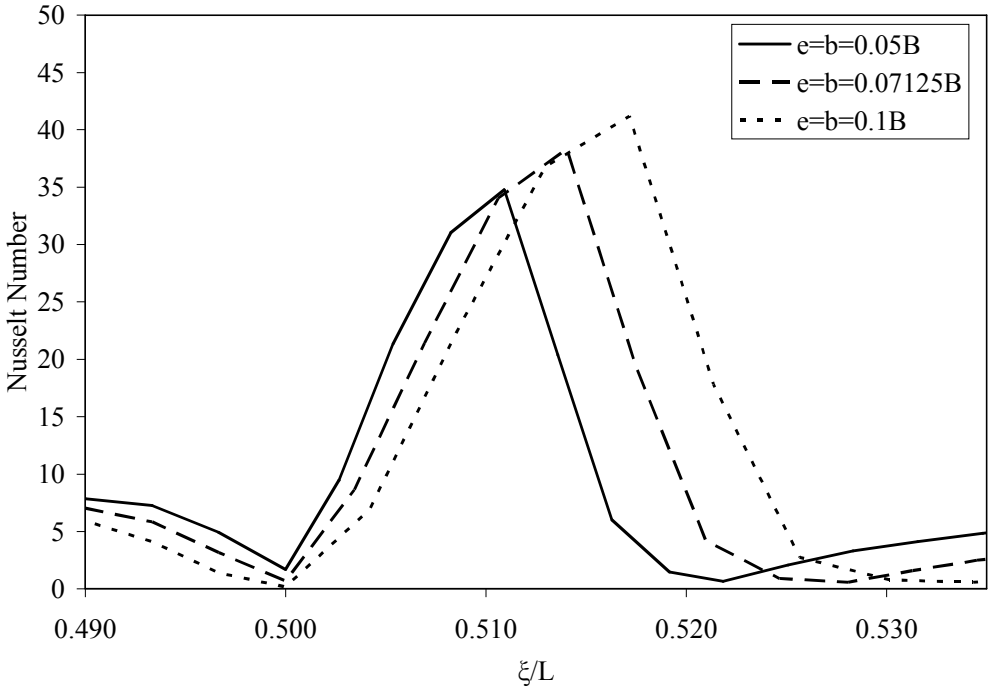

(b)

Figure 2.11 Restriction size effect for semi-circular restriction with water, Re=500. (a) Local Nusselt Number along stream wise direction for "e" and "b" varying from 0.05D to 0.1D in circular microtube, (b) Local Nusselt Number along stream wise direction for "e" and "b" varying from 0.05B to 0.1B in rectangular microchannel.

The effects of height “e” and width “b” of the restriction were also explored for the triangular and semi-circular restrictions for both microtube and microchannel geometries. In all cases, the maximum local Nusselt number increased with “e” as seen for rectangular restriction. In the triangular and semicircular restriction the height “e” and width “b” are varied simultaneously from 0.1B to 0.2B in the micro channel case and from 0.05D to 0.1D for microtube. In figure 2.10 (a) and (b) we see the variation of local Nusselt Number for the triangular restriction for both microtube and microchannel case the value of local Nusselt number increases as the height of the triangle increases and the variation is similar to as seen in the previous cases. Figure 2.11 (a) and (b) shows the local Nusselt Number variation for the semi-circular restriction case for both microtube and microchannel case.

2.3.3 Number of restrictions

Till now we have seen the effect of a single restriction on the Nusselt number. Now we consider more than one restriction in the flow path. For this we consider two configurations, the first configuration consists of three rectangular restrictions and the second configuration consist of five rectangular restrictions; in both cases equally spaced along the length of the microtube or microchannel. Figure 2.12 presents the results for the first configuration. It can be observed that the local Nusselt number peaks at the top front corner of the restriction similar to case of the single restriction. But the highest value of local Nusselt number at the restriction goes on decreasing along the length even though the restrictions are of the same height and width. This is because of the larger bulk fluid temperature as the flow moves downstream. The local heat transfer rate is intimately related to the wall to fluid temperature difference. As wall to fluid temperature difference

drops, the local heat transfer coefficient of Nusselt number drops. Another interesting observation from figure 2.12 is that after each restriction the local Nusselt number recovers to the distribution shown by smooth tube or channel. Therefore, if sufficient distance is provided between restrictions the local Nusselt number over a good portion of the tube or channel that are away from restricted areas will not be affected by the presence of the restriction or no significant history effect of the flow. It suggests that flow restrictions can be conveniently used to trigger local enhancement with out greatly affecting the overall heat transfer pattern. A similar characteristic was seen in the case of the triangular and semi-circular restrictions.

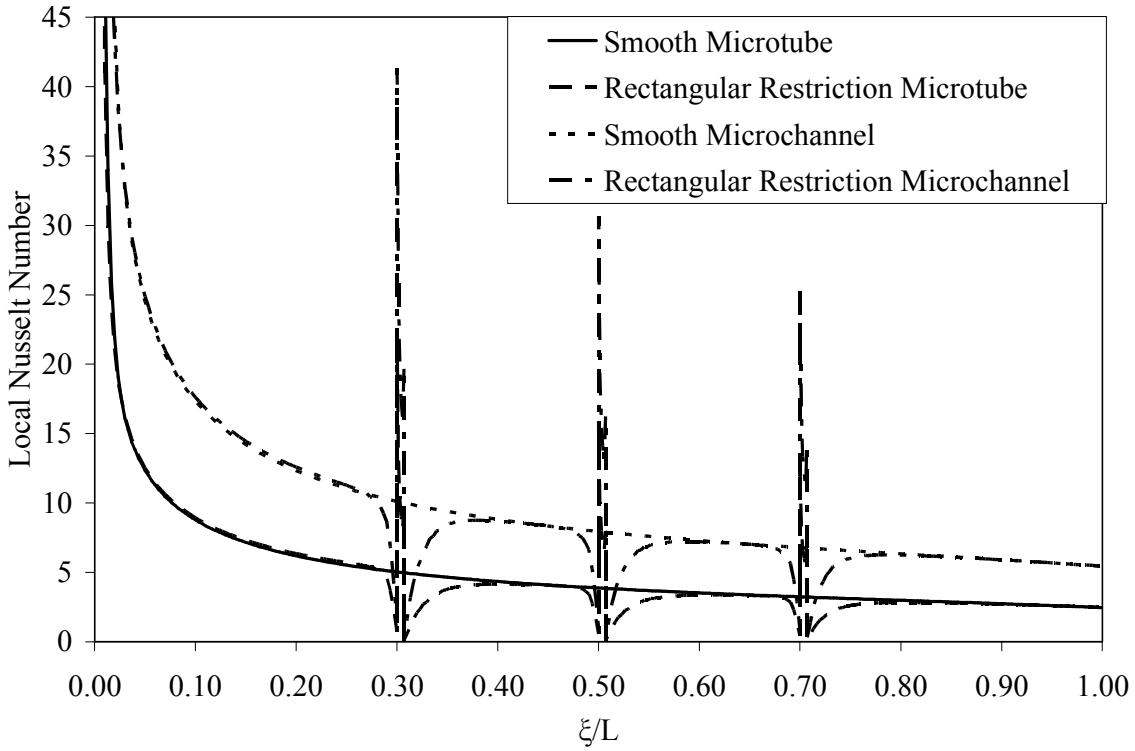

Figure 2.12 Local Nusselt number along stream wise direction for three rectangular obstructions for both circular microtube and rectangular microchannel, Re=500.

Figure 2.13 presents the results for the second configuration containing five equally spaced restrictions. It can be observed that the local Nusselt number variation is

similar to that of the three restriction configuration, but the distance between the consecutive restrictions is small and hence the flow does not stabilize and the momentum and thermal boundary layers are not fully established in the region between restrictions and hence we see that the local Nusselt number values do not coincide with the smooth microtube or microchannel values. Due to smaller distance between restrictions, the flow cannot recover before being disturbed by the subsequent restriction. Therefore, the number of restrictions and spacing between them has a very important role in controlling the overall heat transfer characteristic of the system.

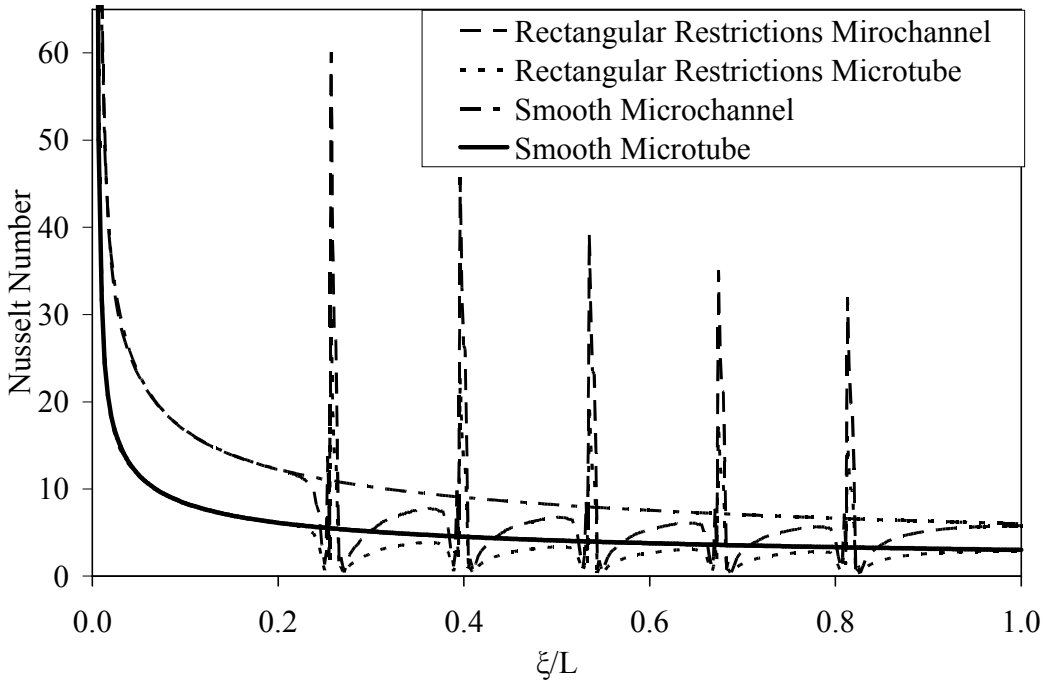

Figure 2.13 Local Nusselt number along stream wise direction for five rectangular obstructions for both circular microtube and rectangular microchannel, Re=500.

Figure 2.14 shows a comparison of our numerical simulation results for local Nusselt number variation with that reported by Croce and D'Agaro [18]. They used a numerical approach to model roughness in microscale tubes and channels. Surface

roughness was modeled by a series of randomly generated peaks or restrictions along an ideal smooth surface and the heights of the restrictions were ranging from 1.32% to 2.65% of the diameter of the tube or the height of the channel. As we have used a restriction height ranging from 10% to 20% of the diameter of the tube or height of the channel till now, we modeled the geometry of the peaks similar to the one in [18] and the variation of local Nusselt number is plotted in Figure 2.14. In Figure 2.14 (a), the comparison of variation of local Nusselt Number with [18] for circular microtube is made.

Figure 2.14 (b) shows a similar comparison for two-dimensional microchannel. The study in [18] assumed a fully-developed flow at the entrance of the tube or channel. The Nusselt number variation for smooth channel is also plotted for reference. In both figures it can be noticed that our results compare reasonably well with values presented in [18] for variation of Nusselt number on top of roughness elements. The curves match at 2^{nd}, 4^{th} and 5^{th} restrictions. In addition, our distributions show more systematic behavior in other two restrictions. In the absence of any test data on microchannel/microtube with restrictions, this validation with results presented by Croce and D'Agaro [18] may be considered as adequate.

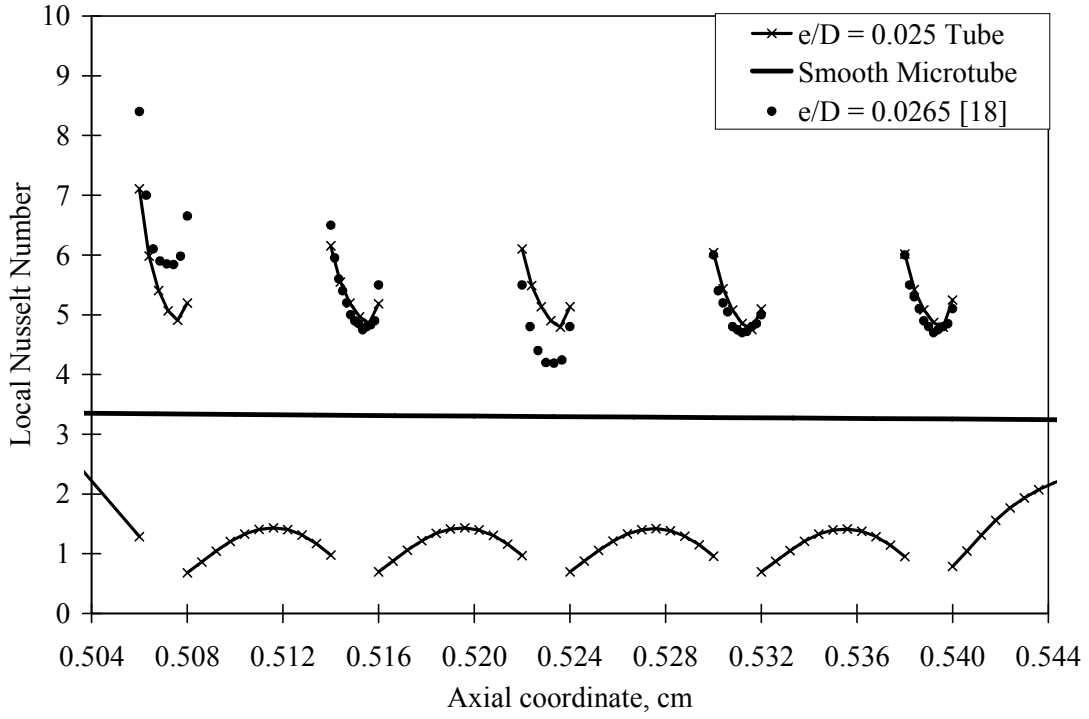

(a)

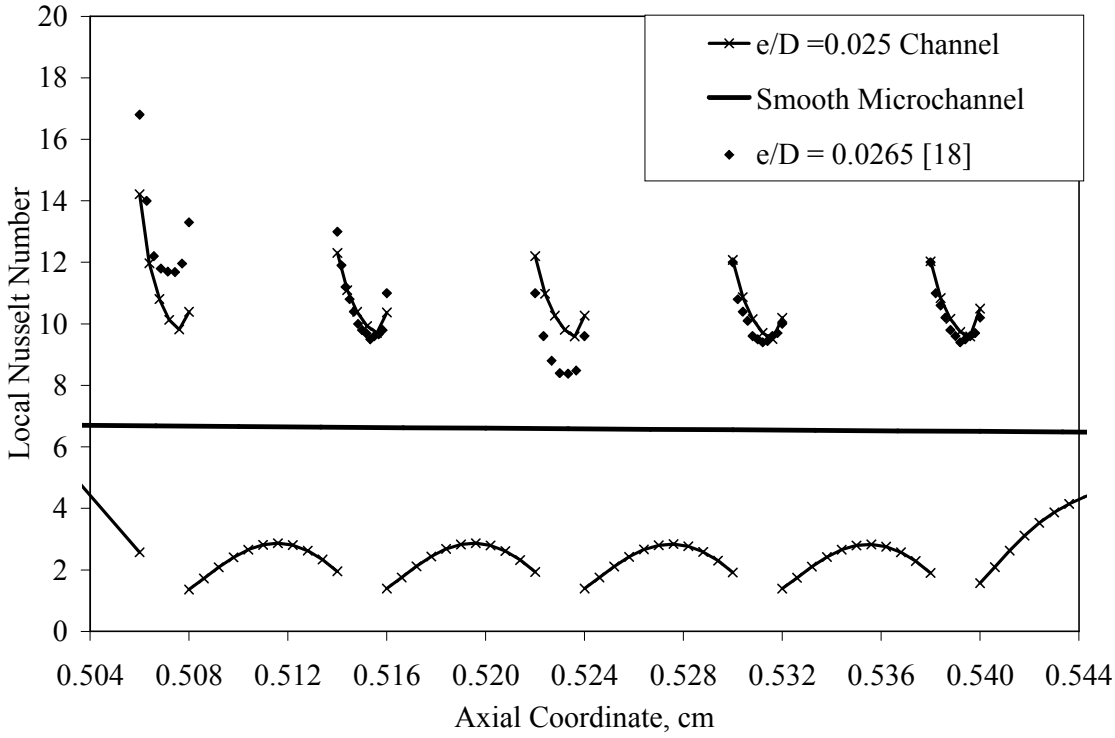

(b)

Figure 2.14 Comparison of local Nusselt number variation with [18]. (a) Circular microtube, (b) Two-dimensional microchannel.

2.3.4 Reynolds number

Until now we studied the local Nusselt number variation for microchannels and microtubes with restrictions. We will now see how the global value of Nusselt number varies for both microchannel and microtube. Global Nusselt number is calculated by taking a weighted average of all the local values of Nusselt number along the length of the microchannel or micro tube. Figure 2.15 shows the average Nusselt number for different Reynolds numbers and shapes of restriction. Figure 2.15 (a) compares the global Nusselt number for various shapes of the restrictions with smooth tube for Reynolds numbers varying from 500 to 1500 for the circular microtube case. Here we find a reduction in the global heat transfer rate for a microtube containing the restriction when compared to a smooth microtube. This decrease is a function of both the shape of the restriction and the Reynolds number. The actual shape of the restriction has an effect on the numerical values of Nu, but does not change the qualitative behavior. The decrease in the heat transfer rate is, however, more significant for the rectangular shape. This can be explained as: the global Nusselt number is a surface-weighted average of values at the peaks (higher than the smooth microtube) and at the valleys (lower than smooth microtube). The peaks cover a lower area (smaller radius) compared to the valley (higher radius). In addition, the peak is much smaller in length compared to the length covered by two recirculating regions at the valley. Hence, the balance is shifted to a lower average Nusselt number.

In Figure 2.15 (b) we compare the average Nusselt number for various shapes of the restrictions in a two-dimensional microchannel with the smooth two-dimensional microchannel for Reynolds numbers varying from 500 to 1500. Here we find an increase in the average Nusselt number for channel containing the restriction when compared to

the smooth channel. This increase is again a function of both the shape of the restriction and the Reynolds number. A rectangular restriction provides the largest enhancement of average Nusselt number.

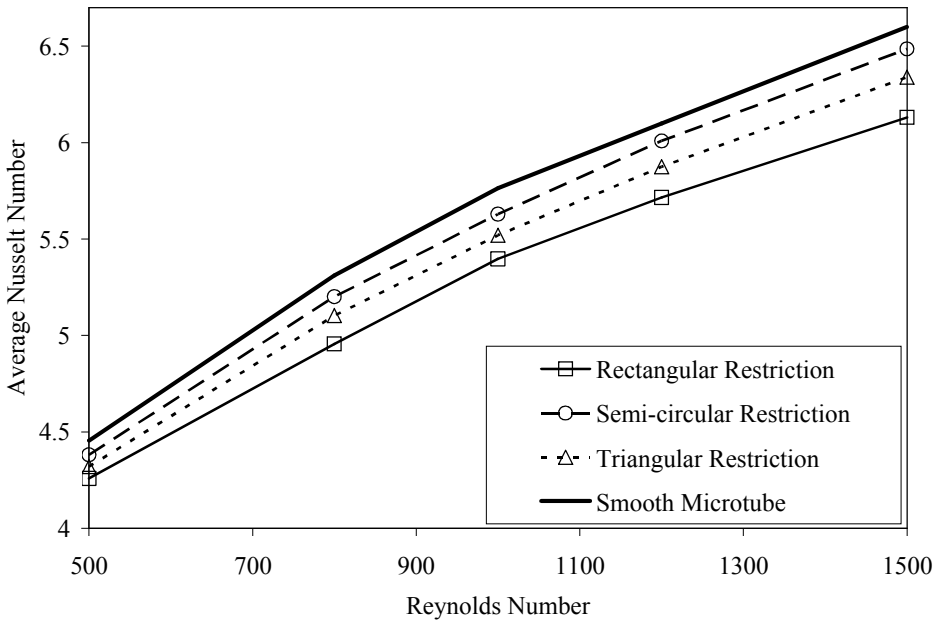

(a)

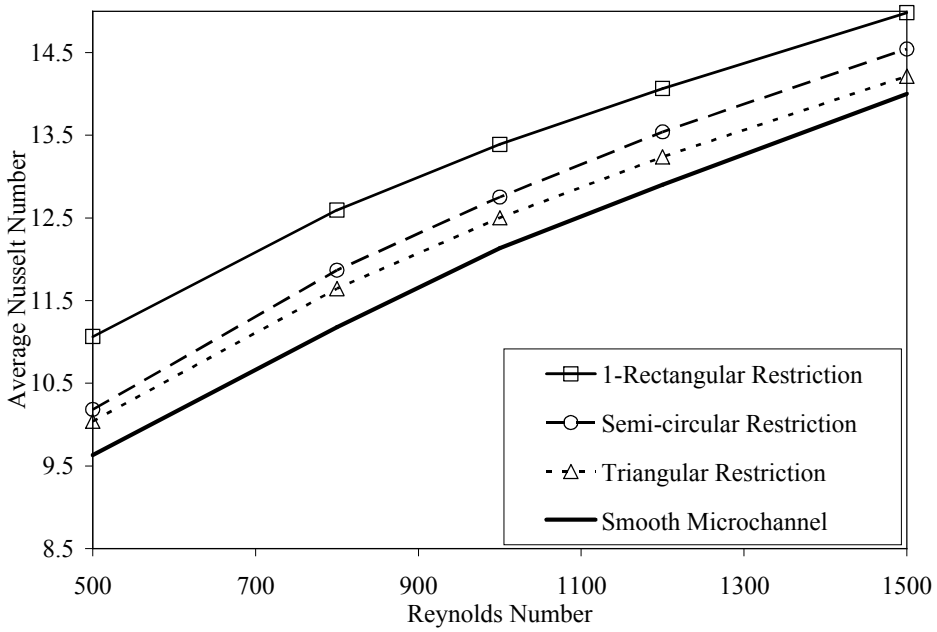

(b)

Figure 2.15 Global Nusselt number for water. (a) Circular tube, (b) Two-dimensional channel.

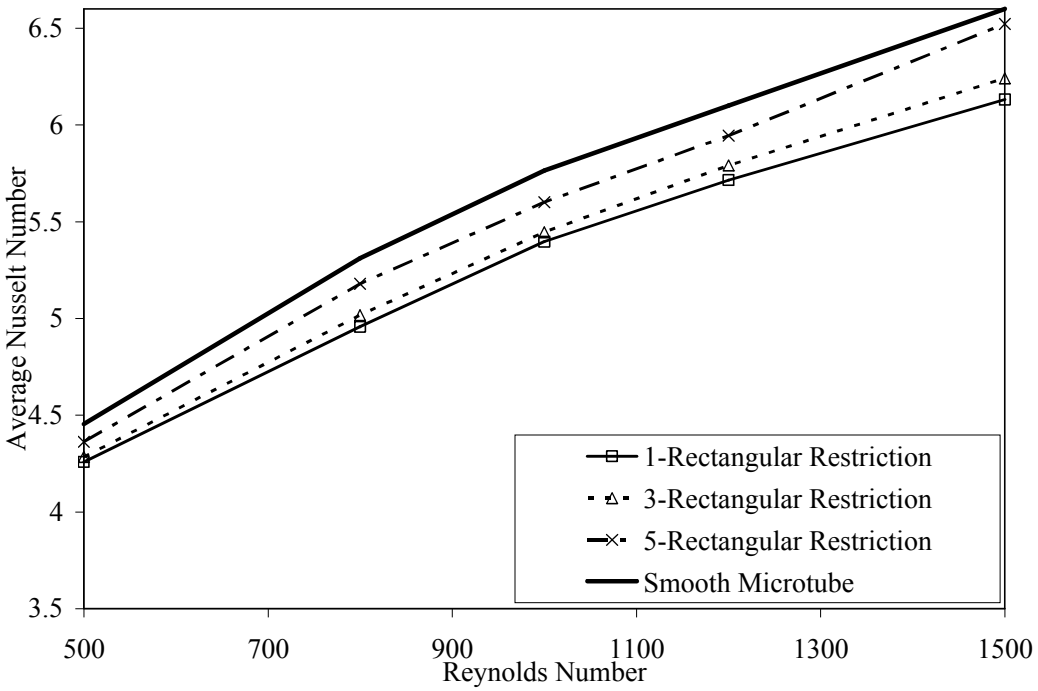

(a)

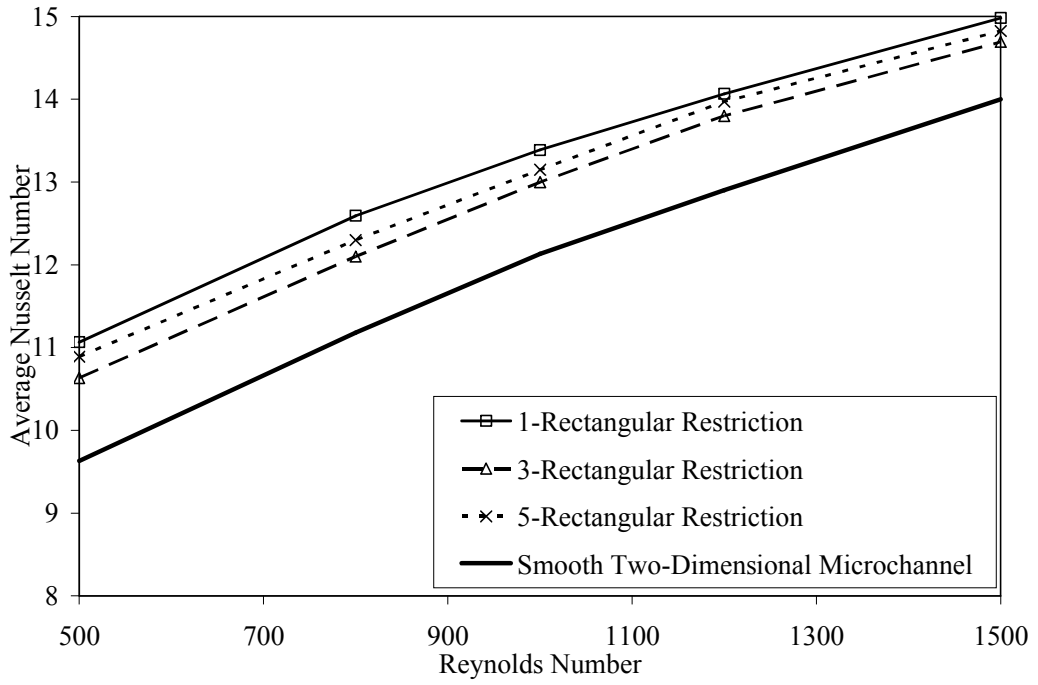

(b)

Figure 2.16 Global Nusselt number for repeated protrusions for water. (a) Circular microtube, (b) Two-dimensional microchannel.

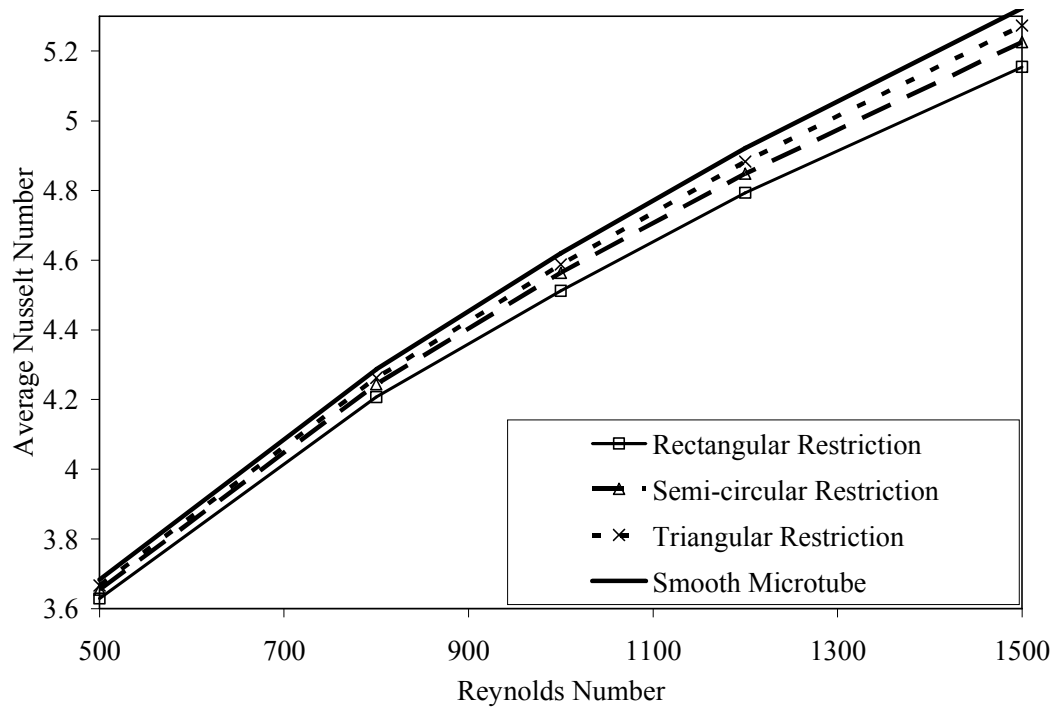

(a)

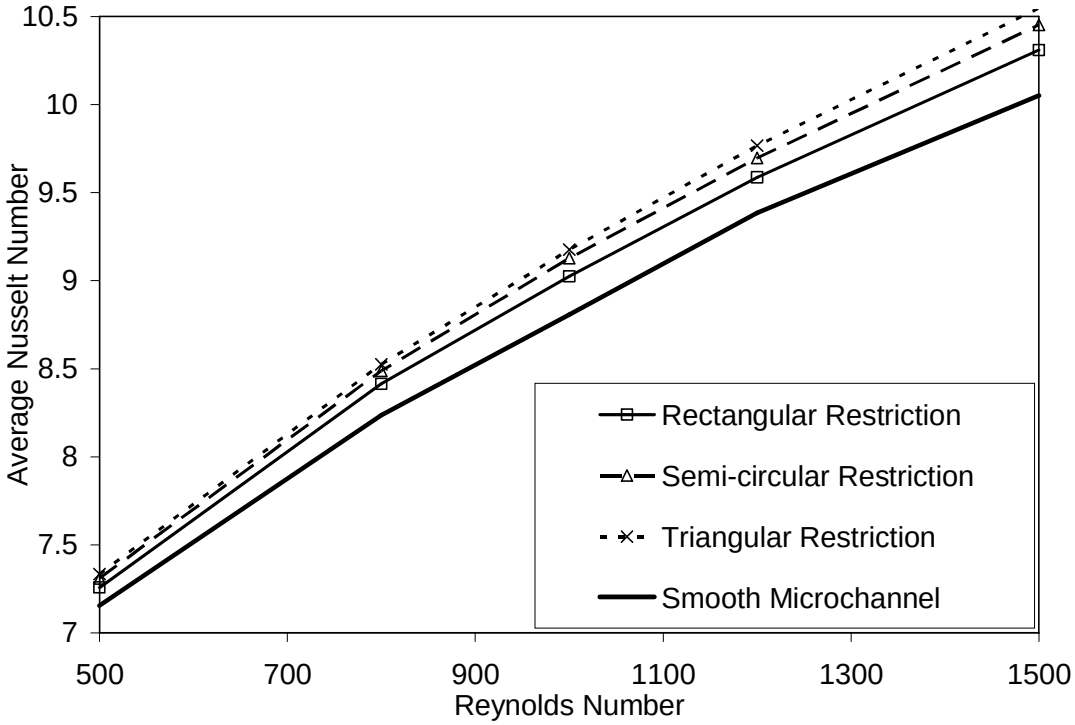

(b)

Figure 2.17 Global Nusselt number for refrigerant R-134a. (a) Circular microtube, (b) Two-dimensional microchannel.

In Figure 2.16 (a) we see the variation of average Nusselt number for smooth microtube and the microtubes with one, three and five restrictions. The smooth tube has the highest Nusselt Number and the other three configurations have lesser average values. But in Figure 2.16 (b) the smooth channel has the least Nusselt number when compared to the other three configurations. It can be noticed that 1-restriction has the highest effect compared to multiple restrictions in flow path.

When we consider refrigerant R-134a, the same trend is seen in the microtube case and the microchannel case as shown in Figures 2.17 (a) and (b) as compared with plots for water. The smooth microtube has higher Nusselt number when compared to the microtubes containing the restriction in the fluid flow domain. For a two-dimensional channel, we see a higher average Nusselt number when a restriction is present. Therefore, the shape of the channel has a very strong influence on whether heat transfer rate is enhanced or diminished when a restriction is present in a microchannel. The values of Nusselt number for R-134a is somewhat lower compared to water because of its lower Prandtl number that controls the thickness of the thermal boundary layer adjacent to the tube wall which in turn controls the convective heat transfer rate. For the temperature range considered in the present investigation, the average Prandtl numbers were 6.99 for water and 4.2 for R-134a.

Figure 2.18 presents the variation of pumping power which is the product of ΔP (difference of pressure between inlet and outlet) and Q (volume flow rate of fluid). The pumping power has been non-dimensionalized using the relevant flow and geometric parameters and presented for Reynolds number varying from 500 to 1500 for the various shapes of the restrictions and for repeated restrictions in a two-dimensional microchannel.

Results for a smooth microchannel are shown for comparison. Water has been used as the working fluid. We see that as the Reynolds number increases, i.e. as the velocity of the working fluid increases, there is an increase in the value of the pumping power. We can also notice that at a lower Reynolds number of 500, the pumping power for all the configurations is about the same. The pumping power required for the five restriction case is the largest and the values for that of the three restrictions case is less than that of the five restrictions case and greater than that of the single restriction cases. With increase in Reynolds number the percentage increase in the pumping power required compared to the smooth microchannel is quite significant.

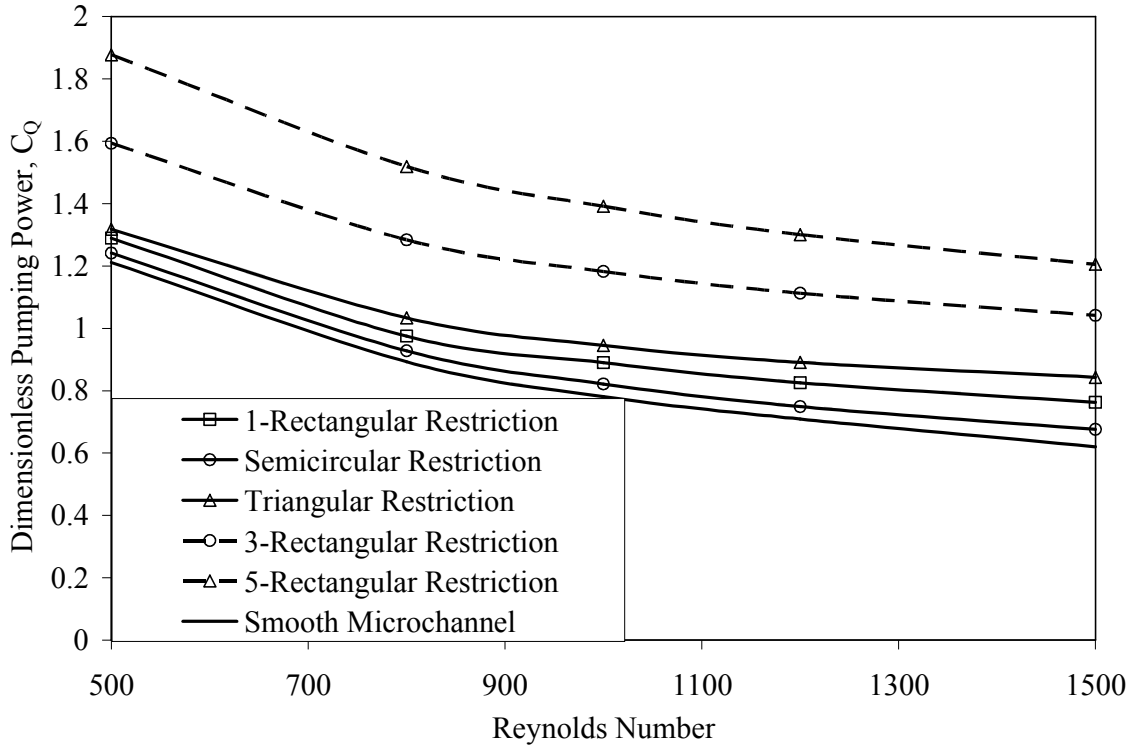

Figure 2.18 Pumping power of microchannel for various restriction shapes and repeated restrictions for water as working fluid.

For a single rectangular restriction at Reynolds number of 500, we observe that the percentage increase in the Nusselt number with reference to the smooth microchannel

is about 12% whereas the pumping power required increases by 8% when compared with the smooth microchannel. Therefore, the heat transfer enhancement is more compared to the pumping power penalty which is good. However for a Reynolds number of 1500 we notice that for a percentage increase of 9% in average Nusselt number we have a 22% increase in pumping power which is not quite desirable. Therefore, the design of a cooling system should look into both of these quantities to find an optimum solution for any given application.

Chapter 3 Effects of Protrusions in a Microchannel for Conjugate Heat Transfer with Uniform or Discrete Heating

3.1 Mathematical Model

A schematic diagram of the micro tube or microchannel is shown in figure 1(a). The length of the tube is divided into five sections and heat is supplied in three different configurations as shown in figure 3.1 (a). In case I, all the sections are heated. In case II sections 1, 3, and 5 are heated and in case III sections 2 and 4 are heated. The total length of the tube or channel is "L" and its wall thickness is "t". Figure 3.1(b) shows the various geometries of the protrusions investigated. In case of multiple protrusions, they are equally spaced around the center protrusion with a spacing "s". The liquid coolant enters with a uniform velocity w_{in} and uniform temperature T_{in}. The flow is assumed to be incompressible, laminar and steady. The properties of solid materials such as were obtained from [43] and assumed to remain constant over the working temperature range. The fluid properties were assumed to vary with temperature. The properties of water and R-134a were obtained from [44] and [45] respectively and correlated as a function of local temperature according to the following equations. For water between 293 K < T < 400 K; $Cp_f = 9.5x10^{-3}T^2 - 5.9299T + 5098.1$; $k_f = -7.0x10^{-6}T^2 + 5.8x10^{-3}T - 0.4765$; $\rho_f = -2.7x10^{-3}T^2 + 1.3104T + 848.07$; and $\ln(\mu_f) = -3.27017 - 0.0131T$. For R-134a between 230 K < T 360 K; $Cp_f = 1x10^{-4}T^2 - 0.0493T + 7.6462$; $k_f = 0.0003T^2 - 0.5937T + 234.62$; $\rho_f = -0.0224T^2 + 9.0255T + 5.18.72$; $\ln(\mu_f) = -0.014217T + 4.880646$.

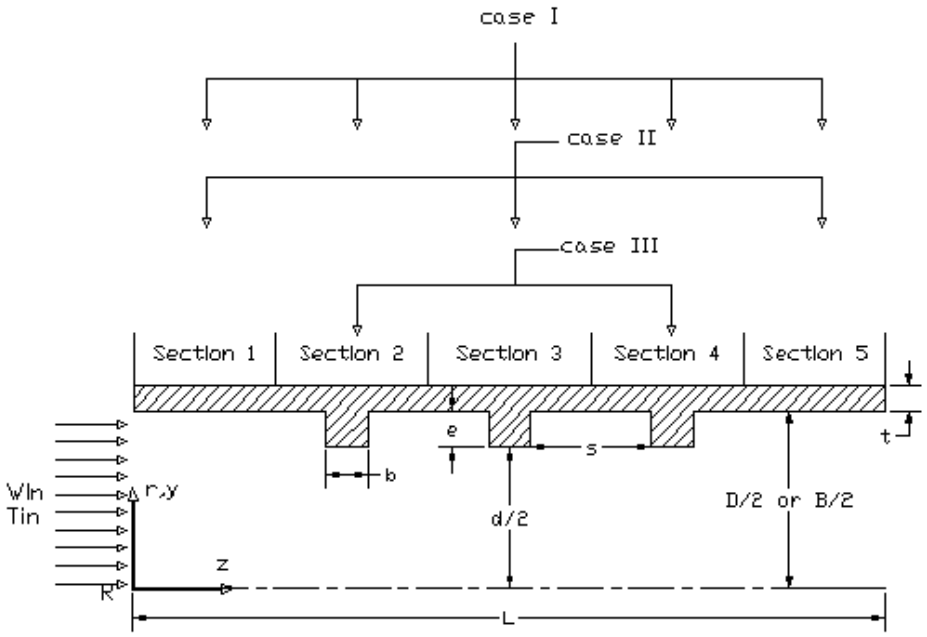

(a)

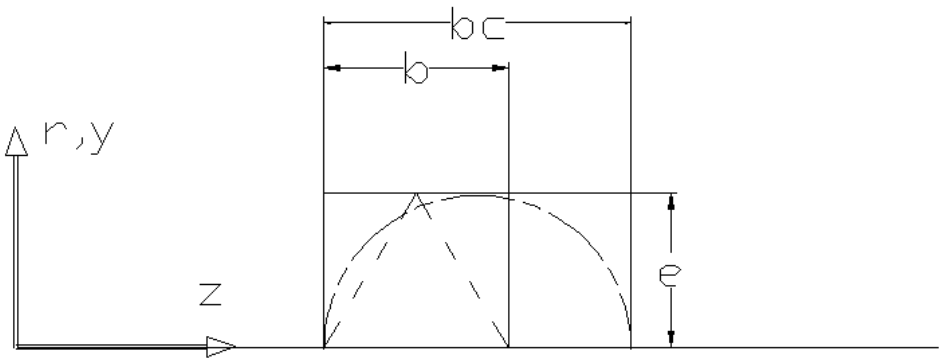

(b)

Figure 3.1 Schematic diagram of the physical problem. (a) Microchannel (microtube) cross-section, (b) Enlarged view of the various shapes of the obstructions used.

The applicable equations for the conservation of mass, momentum, and energy for

in the vector form are [44],

$$\nabla .\left(\vec{V}\right) = 0 \tag{3.1}$$

$$\rho\left(\vec{V}\cdot\nabla\right)\vec{V} = -\nabla P + \mu\nabla^{2}\vec{V} \tag{3.2}$$

$$\rho C_p \left(\vec{V} \cdot \nabla\right) T_f = \nabla \cdot k \nabla T_f \tag{3.3}$$

The energy conservation equation for solid can be expressed as [43],

$$\nabla^2 T_s = 0 \tag{3.4}$$

The boundary conditions for the fluid flow in microtube are:

At $z = 0$, $0 \le r < D/2$ or $0 \le y < B/2$: $v_r = 0$ or $v = 0$, $w = w_{in}$, $T = T_{in}$ (3.5)

At $z = L$, $0 \le r < D/2$ or $0 \le y < B/2$: $P = 0$. (3.6)

At $0 \le z \le L$, $r = 0$, or $y = 0$: $v_r = 0$, $\frac{\partial w}{\partial r} = 0$, $\frac{\partial T}{\partial r} = 0$ or $v = 0$, $\frac{\partial w}{\partial y} = 0$, $\frac{\partial T}{\partial y} = 0$. (37)

At $z=0$, $D/2<r<D/2+t$ or $B/2<y<B/2+t$: $\frac{\partial T_s}{\partial z} = 0$ (3.8)

At $z=L$, $D/2<r<D/2+t$ or $B/2<y<B/2+t$: $\frac{\partial T_s}{\partial z} = 0$ (3.9)

At $0 \le z \le L$, solid-fluid interface: $\vec{V} = 0$, $T_f = T_s$, $k_f \frac{\partial T_f}{\partial n} = k_s \frac{\partial T_s}{\partial n}$ (310)

At $0 \le z \le L$, $r = D/2+t$ or $y = B/2+t$: $\frac{\partial T_s}{\partial r} = q_w$ or $\frac{\partial T_s}{\partial y} = q_w$ (heated sections), $\frac{\partial T_s}{\partial r} = 0$ or

$\frac{\partial T_s}{\partial y} = 0$ (unheated sections) (3.11)

Here "n" is the coordinate normal to inner tube or protrusion surface. It may be noted that viscous dissipation and pressure work terms were neglected in the energy conservation equation (3). These terms are significant when fluid velocity and Prandtl number are large. For the conditions considered in the present investigation ($w_{in} < 2.15$ m/s and $Pr < 7$), these effects are expected to be negligible.

3.2 Numerical Simulation and Parametric Study

The governing equations along with the boundary conditions were solved using the Galerkin finite element method. Four node quadrilateral elements were used in the fluid region. In each element, the velocity, pressure, and temperature fields were approximated which led to a set of equations that defined the continuum. The Newton-Raphson algorithm was used to solve the nonlinear system of discretized equations. An iterative procedure was used to arrive at the solution for the velocity and temperature fields. The solution was considered converged when the field values became practically constant and the relative change from one iteration to the next reduced below 10^{-6}.

The distribution of cells in the computational domain was determined from a series of tests with different number of elements. The simulations were conducted by maintaining the aspect ratio (the ratio of the element lengths in the z-direction to the r- or y-direction) was maintained greater than 1 and less than 8.

Grid independence tests were conducted by generating results for two cases; the first one being the pipe containing the rectangular obstruction of e=0.05D, and the other for the parallel plates with the rectangular obstruction of e=0.05B using different mesh sizes in each case as shown in (Section 2.2) Chapter 2. In addition an energy balance was done by comparing the amount of energy entering the system which includes the heat flux being supplied at the outer wall with the energy carried away by the working fluid determined from the average fluid temperature at the inlet and exit. The difference was within 0.26 % between the values of the energy entering the system and leaving the system.

3.3 Results and Discussions

As stated above we consider three different heating cases for both microtube and two-dimensional microchannel. In case I a constant heat flux is applied to all the sections resulting in uniform heating. Sections 1, 3, and 5 are heated in case II, Section 3 is part of the tube where the protrusion is present (for a single protrusion case). In this case, Sections 2 and 4 are not heated (insulated). For case III of heating in which the Sections 2 and 4 are supplied with a constant heat flux and the Sections 1, 3 and 5 are kept insulated. Magnitude of heat flux was adjusted for each of the discrete heating cases in order to make the same total heat input for all the cases.

Figure 3.2 compares local Nusselt number variation along the length of the microchannel and microtube with rectangular protrusion for all the three heating cases. In figure 3.2 (a), we see that in heating case I which has all the sections of the microtube heated has a gradual decrease in Nusselt number until the protrusion is encountered. At the location where the protrusion is located there is a rapid fall in the value of the local Nusselt number due to the flow is interrupted by the presence of the protrusion and the fluid moves away from the heated wall to go over the protrusion. At the leading edge of the protrusion there is a gradual increase of local Nusselt number along the front wall. At the top front corner, the value of local Nusselt number is the highest because the momentum and the thermal boundary layers begin to form again using the corner of the protrusion as the leading edge. As the boundary layer thickness increases we can see a gradual decrease of Nusselt number until the flow reaches the trailing corner. Then at the rear wall of the protrusion, we observe a gradual fall in local Nusselt number due to expansion of the flow and associated recirculation. Starting with the bottom trailing edge

of the protrusion, Nusselt number gradually increases downstream in the recirculating region following the protrusion. Then the local Nusselt number value recovers to the trend followed by the smooth microtube or channel. In heating case II where the value of local Nusselt number dips at x/L=0.2 because the section from x/L=0.2 and x/L=0.4 is not heated and then the curve loops up as the heat flux is applied at Section 3 i.e. x/L=0.4 to x/L=0.6. Section 3 is where the protrusion is located and we see similar behavior in variation of the value of local Nusselt as see in case I. In Section 4 the value of Nusselt number goes down as we don't have heating at this section. And again the value of Nusselt Number goes up in Section 5. At the protrusion the jump in the value of local Nusselt number is higher than as observed in case I, this is due to the localized heating at the Section 3 which is where the protrusion is located.

In Case III as the Section 2 is heated the Nusselt number increases at x/L=0.2 and then falls a little at x/L=0.4. At the protrusion the values of Nusselt number is lower than that of Cases I and II, but follows the same trend in the increase of value of local Nusselt number. As opposed to case II in Case III we observe that the value of Nusselt number goes up in the Section 4 due to the fact that the heat flux is applied at that section and in the Section 5 which starts from 0.8 we see the value of Nusselt number goes down as there is no heat flux being applied at that section.

Figure 3.2 (b) shows the variation of local Nusselt number for two-dimensional microchannel for the same three heating cases. The local Nusselt number variation exactly identical to the trend observed in the microtube, the only difference is that the value of local Nusselt number is approximately twice that of the microtube.

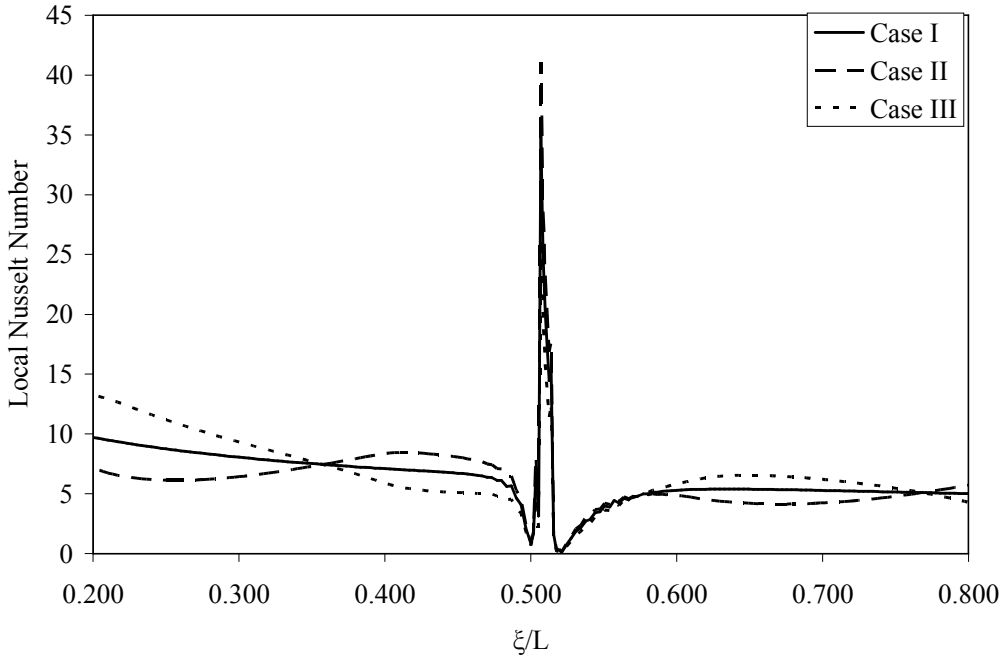

(a)

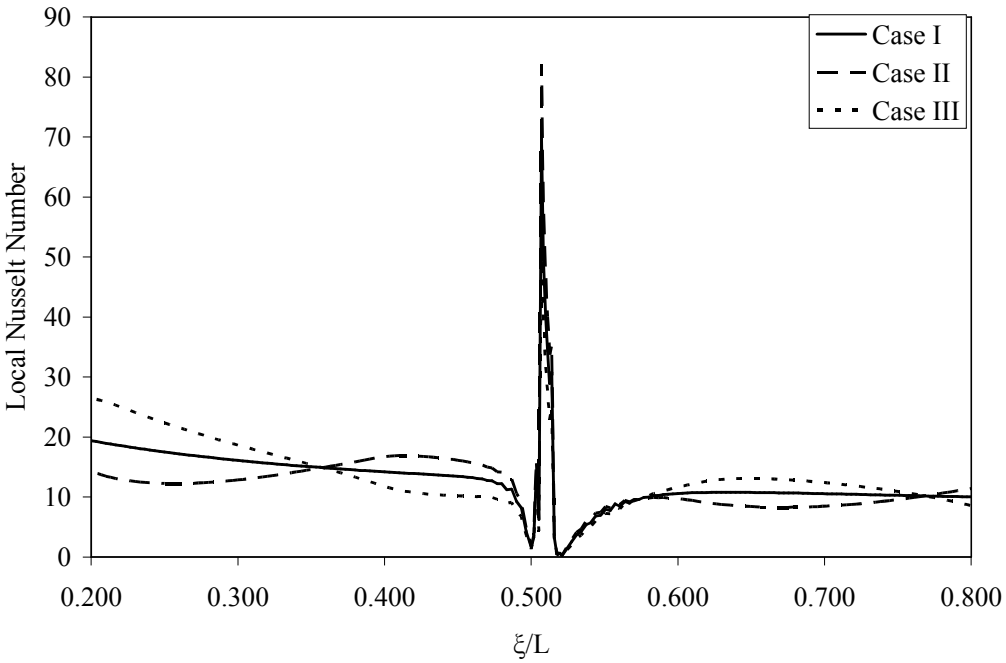

(b)

Figure 3.2 Local Nusselt Number variation for different heat input scenario using water as the coolant, Re=500. a) Microtube, (b) Microchannel.

3.3.1 Shape of the protrusion

Figure 3.3 shows the variation of local Nusselt number along various geometries of the protrusions such as rectangular, triangular, and semicircular protrusions compared with the smooth microtube case for all the three heating cases. Figure 3.3 (a) shows the local Nusselt number variation for various shapes for heating case I where the heat flux is applied all along the wall of the microtube. Here the rectangular protrusion starts at $\xi/L=0.5$ and ends at $\xi/L=0.521$, triangular protrusion starts at $\xi/L=0.5$ and ends at $\xi/L=0.5156$ and the semicircular protrusion starts at $\xi/L=0.5$ and ends at $\xi/L=0.5218$. In all the protrusion shapes we observe that there is a drop in the local value of Nusselt number before the beginning of the protrusion because the flow is interrupted by the presence of the protrusion and the fluid moves away from the heated wall to go over the protrusion. This creates a small recirculation region before the protrusion where the heat transfer rate falls below the smooth microchannel. For the rectangular shaped protrusion, there is a gradual increase of local Nusselt number along the front wall followed by an abrupt increase as we reach the top wall of the protrusion. On the top wall of the protrusion we can see a gradual decrease of Nusselt number until the flow reaches the trailing corner. At the rear wall of the protrusion, we observe a gradual fall in local Nusselt number due to expansion of the flow and associated recirculation. Starting with the bottom trailing edge of the protrusion, Nusselt number gradually increases downstream in the recirculating region following the protrusion.

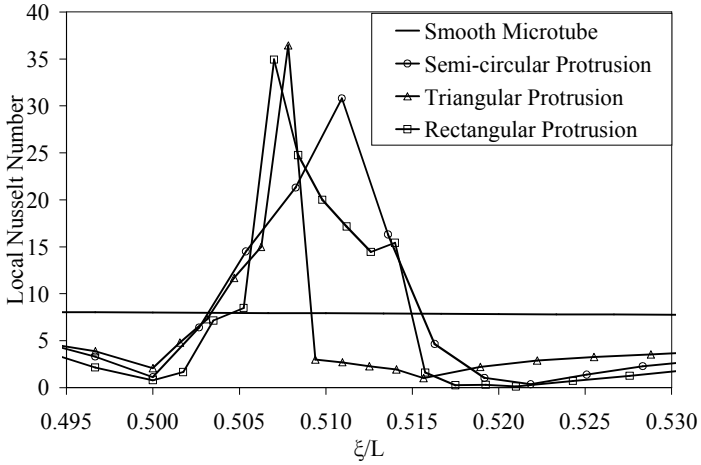

(a)

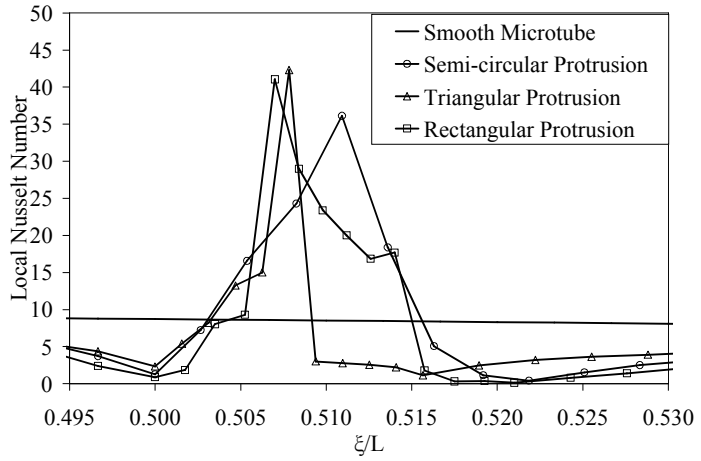

(b)

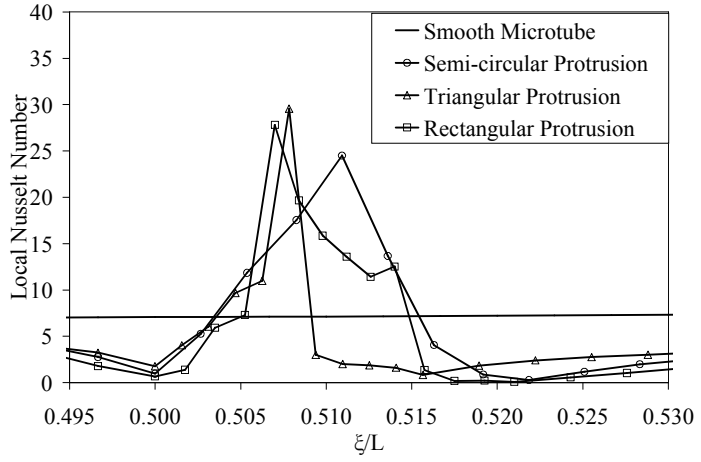

(c)

Figure 3.3 Local Nusselt number along stream wise direction for rectangular, triangular and semi-circular obstruction using water as the working fluid in microtubes, Re=500. (a) Heating case I, (b) Heating case II, (c) Heating case III.

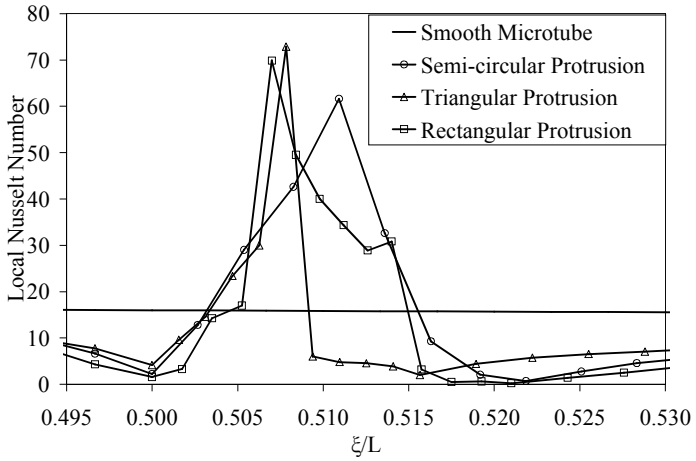

(a) Heating case I

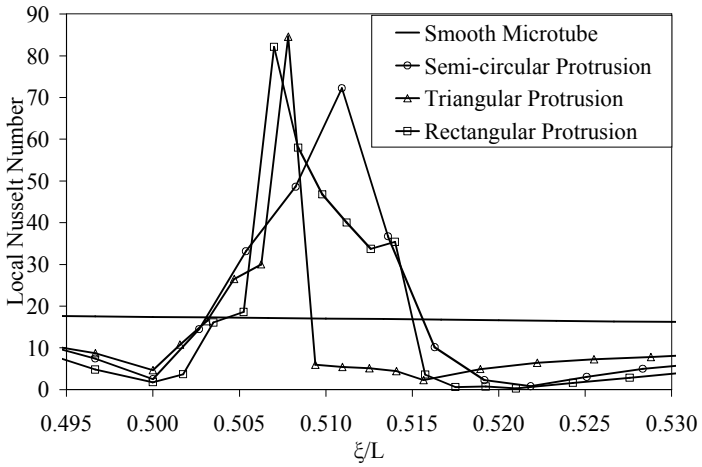

(b) Heating case II

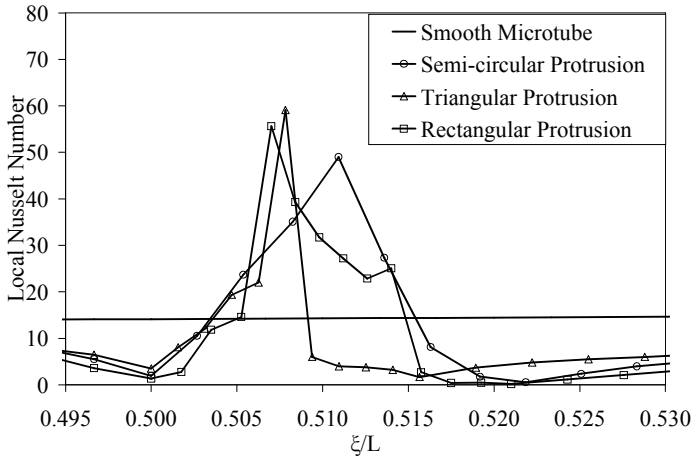

(c) Heating case III

Figure 3.4 Local Nusselt number along stream wise direction for rectangular, triangular and semi-circular obstruction using water as the working fluid for microchannels, Re=500**.** (a) Heating case I, (b) Heating case II, (c) Heating case III.

In the case of the triangular shaped protrusion we see a steady increase in the value of local Nusselt number as the cross-sectional area of the flow decreases and local fluid velocity increases in the direction of the flow. A peak is seen at the vertex of the triangle. At the downstream side of the triangle, the Nusselt number first decreases abruptly and then gradually. The sharp corner directs the main flow to a larger distance downstream and the rear wall of the protrusion is essentially occupied by the recirculating flow. A minimum is seen at a location just downstream from the protrusion. Further downstream, the Nusselt number increases gradually. For the case involving the semicircular protrusion, the rise and fall of local Nusselt number along the protrusion is quite gradual showing much smoother transition compared to the other two shapes of the protrusion. The maximum Nusselt number is seen at the tip of the semi-circle where the flow area is minimal. When the inlet velocity of the fluid was increased to obtain higher Reynolds numbers, we saw an increase in the magnitude of the Nusselt number at the location of the protrusion. The distribution pattern, however, remained the same

Figure 3.3 (b) shows the variation of local Nusselt number for heating case II in which the heat flux is applied at sections 1, 3, and 5 and the protrusion is located at section 3. Here we see that the value of local Nusselt number jump at all the three protrusion shapes is higher that that compared to the other two heating cases, this is again due to fact that the heat flux is discretely applied at the protrusion and in the heated portion of the tube immediately preceding the protrusion, the Nusselt number is higher compared to case I because of the development of a new thermal boundary layer. Figure 3.3 (c) shows the local Nusselt number variation for the third heating case where the heat flux is applied at the section away from the location of the protrusion, i.e. sections 2 and

4. Here the peak Nusselt number came out to be lower because of lower Nusselt number compared to other cases immediately before the protrusion. It may be also noted that heat is transferred by axial conduction in the tube and eventually dissipated by convection from the inner walls of the tube and the protrusion.

Figures 3.4 (a), (b), and (c) shows the variation of local Nusselt number for various geometries of protrusions in two-dimensional microchannels compared with the smooth microchannel. Here we observe the same trend as seen in the case of microtube, but the value of the Nusselt number is relatively higher that that observed in the microtube.

3.3.2 Size of protrusion

The effect of various sizes of the protrusion on circular microtubes and microchannels for the three heating cases can again be interpreted by comparison of local Nusselt number. Here, we varied two parameters height "e" and width "b" of the protrusion. Figure 3.5 shows the obstruction size effect on local Nusselt number in circular microtube case. Figure 3.5 (a) shows the variation of local Nusselt number along the stream wise direction for constant width with b/D=0.05 for the heating case I were a constant heat flux is applied all along the length of the tube. We see that as the height of the obstruction increases the value of local Nusselt number also increases. The highest Nusselt number for each case is seen at the top front corner. This is due to the formation of both thermal and momentum boundary layers at the top of the protrusion with the front top corner as the leading edge. With the increase of obstruction size i.e. "e/D", the flow cross-sectional area reduces and causes a larger velocity of flow in the obstruction area. This enhances the local convection heat transfer coefficient. A larger "e/D" however,

means a larger jump for the flow and longer recirculation region before and after the obstruction, in those areas, Nusselt number decreases with increase of "e/D". Figure 3.5 (b) shows the streamwise local Nusselt number variation for the heating case II where sections 1, 3, and 5 are heated and the protrusion is located in the middle of the 3rd section. Here again we observe similar local Nusselt number variation as see in heating case I but the value maximum Nusselt number is greater than in the previous case. Figure 3.5 (c) shows the variation of local Nusselt number along the stream wise direction for the heating case III in which the heat flux is not applied to the section where the protrusion is located. Here, also we see the same trend being followed in the variation of the value of local Nusselt number is the same as seen in figures 6 (a) and (b), but the only difference is that the jump in the value of local Nusselt number of each height is lesser than in cases I and II, this is due to the fact that there is no heat flux being applied at the section where the protrusion is located.

Figure 3.6 (a) shows the variation of local Nusselt Number along the stream wise direction for constant height "e/D"=0.05 and the value of "b/D" varying from 0.05 to 0.1 for heating case I where the heat flux is applied all along the length of the microtube. Here, we can notice the value of local Nusselt number remains the same for all three obstructions until the trailing edge of an obstruction is approached. Different values in recirculation region downstream of the protrusion are primarily due to different locations for the start of the new thermal boundary layer.

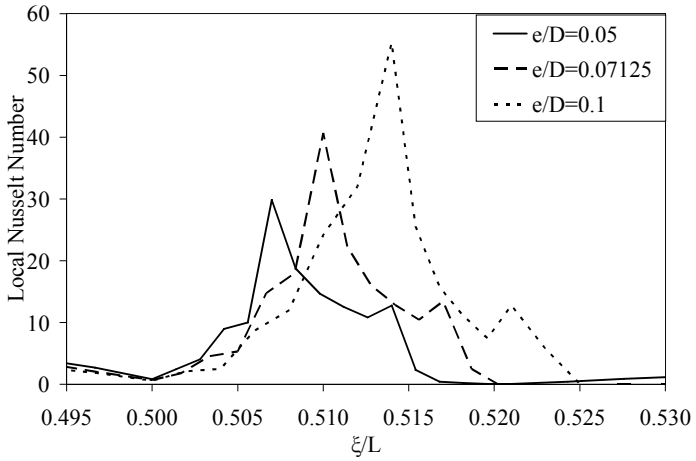

(a)

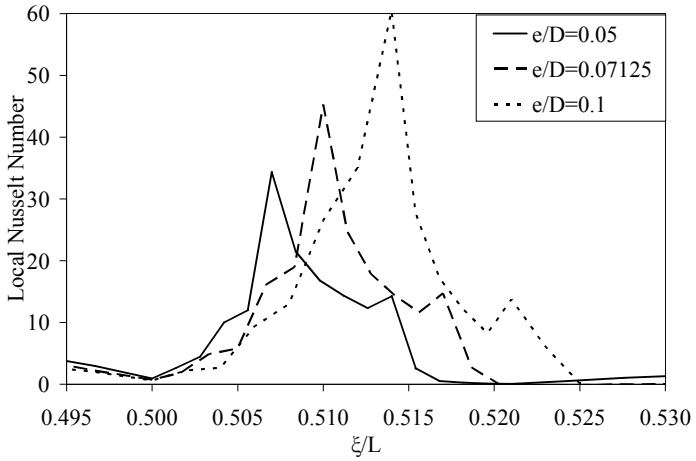

(b)

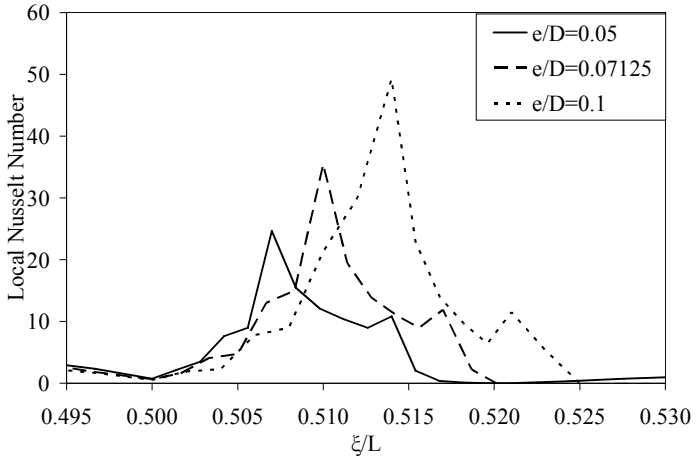

(c)

Figure 3.5 Local Nusselt number when varying height 'e' from 0.05D to 0.1D keeping 'b' constant for rectangular protrusion when water is the working fluid in microtubes, Re=500. (a) Heating case I, (b) Heating case II, (c) Heating case III.

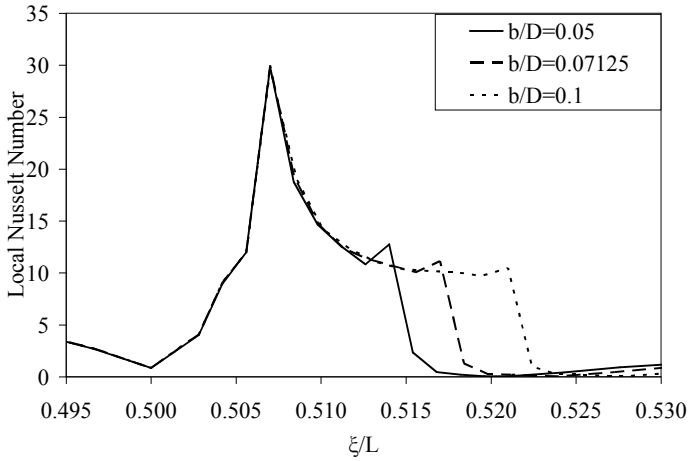

(a)

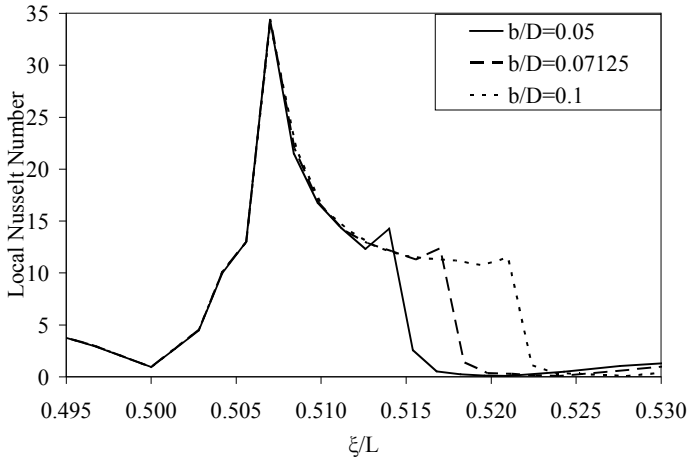

(b)

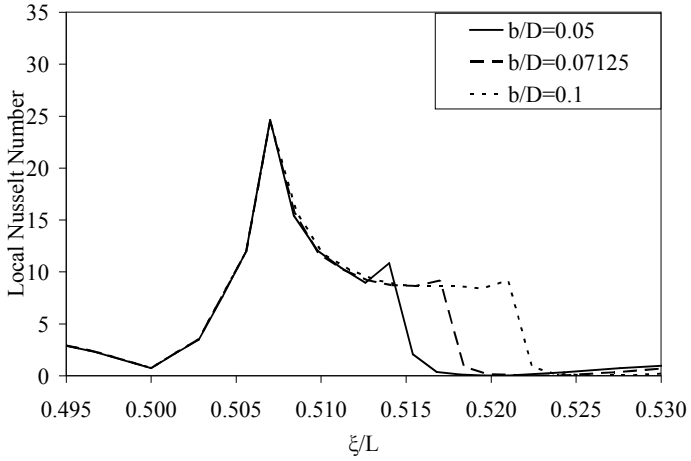

(c)

Figure 3.6 Local Nusselt Number when varying width 'b' from 0.05D to 0.1D keeping 'e' constant for rectangular protrusion when water is the working fluid in microtubes, Re=500. (a) Heating case I, (b) Heating case II, (c) Heating case III.

Figure 3.6 (b) shows the variation of local Nusselt number along the stream wise direction for the heating Case II in which the heat flux is applied at the section where the protrusion is located. Figure 3.6 (c) shows the variation of local Nusselt number along the stream wise direction for the heating case III in which the heat flux is not applied to the section where the protrusion is located. Here, again we see the same trend being followed in the variation of the value of local Nusselt number is the same, but the difference is that the jump in the value of local Nusselt number is lowest in heating case III as compared to the other two heating cases, because there is no heat flux being applied in this case at the location of the protrusion. Heating case II produces the highest value of local Nusselt number as compared to the other two cases; this is because there is a discrete heat flux being applied at the section of the microtube where the protrusion is located.

3.3.3 Wall thickness

All the above results obtained were for the wall thickness of 100 μm i.e. t/D = 0.1428, now we increased the wall thickness to 200 μm (t/D = 0.28571), 400 μm (t/D = 0.5714) and 700 μm (t/D = 1). Figures 3.7 (a), (b), and (c) show the variations of local Nusselt number for different wall thicknesses used in the circular microtube with a rectangular protrusion at 3rd section, for the three heating cases. Figure 3.7 (a) shows the variation of local Nusselt number for the case I where the heat flux is applied uniformly all along the protrusion. We observe a steady decrease in the value of jump in Nusselt number at the start of the protrusion as the wall thickness increases. This is due of the smoothening effect of the wall of the microtube because as the wall thickness is increased the distance the heat has to travel to the inner wall is increased and thus the heat gets

evenly conducted in the solid media, thus causing the reduced temperature gradient and in turn the reduced local Nusselt number value.

Figure 3.7 (b) shows the variation of local Nusselt number at the protrusion for various thicknesses for case II where the heat flux is applied at the protrusion. Here we see that there is a similar decrease in the jump of value of Nusselt number at the protrusion but the maximum value reached for the case with t/D = 0.1428 is higher than the value see in figure 3.7 (a) for the first case. In figure 3.7 (c) we see the local Nusselt number variations at the protrusions for various thicknesses for case III, where there is no heat flux being applied at the protrusion. This can be explained by the fact that in case II the heat flux is applied at the section where the protrusion is located and in heating case III heat flux is applied at the 2^{nd} and 4^{th} sections which are located on either side of the section containing the protrusion. And also the distance traveled by the heat is larger which causes the temperature gradient at the inner wall i.e. the solid-fluid interface to be lower than in case II causing the reduction in the value of local Nusselt number. Here, we also observe that the decrease in the value of local Nusselt number is not as distinct as seen in heating case II for the microtubes with t/D = 0.1428, t/D = 0.28571 and the t/D = 0.5714. But when we compare the microtube with t/D = 1with the other three microtubes we see a lower value of local Nusselt number, because again the heat has to travel a larger distance when compared to the other three microtubes. Figure 3.8 shows the variation of local Nusselt number for different wall thicknesses used in the two-dimensional microchannel with rectangular protrusion at 3^{rd} section for the three heating cases. Here we see similar behavior as seen in the microtube but the value of local Nusselt number is almost twice as that of the value seen in the microtube case.

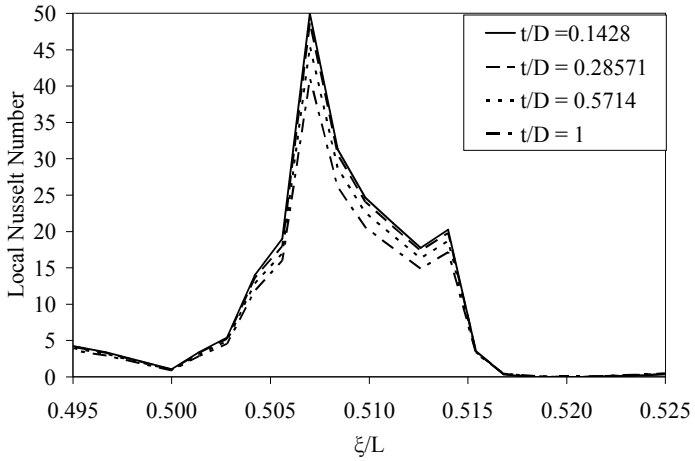

(a)

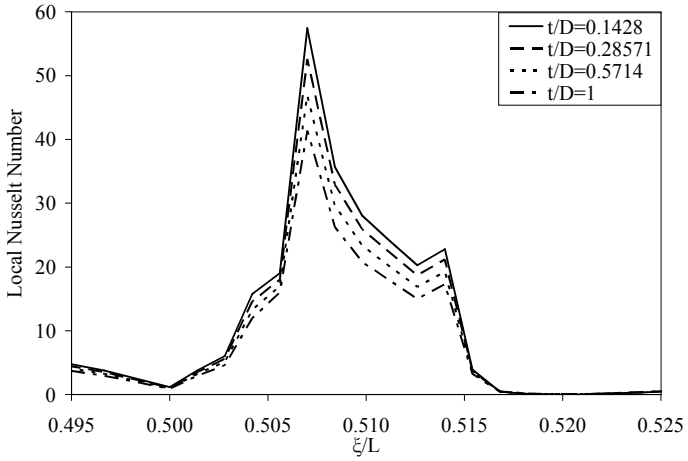

(b)

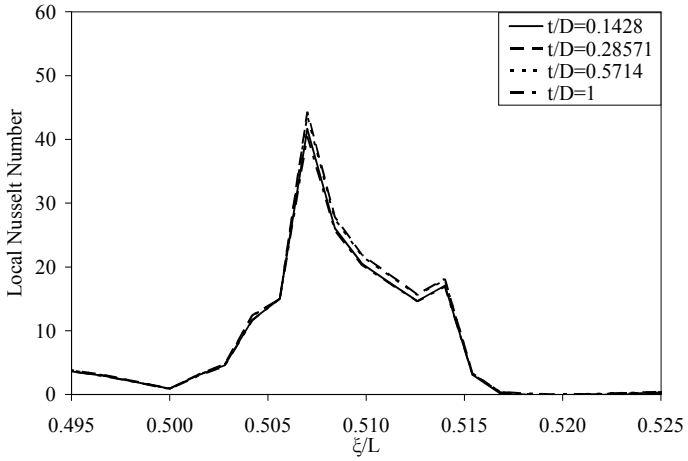

(c)

Figure 3.7 Local Nusselt number variation with wall thickness in aluminum microtubes with water as working fluid, Re=500.
(a) Heating Case I, (b) Heating Case II, (c) Heating Case III.

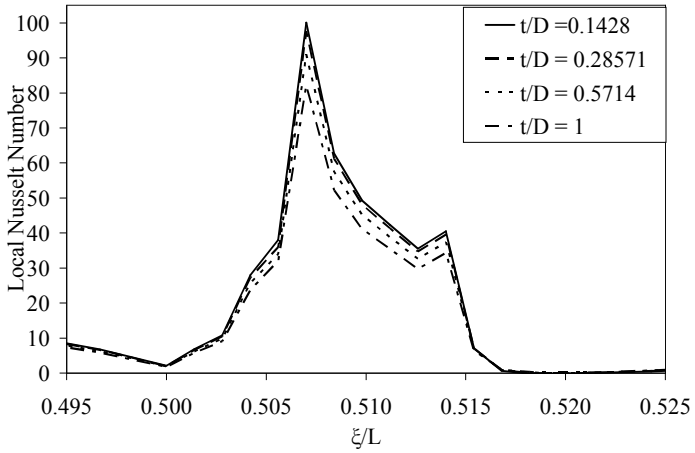

(a)

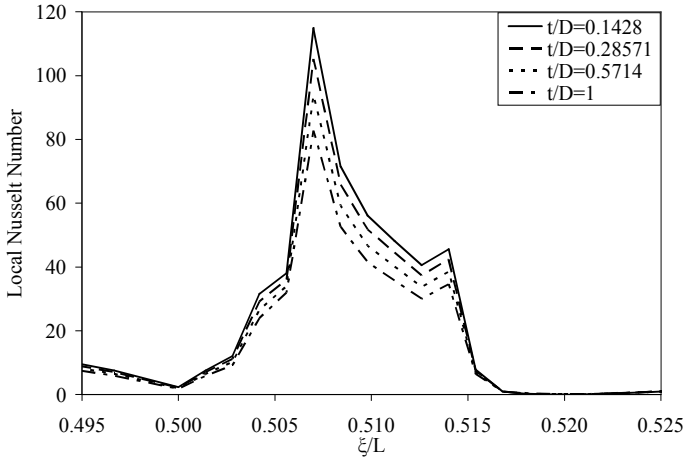

(b)

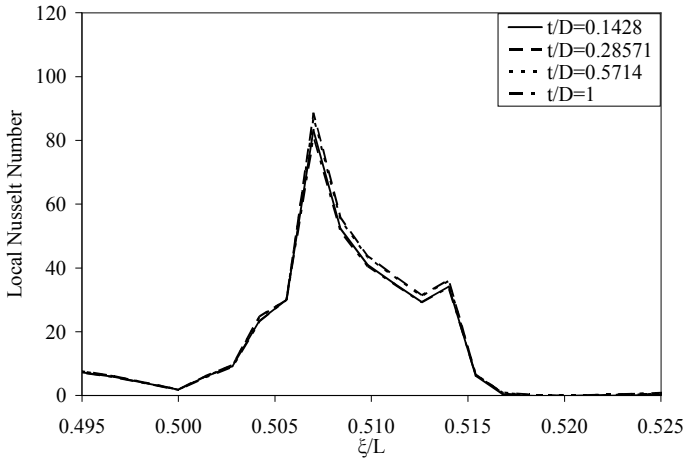

(c)

Figure 3.8 Local Nusselt number variation with wall thickness in aluminum microchannels with water as working fluid, Re=500.
(a) Heating Case I, (b) Heating Case II, (c) Heating Case III.

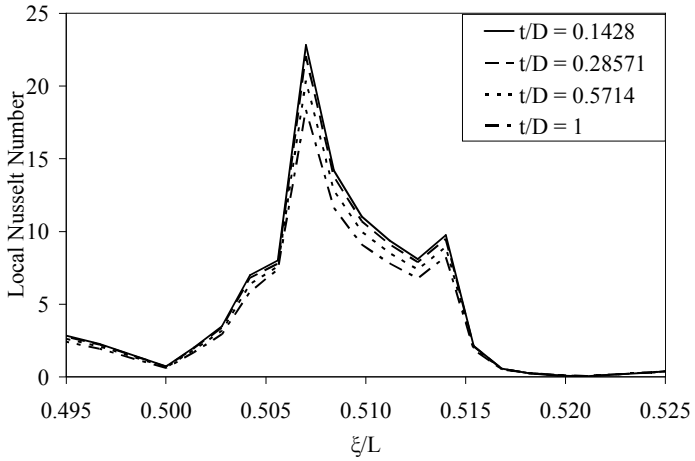

(a)

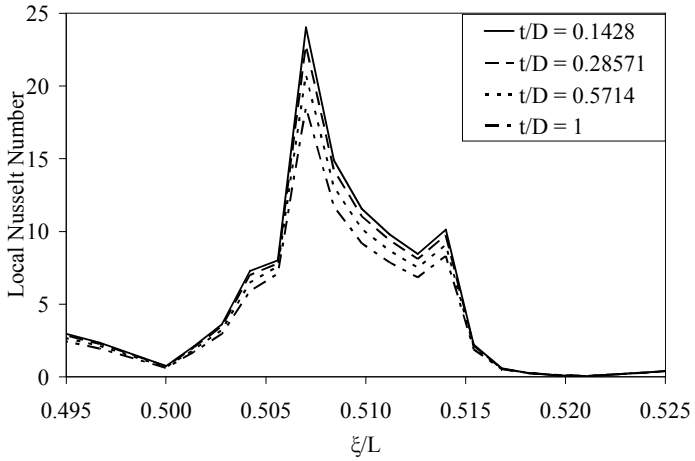

(b)

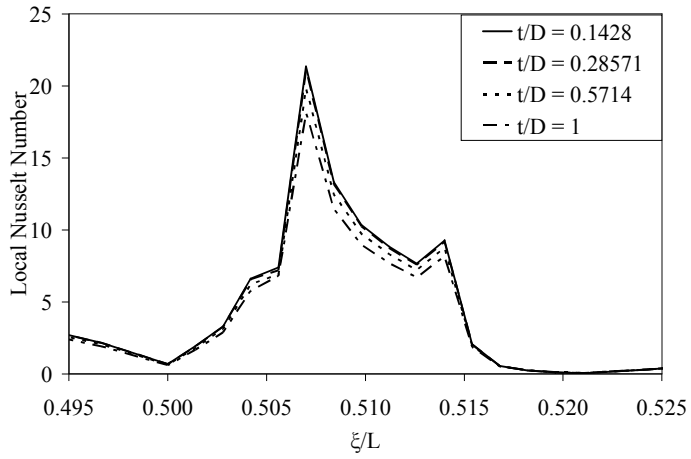

(c)

Figure 3.9 Local Nusselt number variation with wall thickness in aluminum microtubes with refrigerant R-134a as working fluid, Re=500.
(a) Heating Case I, (b) Heating Case II, (c) Heating Case III.

Similar trend of the reduction of local Nusselt number was observed when the working fluid was changed from water to a lower Prandtl number fluid refrigerant R-134a as shown in figures 3.9 (a), (b), and (c). The only difference from what seen before is the value of local Nusselt number is lesser than the value observed in microtubes with water as working fluid. This behavior can again be attributed to the larger distance traveled by the heat from the outer wall to inner solid-fluid interface or the inner wall and also the lower Prandtl number of the refrigerant R-134a when compared to water.

3.3.4 Number of protrusions

Till now we have seen the effect of a single protrusion on the Nusselt number. Now we consider more than one protrusion in the flow path. For this we consider two configurations, the first configuration consists of three protrusions and the second configuration consist of five protrusions in both cases equally spaced along the length of the microtube or microchannel. Now considering the three protrusion configuration for the rectangular protrusion, for all three heating cases as shown in figure 3.10 (a) for Aluminum as the material of the microtube. Here we see that the local Nusselt number peaks at the top front corner of the protrusion similar to case of the single protrusion. But the value of the local Nusselt number at the start of the protrusion goes on decreasing along the length even though the protrusions are of the same height and width. This is because of the larger bulk fluid temperature as the flow moves downstream. Here we see that the heating case I has the mean variation of local Nusselt number with respect to the other two heating cases.

All the above results were obtained for microtubes made of aluminum which has relatively high thermal conductivity and relatively low density, which makes it most

appropriate metal to be used in heat-exchangers because it keeps the weight of the heat-exchanger low and also dissipates well due to high thermal conductivity. Now we use bronze which is an alloy of Copper with small amount of Tin added to enhance its hardness which has good thermal properties but relatively low thermal conductivity when compared to aluminum. Figure 3.10 (b) shows the variation of the value of local Nusselt number along the streamwise direction of the microtube containing three rectangular protrusions made of Bronze and having a t/D = 0.1428 and using water as the working fluid for all the three heating cases. Here we see that in heating case II in which the heat flux is supplied at the section where the protrusion is located has a higher value of Nusselt number at the start of the protrusion than the value observed in heating case III where the heat flux is not applied at the section where the protrusion is located. We observe that the difference in the value is quite large, this large difference can be attributed to the fact that the thermal conductivity of the alloy Bronze is relatively lower when compared the thermal conductivity of Aluminum. Due to this lower thermal conductivity of the alloy Bronze the heat does not get evenly distributed from the 2^{nd} and 4^{th} section which are heated in heating case II, thus causing the gradient in temperature at the protrusion to be quite small resulting in a lower local value of Nusselt number when compared to the microtube made of Aluminum as shown in figure 3.10 (a).

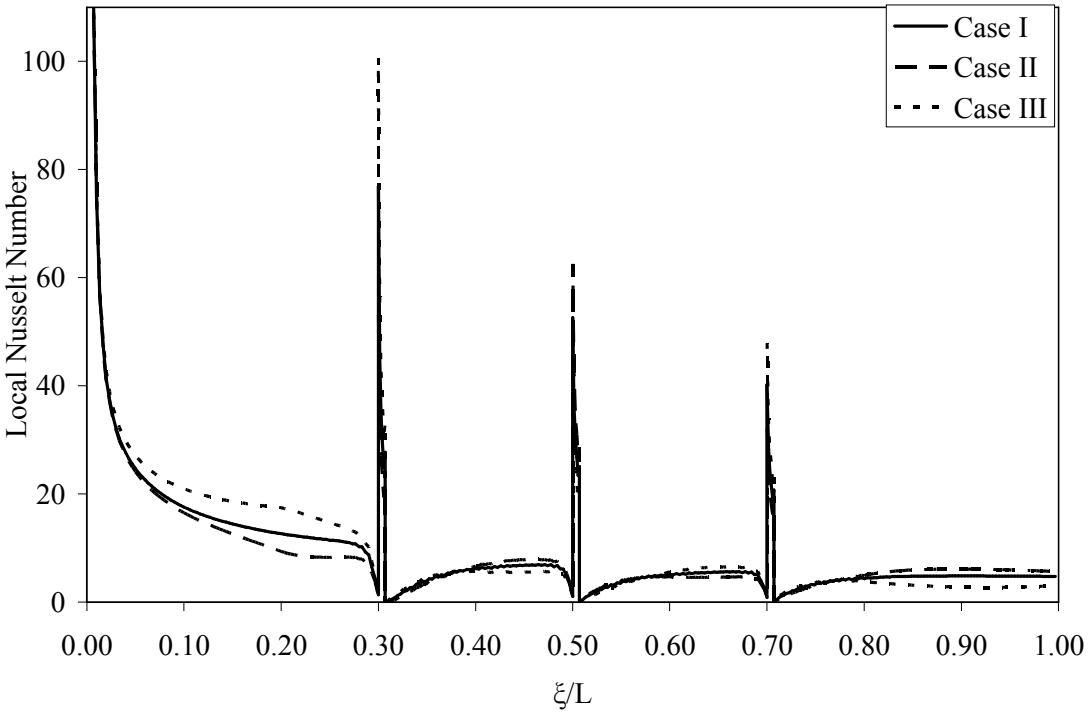

(a)

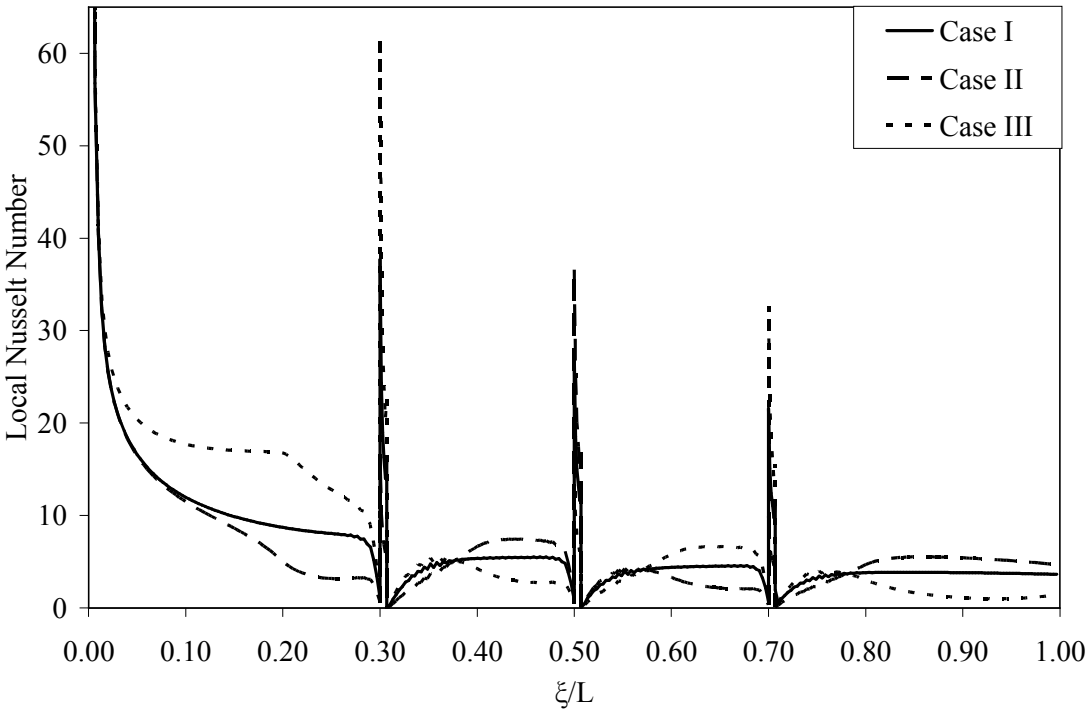

(b)

Figure 3.10 Local Nusselt number microtubes with three protrusions for water as working fluid for different materials, Re=500.
(a) Aluminum microtube, (b) Bronze microtube.

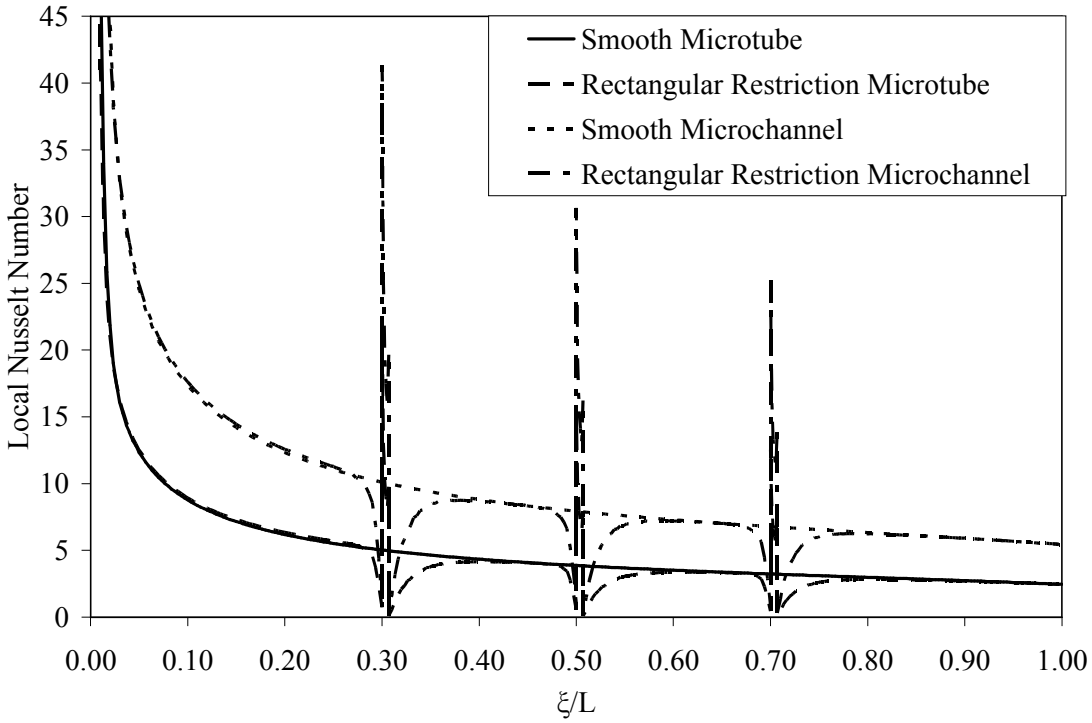

Figure 3.11 Local Nusselt number comparison for Aluminum microchannels and microtubes with three protrusions for water as working fluid, Re=500.

Figure 3.11 presents the results for the three protrusions equally spaced protrusions in the flow regime for both the microtube and microchannel compared with the smooth microtube and channel for the case where a uniform heat flux is applied all along the length of the microtube or microchannel. It can be observed that the local Nusselt number again peaks at the top front corner of the protrusion similar to case of the single protrusion. But the highest value of local Nusselt number at the protrusion goes on decreasing along the length even though the protrusions are of the same height and width. This is because of the larger bulk fluid temperature as the flow moves downstream. The local heat transfer rate is intimately related to the wall to fluid temperature difference. As wall to fluid temperature difference drops, the local heat transfer coefficient of Nusselt number drops. Another interesting observation from figure 12 is that after each protrusion

the local Nusselt number recovers to the distribution shown by smooth tube or channel. Therefore, if sufficient distance is provided between protrusions the local Nusselt number over a good portion of the tube or channel that are away from restricted areas will not be affected by the presence of the protrusion or no significant history effect of the flow. It suggests that flow protrusions can be conveniently used to trigger local enhancement with out greatly affecting the overall heat transfer pattern. A similar characteristic was seen in the case of the triangular and semi-circular protrusions.

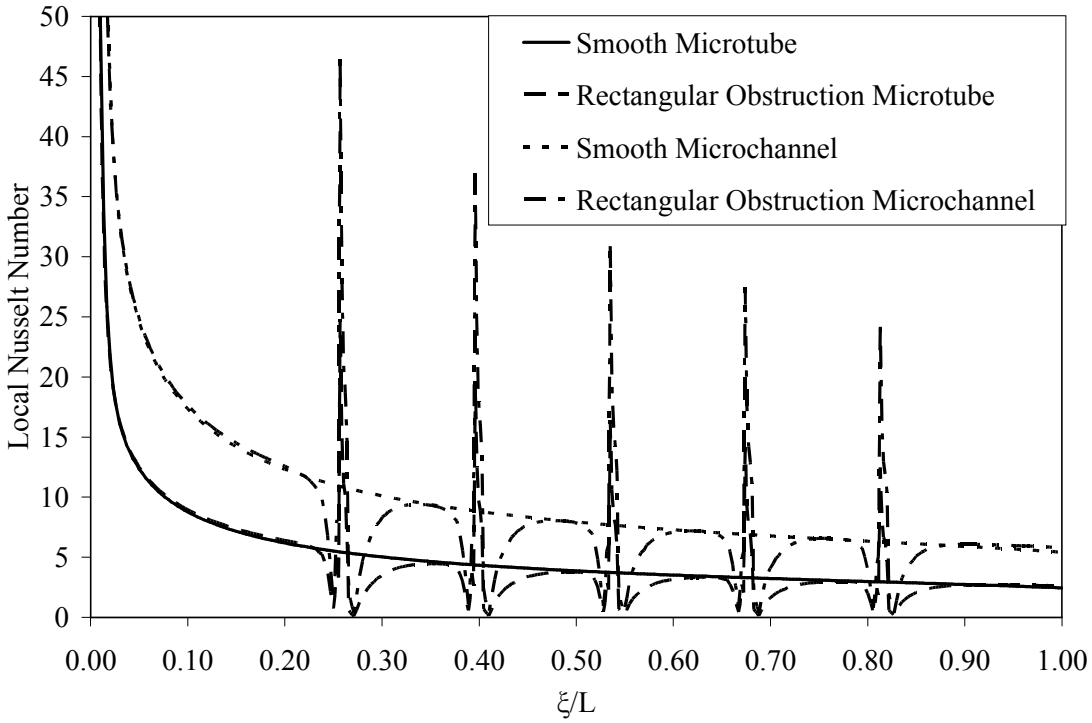

Figure 3.12 Local Nusselt number comparison for Aluminum microchannels and microtubes with five protrusions for water as working fluid, Re=500.

Figure 3.12 presents the results for the second configuration containing five equally spaced obstructions. It can be observed that the local Nusselt number variation is similar to that of the three obstruction configuration, but the distance between the consecutive obstructions is small and hence the flow just stabilizes and the momentum

and thermal boundary layers are not fully established in the region between obstructions and the flow is again disturbed, hence we see that the local Nusselt number values do just coincide with the smooth microtube or microchannel values. Due to smaller distance between protrusions, the flow cannot recover before being disturbed by the subsequent protrusion. Therefore, the number of protrusions and spacing between them has a very important role in controlling the overall heat transfer characteristic of the system.

3.3.5 Reynolds number

Until now we studied the local Nusselt number variation for microchannels and microtubes with protrusions. We will now see how the global value of Nusselt number varies for both microchannel and microtube. Global Nusselt number is calculated by taking a weighted average of all the local values of Nusselt number along the length of the microchannel or micro tube. Figure 3.13 shows the average Nusselt number for different Reynolds numbers and shapes of obstruction for the heating case I in which the heat flux is applied all along the length of the tube. Figure 3.13 (a) compares the average Nusselt number for various shapes of the obstructions with smooth tube for Reynolds numbers varying from 500 to 1500 for the circular microtube case. Here we find a reduction in the global heat transfer rate for a microtube containing the obstruction when compared to a smooth microtube. This decrease is a function of both the shape of the obstruction and the Reynolds number. The actual shape of the obstruction has an effect on the numerical values of Nu, but does not change the qualitative behavior. The decrease in the heat transfer rate is, however, more significant for the rectangular shape. This can be explained as: the global Nusselt number is a surface-weighted average of values at the peaks (higher than the smooth microtube) and at the valleys (lower than smooth microtube). The peaks

cover a lower area (smaller radius) compared to the valley (higher radius). In addition, the peak is much smaller in length compared to the length covered by two recirculating regions at the valley. Hence, the balance is shifted to a lower average Nusselt number.

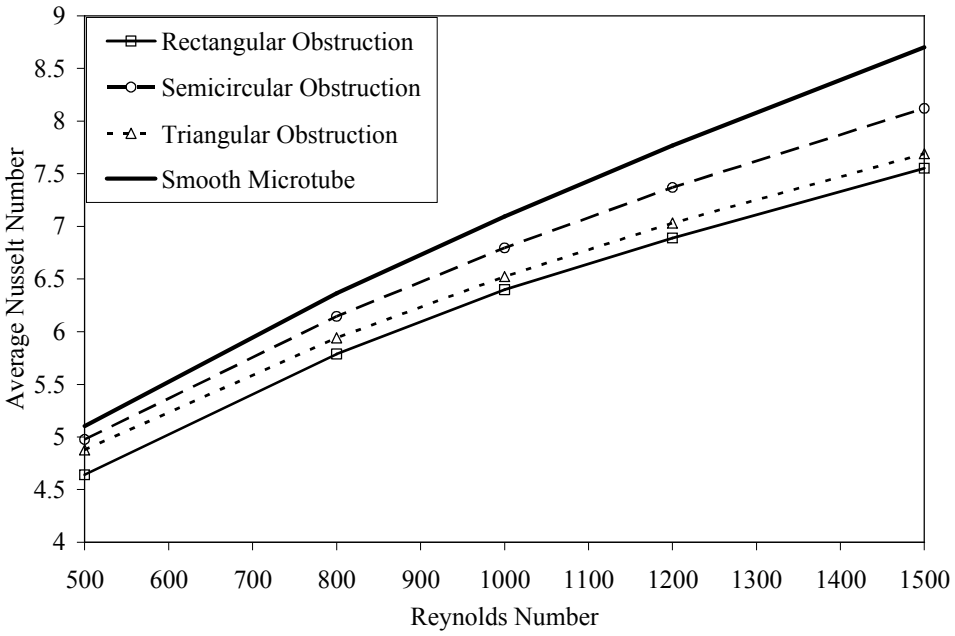

(a)

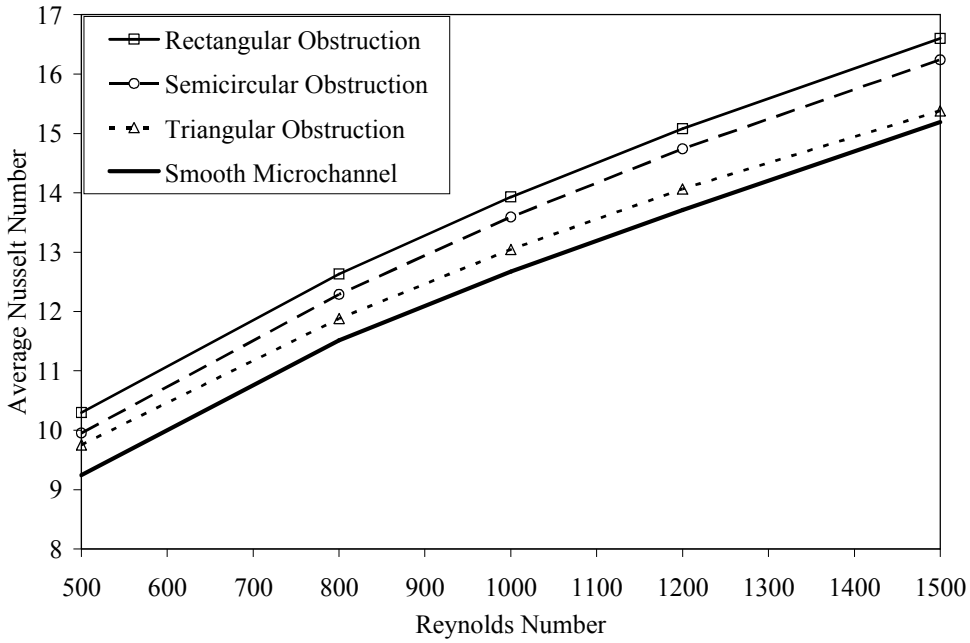

(b)

Figure 3.13 Average Nusselt number for various protrusion shapes for water. (a) Circular microtube, (b) Circular microchannel.

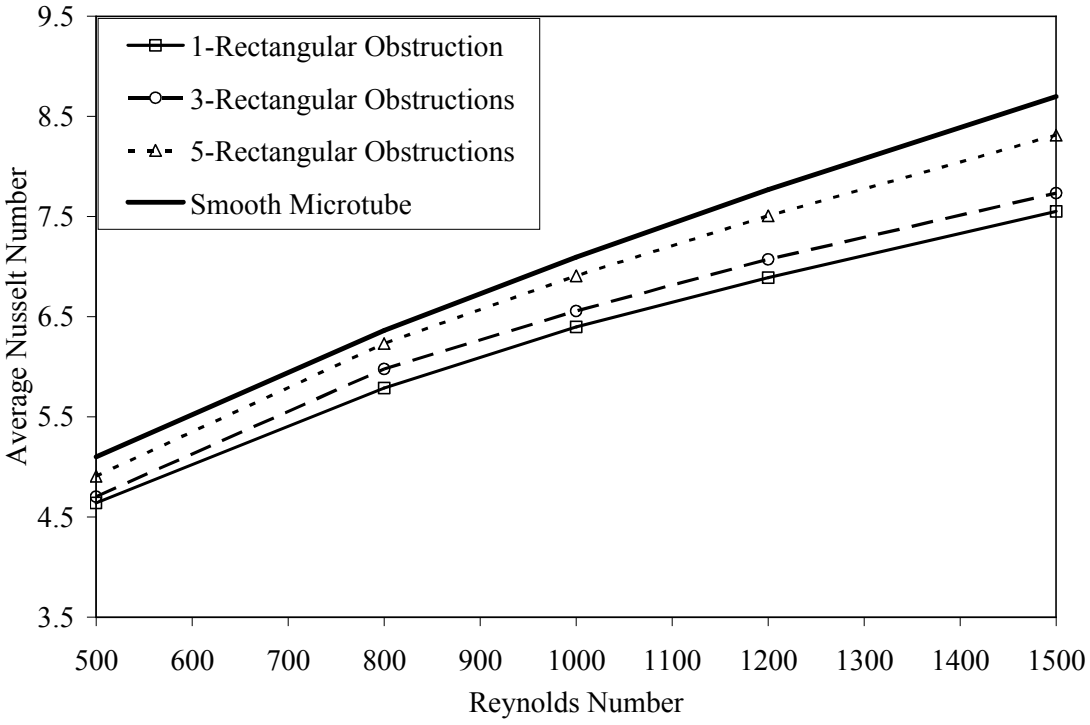

(a)

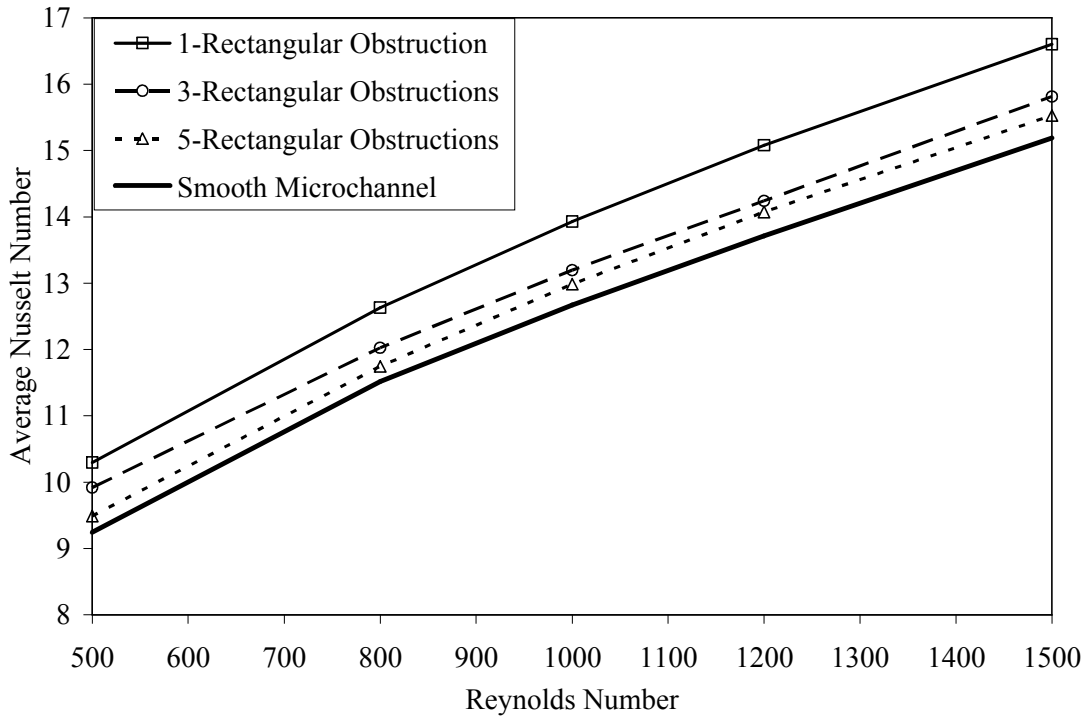

(b)

Figure 3.14 Average Nusselt number for repeated protrusions for water. (a) Circular microtube, (b) Circular microchannel.

In Figure 3.13 (b) we compare the average Nusselt number for various shapes of the obstructions in a two-dimensional microchannel with the smooth two-dimensional microchannel for Reynolds numbers varying from 500 to 1500. Here we find an increase in the average Nusselt number for channel containing the obstruction when compared to the smooth channel. This increase is again a function of both the shape of the obstruction and the Reynolds number. A rectangular protrusion provides the largest enhancement of average Nusselt number.

In Figure 3.14 (a) we see the variation of average Nusselt number for smooth microtube and the microtubes with one, three and five obstructions for heating case I. The smooth tube has the highest Nusselt Number and the other three configurations have lesser average values. But in Figure 3.14 (b) the smooth channel has the least Nusselt number when compared to the other three configurations. It can be noticed that 1-obstruction has the highest effect compared to multiple obstructions in flow path.

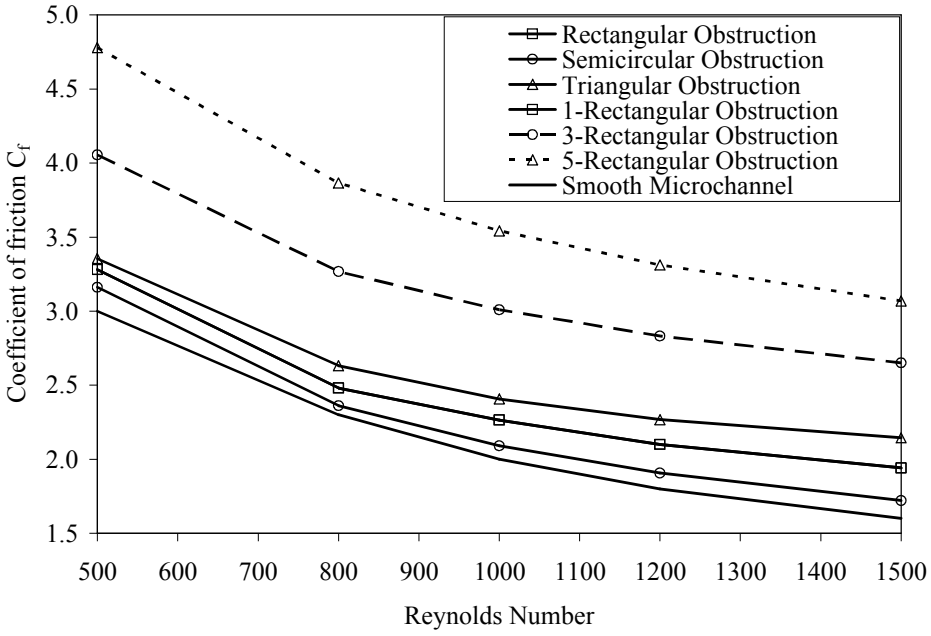

Figure 3.15 Coefficient of friction of microchannel for various protrusion shapes for water as working fluid.

Figure 3.15 presents the variation of friction coefficient (C_f) for the microchannels with Reynolds number varying from 500 to 1500 for the various shapes of the protrusions and also the repeated rectangular protrusions used in microchannels with the smooth Aluminum microchannel for water as the working fluid for the uniform heat flux applied all along the length of the microchannel. Here we see that as the Reynolds number increases, i.e. as the velocity of the working fluid increases we notice a decrease in C_f. We see that at lower Reynolds numbers the C_f of all the three different protrusion shapes is very close to each other. And as the velocity is increased we see C_f increases in value when compared to the smooth microchannel. At a Reynolds number of 1500 we observe that the microtube with triangular obstruction has the highest C_f among the different shapes of the protrusion. The highest C_f is seen with the five protrusion case.

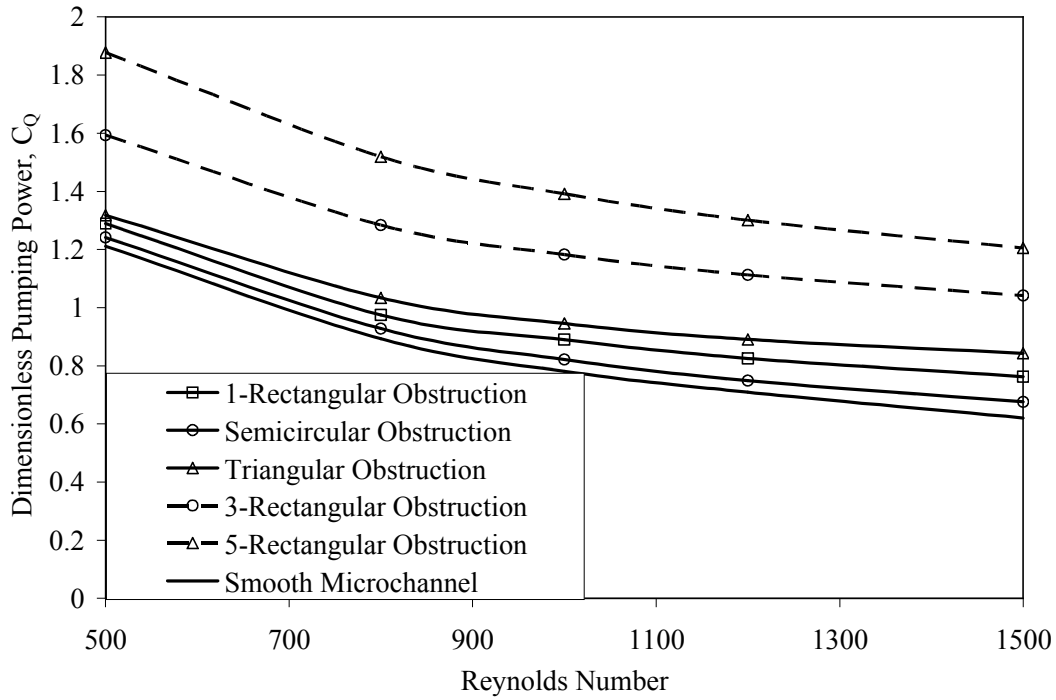

Figure 3.16 Pumping power for microchannel with various shapes of protrusion and various numbers of protrusions.

Figure 3.16 presents the variation of pumping power which is a product of difference of pressure and volume flow rate of fluid which was non-dimensionalized, for the microchannels with Reynolds number varying from 500 to 1500 for the various shapes of the restrictions and repeated restrictions used in smooth Aluminum microchannel for water as the working fluid for the uniform heat flux applied all along the length of the microtube. Here again, we see that as the Reynolds number increases, i.e. as the velocity of the working fluid increases we notice an increase in the value of pumping power. We see that at lower Reynolds number of 500 the pumping power of the configurations is the same. The pumping power required for the five protrusion case is the largest and the values for that of the three protrusions case is less than that of the five protrusions case and greater than that of the single protrusion cases. In the single protrusion case we see that with increase in Reynolds number the percentage increase in the pumping power required is quite dramatic. At Reynolds number of 500 we observe that the percentage increase in the Nusselt number with reference to the smooth microchannel is about 12% whereas the percentage pumping power required increases by 8%whencompared with the smooth microchannel, which is quite acceptable because there is considerable increase in heat transfer when compared to the increase in the required pumping power. For a Reynolds number of 1500 we see that that for a percentage increase of 9% in average Nusselt number we see a 22% increase in pumping power for the single rectangular restriction case. We observe that that even though there is a substantial augmentation in heat transfer but the pumping power required increases by a large value at higher Reynolds number values.

The variation of local Nusselt number with Reynolds number was plotted and compared with experimental results from Chen and Wang [13]. The value of local Nusselt number is plotted along the axial length of the block for a microchannel with air as the working fluid and Reynolds Number of 1300. We see there is a very good agreement between the experimental and Simulation data as see in figure 3.17.

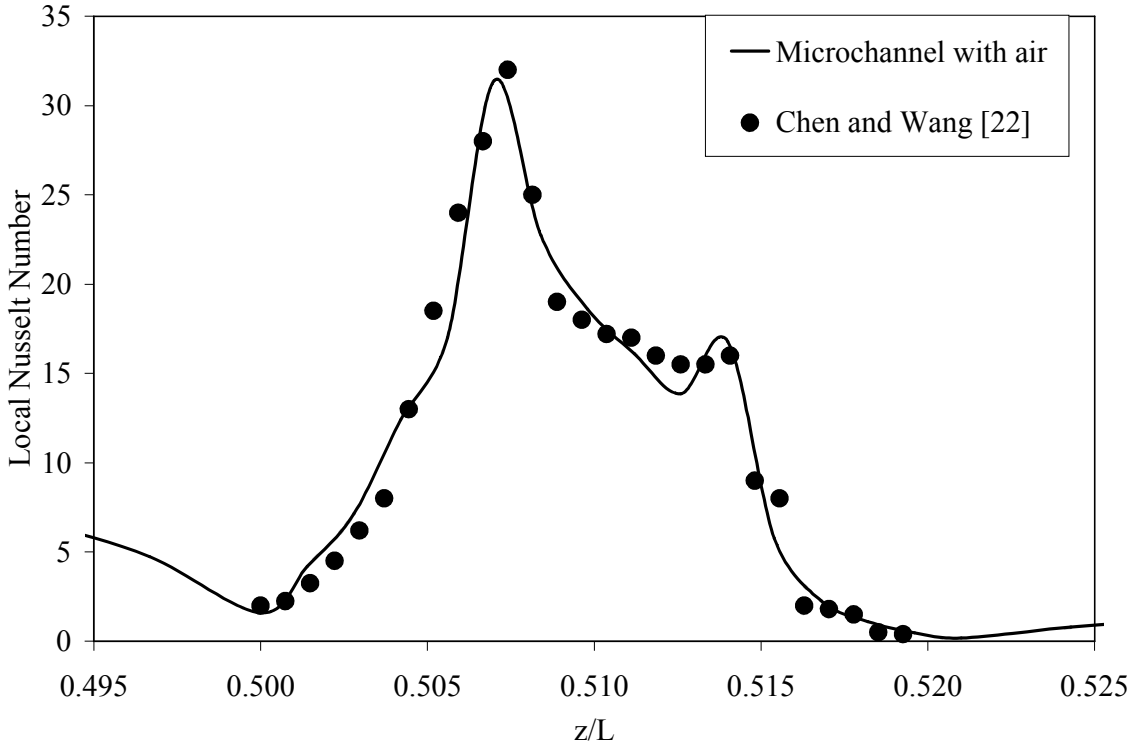

Figure 3.17 Comparison between numerical simulation and experimental results from Chen and Wang [13].

Chapter 4 Transient Heat Transfer in Trapezoidal Microchannels Under Time Varying Heat Source

4.1 Mathematical Model

The model in hand is a trapezoidal cross-sectional microchannel consisting of two different substrates gadolinium on top and silicon on bottom while the channel was manufactured into the bottom one with a lateral angle of 63^{o} from the horizontal. The gadolinium substrate on the top is joined to the silicon substrate and the primary working fluid selected was water. Figure 4.1 shows the schematic drawing of the model. Heat is generated in the gadolinium substrate and convected to the water while part of it is conducted to the silicon and then convected to water.

The applicable differential equations for the conservation of mass, momentum, and energy in the Cartesian coordinate system for the fluid can be written as [44],

$$\frac{\partial u}{\partial x}+\frac{\partial v}{\partial y}+\frac{\partial w}{\partial z}=0 \tag{4.1}$$

$$\frac{\partial u}{\partial t}+u\frac{\partial u}{\partial x}+v\frac{\partial u}{\partial y}+w\frac{\partial u}{\partial z}=-\frac{1}{\rho}\frac{\partial p}{\partial x}+\nu\left(\frac{\partial^2 u}{\partial x^2}+\frac{\partial^2 u}{\partial y^2}+\frac{\partial^2 u}{\partial z^2}\right) \tag{4.2}$$

$$\frac{\partial v}{\partial t}+u\frac{\partial v}{\partial x}+v\frac{\partial v}{\partial y}+w\frac{\partial v}{\partial z}=-\frac{1}{\rho}\frac{\partial p}{\partial x}+\nu\left(\frac{\partial^2 v}{\partial x^2}+\frac{\partial^2 v}{\partial y^2}+\frac{\partial^2 v}{\partial z^2}\right) \tag{4.3}$$

$$\frac{\partial w}{\partial t}+u\frac{\partial w}{\partial x}+v\frac{\partial w}{\partial y}+w\frac{\partial w}{\partial z}=-\frac{1}{\rho}\frac{\partial p}{\partial x}+\nu\left(\frac{\partial^2 w}{\partial x^2}+\frac{\partial^2 w}{\partial y^2}+\frac{\partial^2 w}{\partial z^2}\right) \tag{4.4}$$

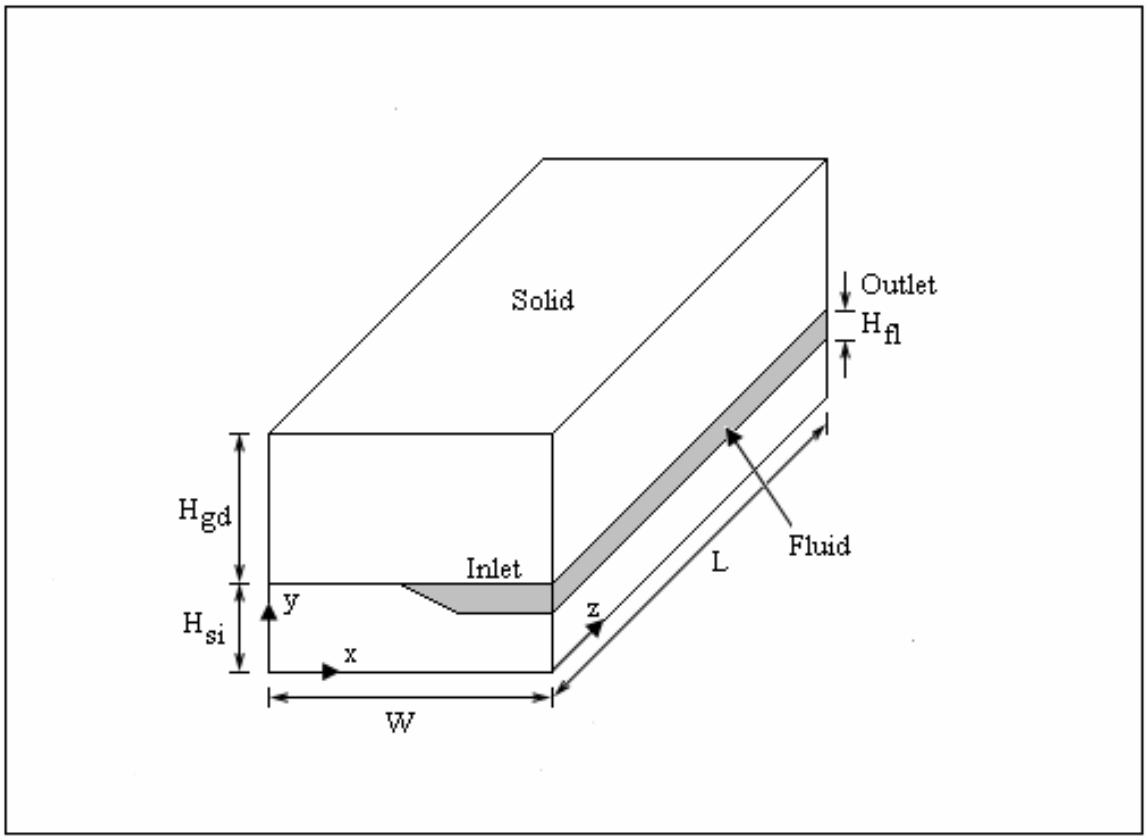

Figure 4.1 Schematic for microchannel heat exchanger model.

$$\frac{\partial T_f}{\partial t} + u\frac{\partial T_f}{\partial x} + v\frac{\partial T_f}{\partial y} + w\frac{\partial T_f}{\partial z} = \alpha\left(\frac{\partial^2 T_f}{\partial x^2} + \frac{\partial^2 T_f}{\partial y^2} + \frac{\partial^2 T_f}{\partial z^2}\right) \tag{4.5}$$

The energy conservation equation in the solid gadolinium substrate is [43]:

$$\frac{\partial^2 T_{gd}}{\partial x^2} + \frac{\partial^2 T_{gd}}{\partial y^2} + \frac{\partial^2 T_{gd}}{\partial z^2} + \frac{g_0}{k_{gd}} = \frac{1}{\alpha}\frac{\partial T_{gd}}{\partial t} \tag{4.6}$$

and for the solid silicon substrate is:

$$\frac{\partial^2 T_{si}}{\partial x^2} + \frac{\partial^2 T_{si}}{\partial y^2} + \frac{\partial^2 T_{si}}{\partial z^2} = \frac{1}{\alpha}\frac{\partial T_{si}}{\partial t} \tag{4.7}$$

Equations (1) – (7) are subject to following initial and boundary conditions:

At t = 0: $T_f = T_{gd} = T_{si} = T_{in}$ (4.8)

At z = 0, at fluid inlet: $u=0,\ v=0,\ w=w_{in},\ T=T_{in}$ (4.9)

At z = 0, on solid surface: $\frac{\partial T_{si}}{\partial z} = 0\,,\ \frac{\partial T_{gd}}{\partial z} = 0$ (4.10)

At z = L, at fluid outlet: $p=0$ (4.11)

At z = L, on solid surface: $\frac{\partial T_{si}}{\partial z} = 0\,,\ \frac{\partial T_{gd}}{\partial z} = 0$ (4.12)

At x = 0, $0 < y < (H_{si}-H_{fl})$, $0 < z < L$: $\frac{\partial T_{si}}{\partial z} = 0$ (4.13)

At x = 0, $(H_{si}-H_{fl}) < y < H_{si}$, $0 < z < L$: $u=0,\ \frac{\partial v}{\partial x} = 0\,,\ \frac{\partial w}{\partial x} = 0\,,\ \frac{\partial T_f}{\partial x} = 0$ (4.14)

At x = 0, $H_{si} < y < (H_{si}+H_{gd})$, $0 < z < L$: $\frac{\partial T_{gd}}{\partial x} = 0$ (4.15)

At x = B, $0 < y < H_{si}$, $0 < z < L$: $\frac{\partial T_{si}}{\partial x} = 0$ (4.16)

At x = B, $H_{si} < y < (H_{si}+H_{gd})$, $0 < z < L$: $\frac{\partial T_{gd}}{\partial x} = 0$ (4.17)

At y = 0, $0 < x < B$, $0 < z < L$: $\frac{\partial T_{si}}{\partial y} = 0$ (4.18)

At $y = (H_{si}-H_{fl})$, $B-B_s < x < B$, $0 < z < L$: $u=0$, $v=0$, $w=0$, $T_f = T_{si}$, and

$$k_f \frac{\partial T_f}{\partial y} = k_{si} \frac{\partial T_{si}}{\partial y} \quad (4.19)$$

At $y = H_{si}$, $0 < x < B-B_c$, $0 < z < L$: $u=0$, $v=0$, $w=0$, $T_f = T_{gd}$, and

$$k_f \frac{\partial T_f}{\partial y} = k_{gd} \frac{\partial T_{gd}}{\partial y} \quad (4.20)$$

At $y = H_{si}$, $B-B_c < x < B$, $0 < z < L$: $$k_{si} \frac{\partial T_{si}}{\partial y} = k_{gd} \frac{\partial T_{gd}}{\partial y} \quad (4.21)$$

At $y = (H_{si}+H_{gd})$, $0 < x < B$, $0 < z < L$: $\frac{\partial T_{gd}}{\partial y} = 0$ (4.22)

The inclined fluid-silicon surface, 0<z<L, u=0, v=0, w=0, $T_f = T_{si}$, and

$$k_f \frac{\partial T_f}{\partial n} = k_{si} \frac{\partial T_{si}}{\partial n} \tag{4.23}$$

4.2 Numerical Simulation and Parametric Study

The governing equations along with the initial and boundary conditions were solved using the Galerkin finite element method. The Newton-Raphson algorithm was used to solve the nonlinear system of discretized equations. An iterative procedure was used to arrive at the solution for the velocity and temperature fields. The solution was considered converged when the field values did not change from one iteration to the next, and the residuals for each variable became negligible.

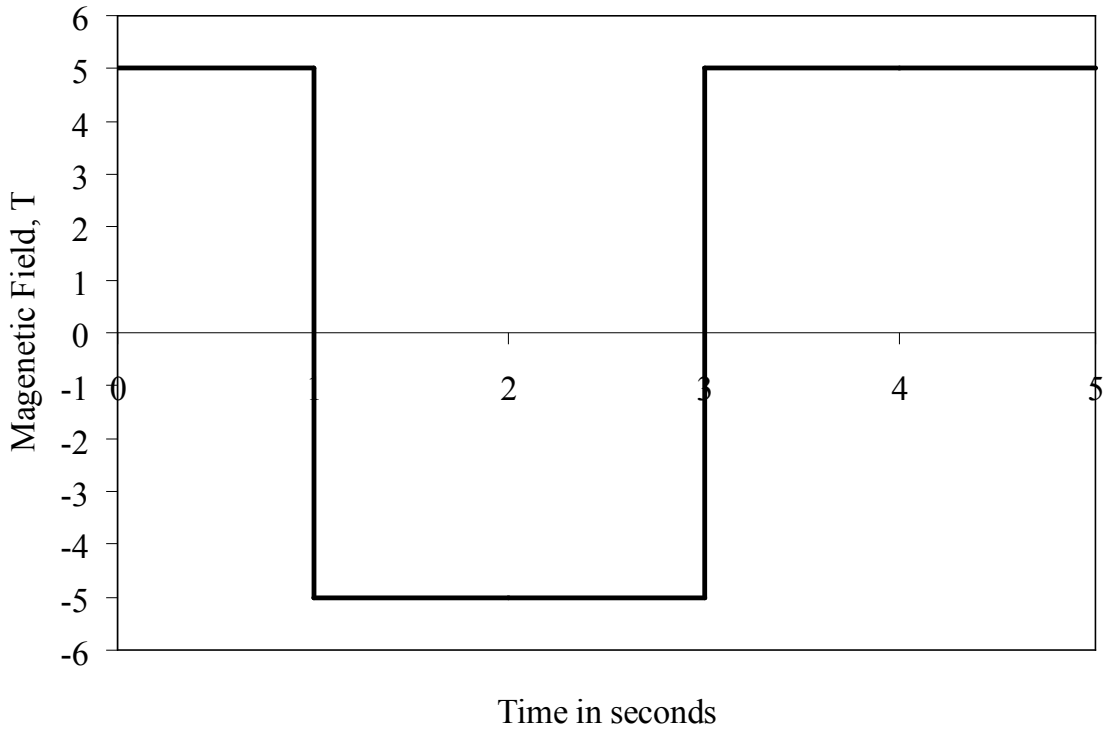

Figure 4.2 Local variation of magnetic field with time.

For the numerical computations, the Length (L) and the half width (W) of the model were set to a constant value, 1.0 cm and 0.3 cm respectively. The height of the silicon substrate (H_{si}) and the inlet temperature were also set to a constant value, 0.1 cm and 20 ^{o}C respectively. To represent the heat generation and cooling process numerically, the magnetic field value was fluctuated between the values of +5 and -5 T, figure 5.2. Time period of 2 seconds was used. The first period was chosen to be one half of the selected time length since it started from the initial condition. We had one complete cooling and one complete heating cycle after the initial half heating cycle because the subsequent heating and cooling cycles exhibited similar trend to the first cooling and heating cycles.

The parameters to be changed were selected to be: Reynolds number, magnetic field, height of fluid microchannel, width of fluid microchannel, and working fluid. Initially these parameters were selected as follows: Re = 2000, G = 5 Tesla, H_{fl} = 0.03 cm, H_{gd} = 0.3 cm, and water as the working fluid. One parameter was changed at a time while all other parameters kept constant to study the effect of each parameter separately. Reynolds number was changed to 1500 and 1000, G was changed to 2 and 10 Tesla, H_{fl} was changed to 0.02 cm, W_{fl} was changed to 0.13cm, and the working fluid was changed from water to R-134a.

4.3 Result and Discussion

Figure 4.3 shows a grid independence study carried out in the cross-sectional area of the channel to determine the optimum grid size and to insure accurate results. The number of intervals in the axial direction kept constant because it does not affect the

results significantly. The results obtained by using (nx = 16, ny = 16, nz = 42) that had an average error of 0.0034% in the silicon side and a maximum error of 0.01% in the interface temperature compared to (nx = 20, ny = 12, nz = 42). The heat flow rate also shows a small error comparing the above two grid systems. Figure 4.3 show that the grid size (nx = 16, ny = 16, nz = 42) selected was sufficient enough to reach optimum results.

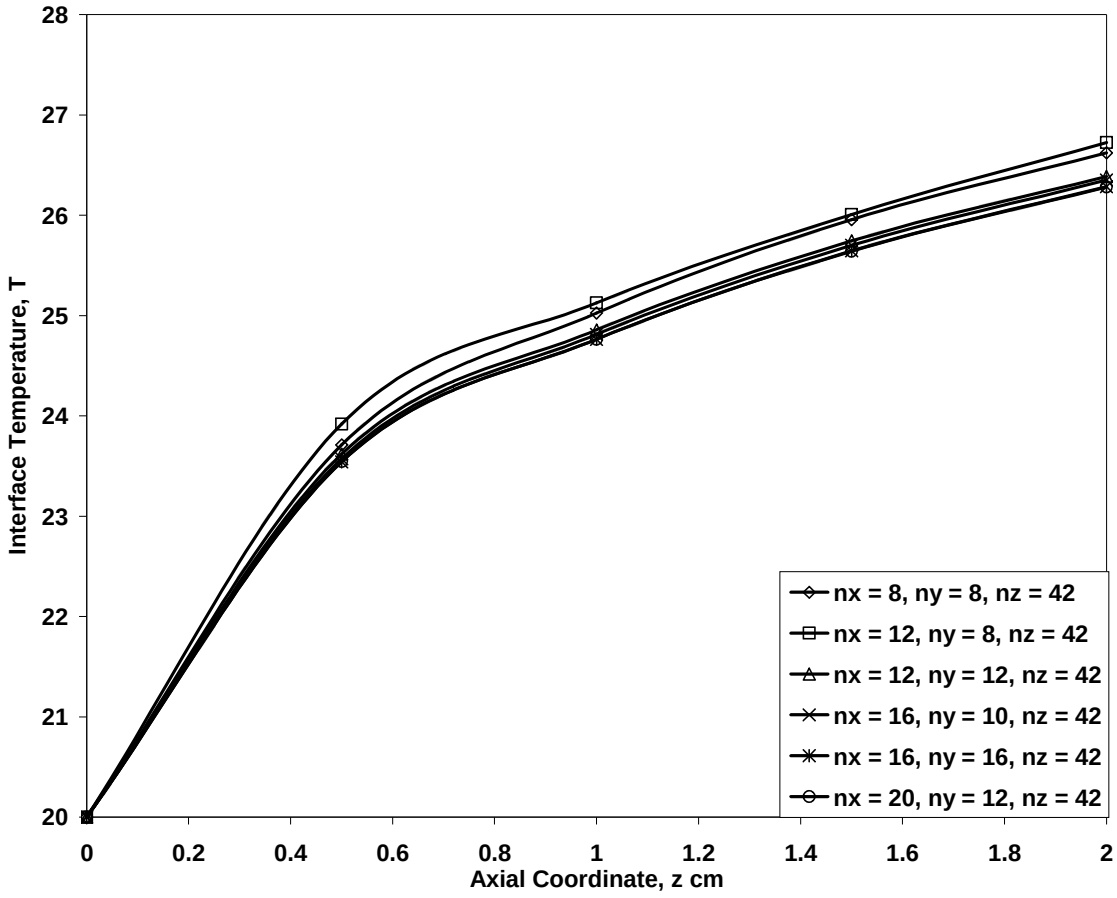

Figure 4.3 Peripheral average interface temperature along the axial direction at the fluid-silicon interface (Re = 2000, G = 5 T, H_{fl} = 0.03 cm).

The local interface temperature, heat flow rate, heat transfer coefficient and Nusselt number were calculated from the resulted velocity and temperature distribution. The heat generation occurred in the 1st and 3rd periods while the cooling process occurred in the 2nd period.

Figures 4.4 and 4.5 shows the local Nusselt number along different channel edges. Curves for different axial locations were plotted. Figure 4.4 shows the local Nusselt along the fluid-gadolinium interface at different axial locations at the end of the first time period. It shows that Nusselt number is higher closer to the center of the trapezoidal microchannel. This is because the fluid volume is lesser at the edges of the trapezoidal microchannel which results in lesser resistance in heat transfer. This lesser resistance gives smaller temperature gradient in the solid region resulting in smaller heat flow rate. The heat flow rate increases along the edge towards the center of the channel. This causes the heat transfer coefficient, and thus Nusselt number, to increase. Along the axial direction, the temperature gradient decreases causing the heat flow rate to decrease. The interface-bulk temperature difference increases along the axial direction. Both cause the Nusselt number to decrease along the axial direction.

Figure 4.5 shows the local Nusselt along the fluid-silicon interface at different axial locations at the end of the first time period. The silicon edge is tapered at closer to the side ends of the channel. At the tapered edge, there is small fluid volume where the heat flow rate almost transfers without any resistance. As a result, the temperature gradient is smaller and causes smaller heat flow rate values, and thus, smaller Nusselt number. The heat flows from the gadolinium to the silicon by conduction and then to the fluid by convection. At the very far tip of the tapered edge, the heat flow finds away to travel through the fluid and to the silicon overcoming the small fluid resistance. Further away from the tip of the tapered edge, the heat flow from the silicon takes control giving positive results. The heat flow rate increases quickly along the tapered edge reaching reasonable values resulting in adequate Nusselt number values.

Along the horizontal edge, the temperature gradient and the heat flow rate decrease. This is because part of the heat flow rate that travel through the silicon transfers by convection to the fluid before it reaches the center of the channel. This eventually causes Nusselt number to decrease along the horizontal side of the silicon edge. Similarly to the gadolinium edge, the temperature gradient decreases along the axial direction. This causes the heat flow rate to decrease along the axial direction. The interface-bulk temperature difference increases along the axial direction. Both cause the Nusselt number to decrease along the axial direction.

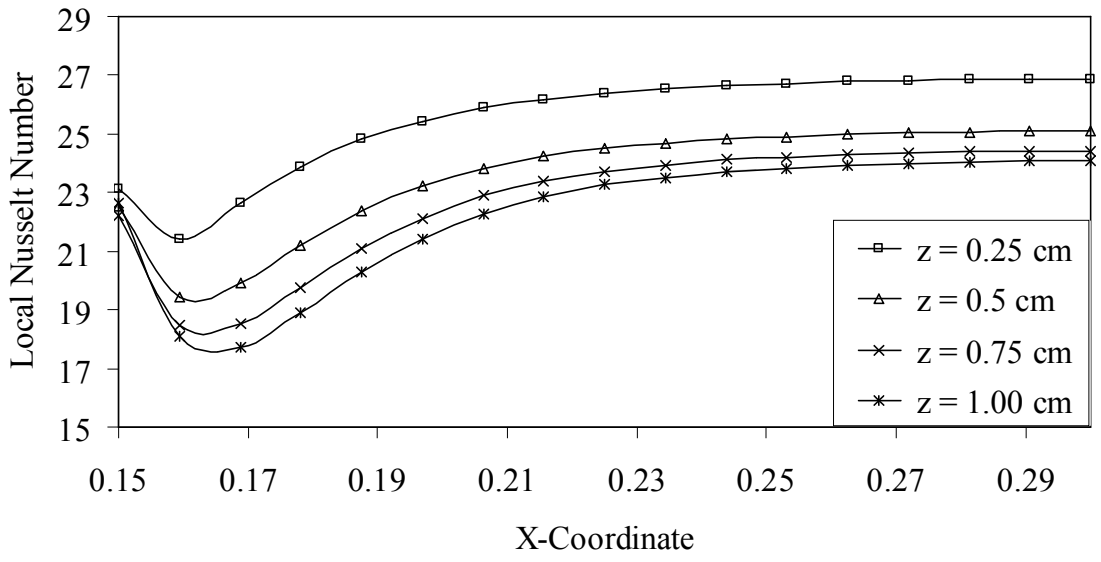

Figure 4.4 Local Nusselt along the fluid-gadolinium interface at different axial locations after 1 second (Re = 2000, G = 5 T, H_{fl} = 0.03 cm).

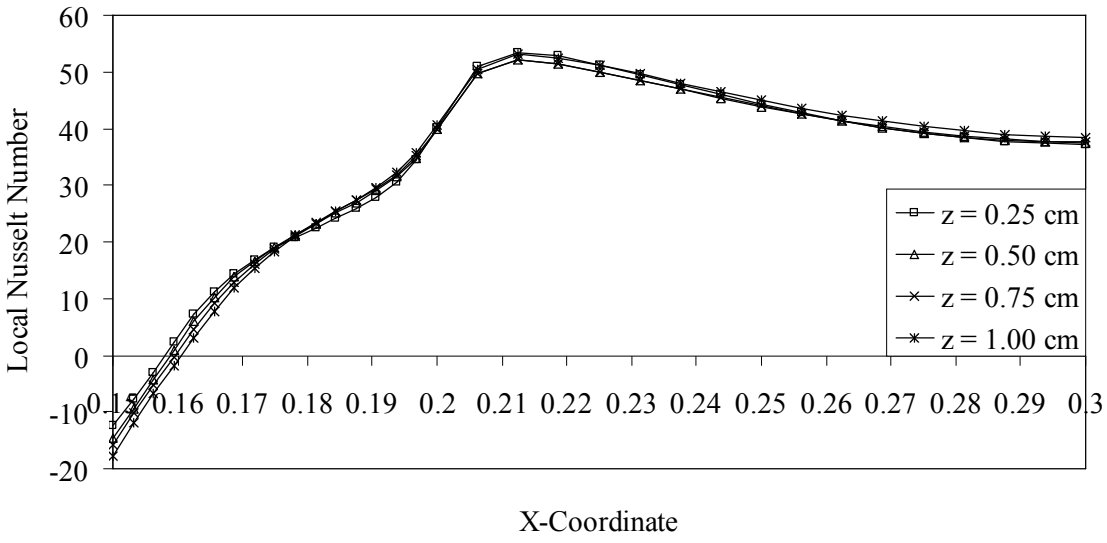

Figure 4.5 Local Nusselt along the fluid-silicon interface at different axial locations after 1 second (Re = 2000, G = 5 T, H_{fl} = 0.03 cm).

Figure 4.6 shows the bulk temperature over the length of the tube for different time periods. As heat is generated the bulk temperature increases and it decreases when cooling process takes over. The bulk temperature increases in the first half heating period and then the cooling stage starts and the temperature starts falling below the initial fluid temperature. The lowest bulk temperature is attained at the end of the cooling period and again the bulk temperature starts to increase and reaches the highest value at the end of the second heating phase.

Figure 4.7 shows the average interface temperature variation at different locations for different time at the solid-fluid interface. It follows the same trend as seen in the case of bulk temperature, but the maximum value of the temperature attained during the heating phases is higher and the lowest value attained during the cooling phases is lower than that of the bulk temperature. This is because the heating and cooling occurs in the solid and the heat is transferred to the fluid.

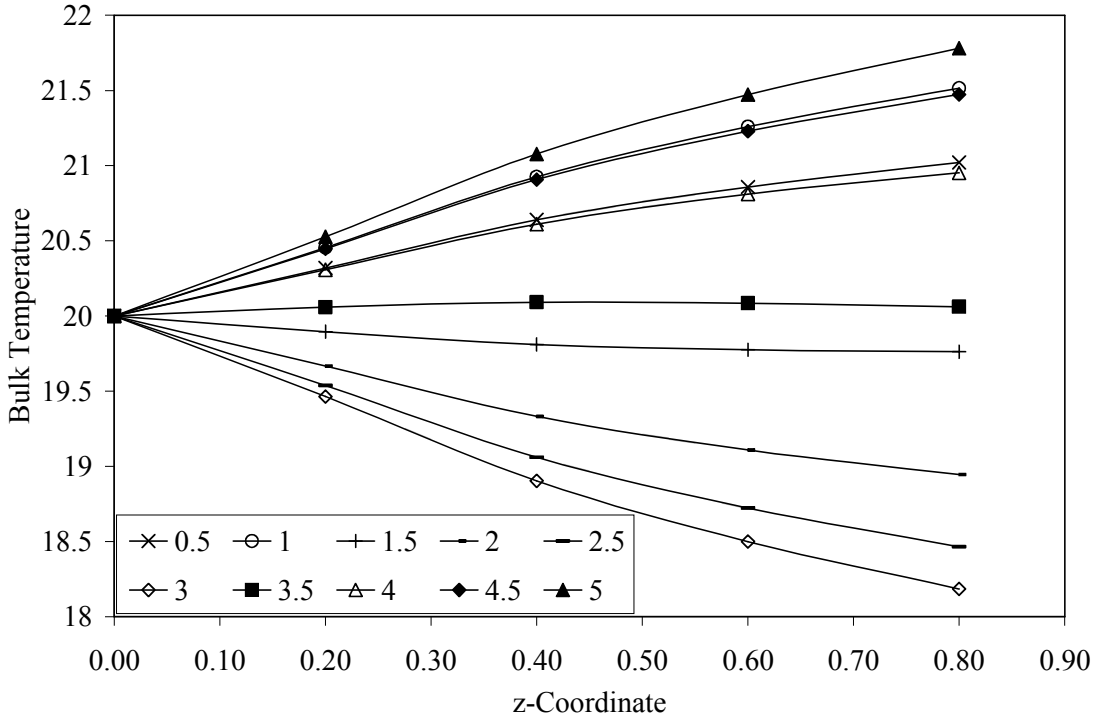

Figure 4.6 Bulk temperature at different axial locations for different time periods (Re = 2000, G = 5 T, H_{fl} = 0.03 cm).

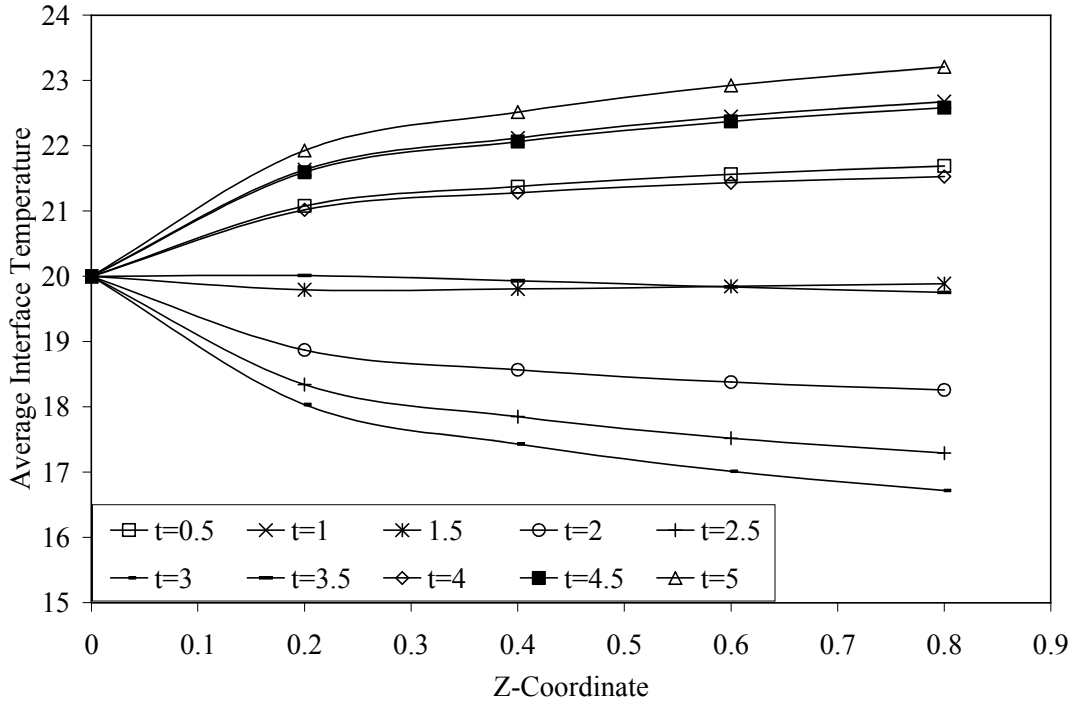

Figure 4.7 Peripheral average interface temperature at different axial locations for different time periods (Re = 2000, G = 5 T, H_{fl} = 0.03 cm).

Figure 4.8 shows the average heat flux along the solid-fluid interface. The average heat flux is a function of the difference between the interface temperature and the fluid temperature adjacent to the wall on both the Gadolinium side and the Silicon side. During the heating stage we have heat flow from the solid to the fluid as the temperature in the solid is greater than that of the fluid temperature; hence we have a positive value of the heat flux during the heating phase. In the cooling phase the temperature of the solid becomes lesser than that of the fluid and hence we have heat flow from the fluid to the solid, thus the negative heat flux values during the cooling phase.

Figure 4.9 shows the average Nusselt number at different axial locations at different time periods for the total interface including both sides of the channel, gadolinium and silicon sides. The Nusselt number behavior is shown to be more or less the same for each time period regardless of the process. But at time t=1.5 s there is a switch from heating to cooling phase causing the interface and bulk temperature to switch from heating to cooling process. Thus we see there is a very low average Nusselt number value. Again when the cooling period switches to the heating period we see a dip in the Nusselt number value. At a certain point of the switching process Nusselt number will be infinite, that is when the interface and bulk temperature are equal. The switch between interface and bulk temperatures seems to occur early in the second period causing lower Nusselt number at time 1.5 s. Nusselt number variation seems to be steady further away from the inlet because of the lower heat flow rate that results from lower interface-bulk temperature.

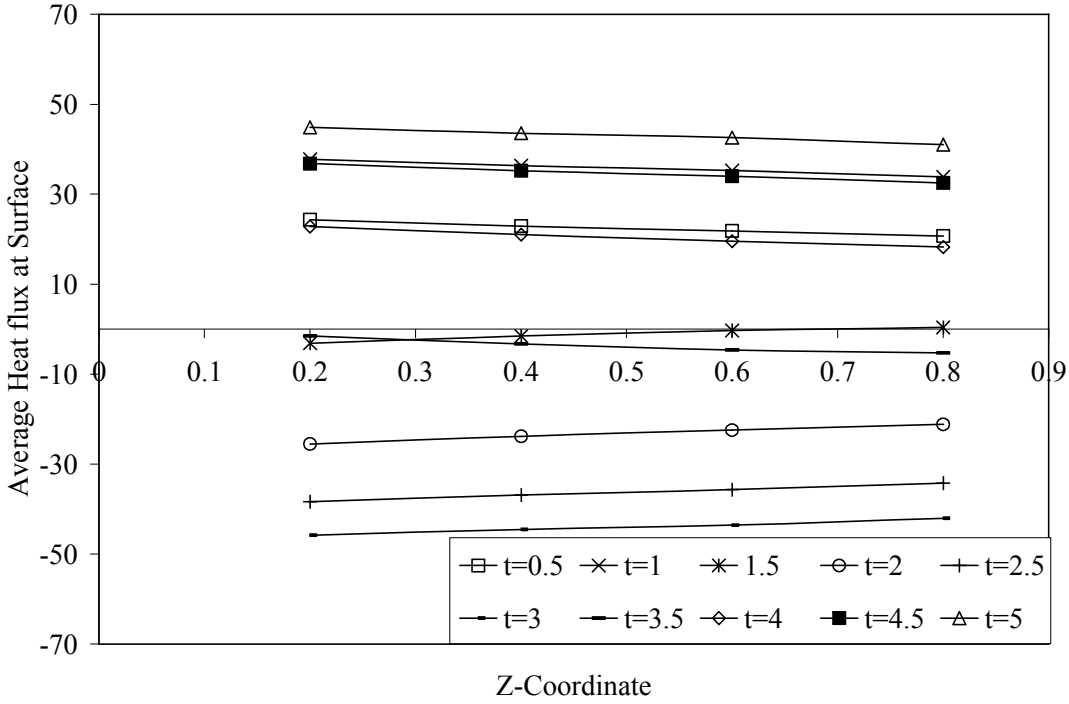

Figure 4.8 Average heat flux at surface at different axial locations for different time periods (Re = 2000, G = 5 T, H_{fl} = 0.03 cm).

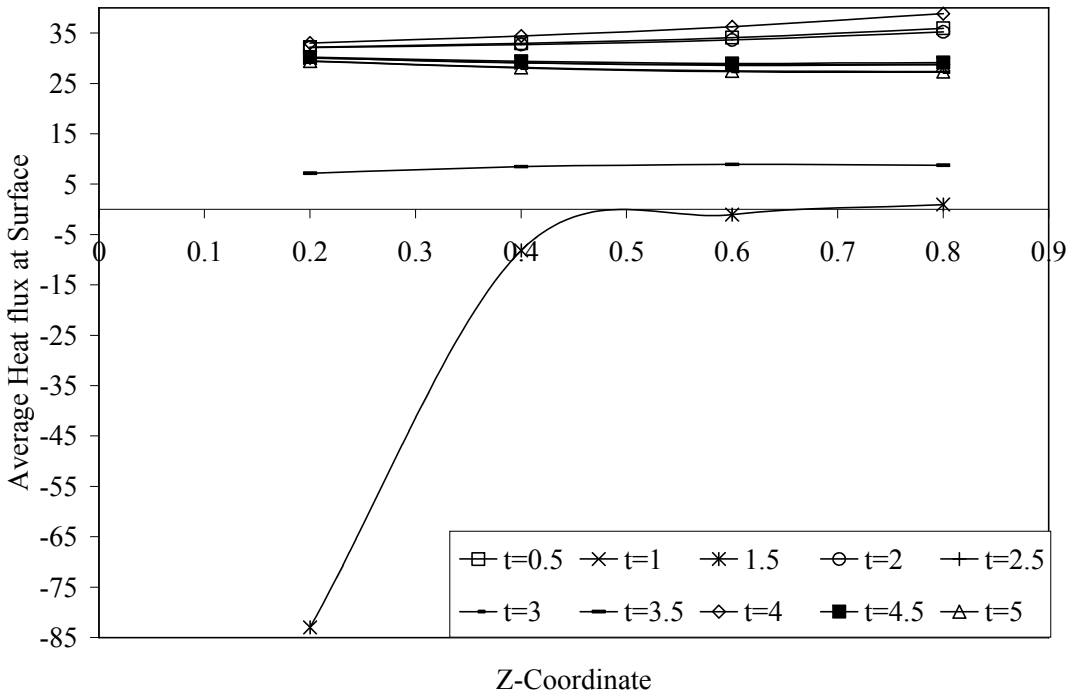

Figure 4.9 Peripheral average Nusselt number at different axial locations for different time periods (Re = 2000, G = 5 T, H_{fl} = 0.03 cm).

4.3.1 Reynolds number

The above results were for the base case which had Reynolds number value of 2000. The first parameter that was changed was Reynolds number to 1500 and also to1000. Figure 4.10 shows the bulk temperature over the length of the tube at different time periods for Re = 1500. Lower Reynolds number, or lower fluid velocity, slows down the heating and cooling process and thus results in higher bulk temperature because of the higher and lower value of average interface temperature as seen in the figure 4.11 as compared to the base case. It also results in a slightly higher average value of heat flux as seen in figure 4.12 in comparison with figure 4.8. Nusselt number behavior in figure 4.13 is explained in the same fashion as in the previous case. The value of Nusselt number is higher than the original case because of the higher absolute values of the heat flow rate resulted from lower fluid velocity.

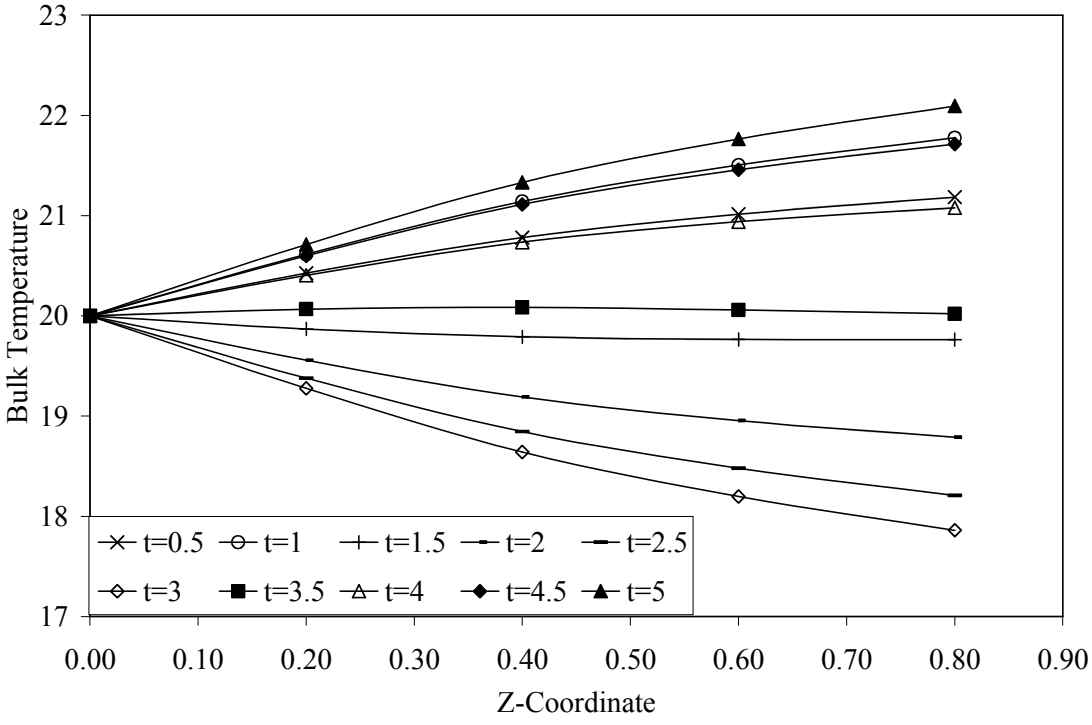

Figure 4.10 Bulk temperature at different axial locations for different time periods for Re = 1500 (G = 5 T, H_{fl} = 0.03 cm).

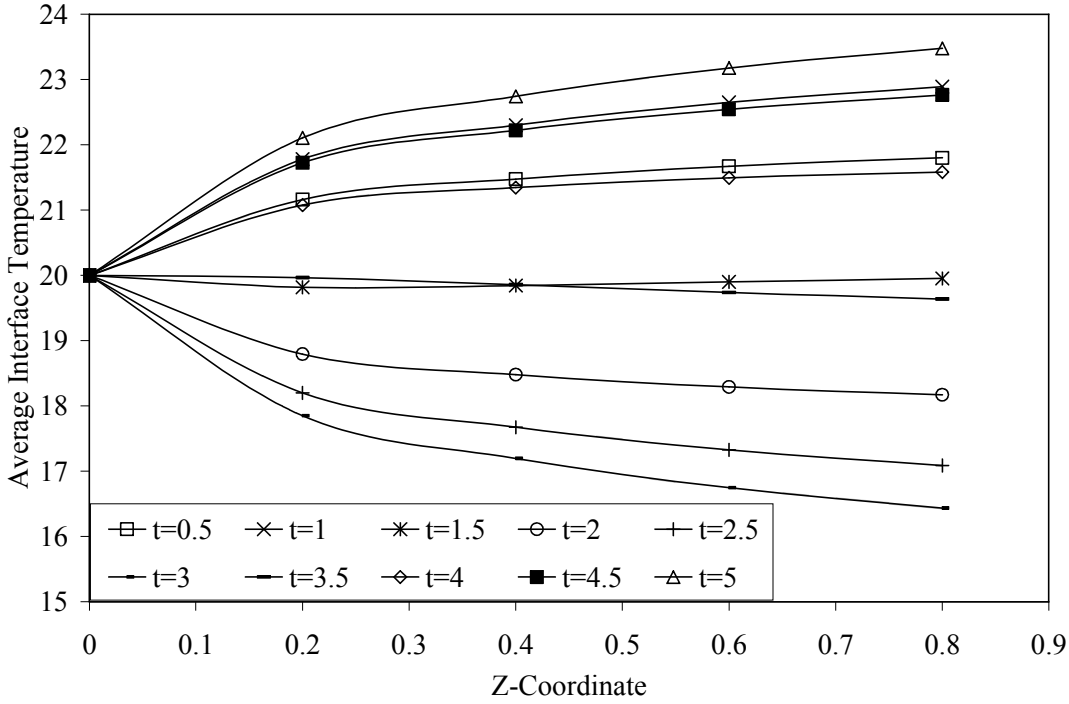

Figure 4.11 Peripheral average interface temperature at different axial locations for different time periods for Re = 1500 (G = 5 T, H_{fl} = 0.03 cm).

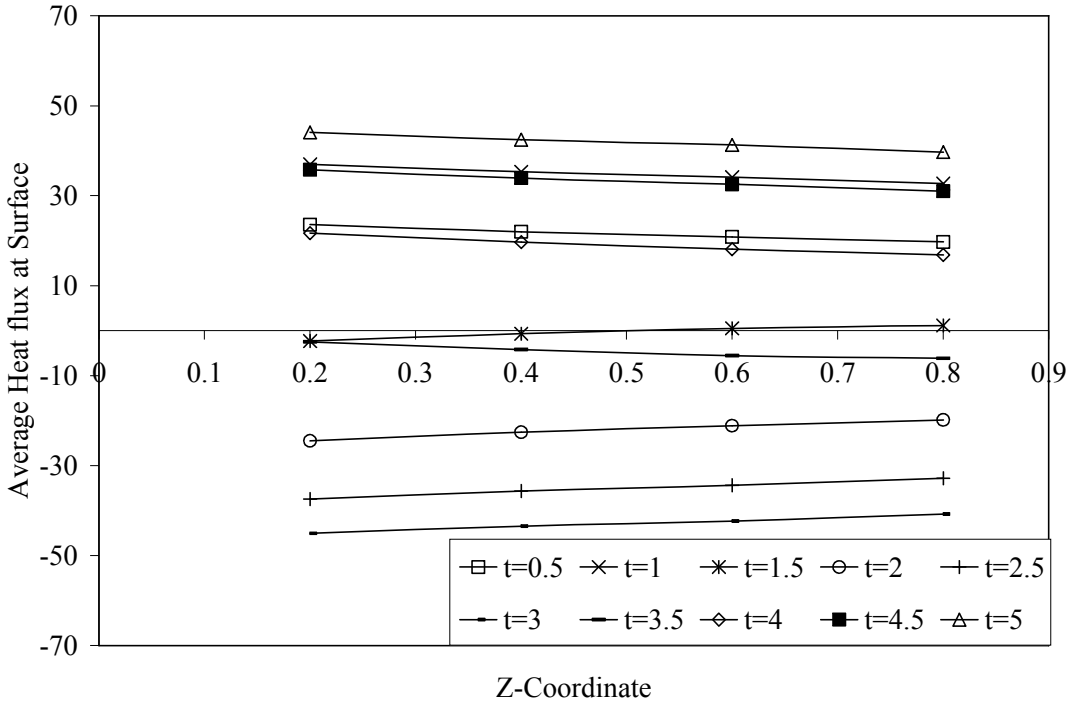

Figure 4.12 Average heat flux at surface at different axial locations for different time periods for Re = 1500 (G = 5 T, H_{fl} = 0.03 cm).

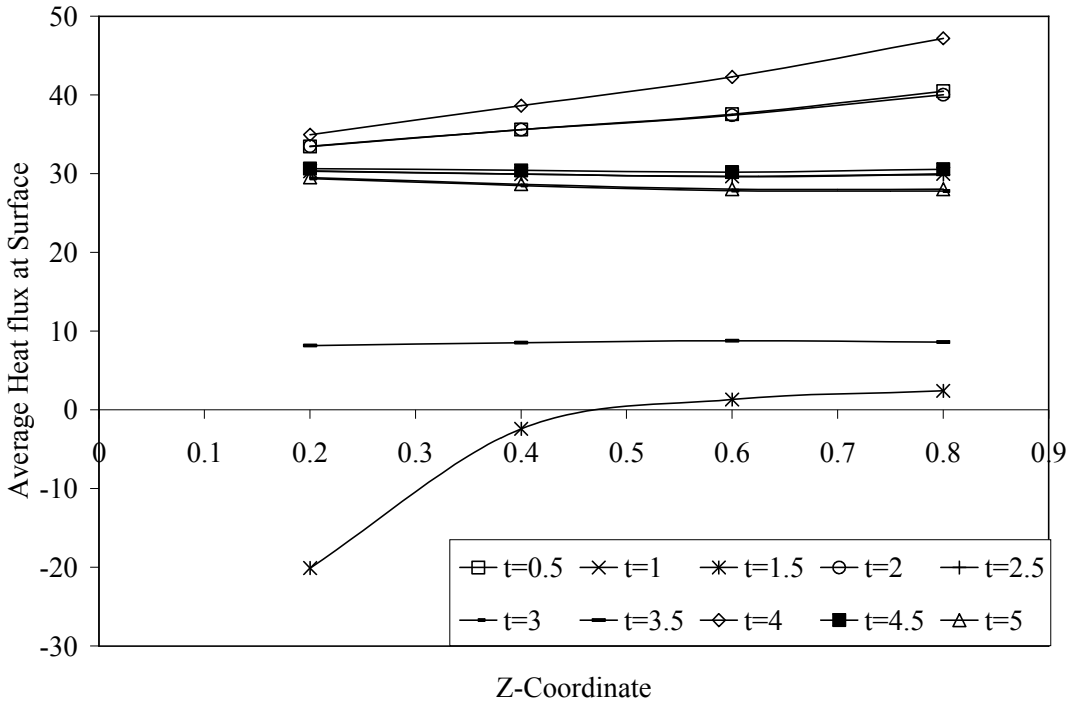

Figure 4.13 Peripheral average Nusselt number at different axial locations for different time periods for Re = 1500 (G = 5 T, H_{fl} = 0.03 cm).

Now we again vary the Reynolds number to 1000 from 1500 by varying the fluid inlet velocity. Figures 4.14 and 4.15 show the variation of bulk temperature and average interface temperature for different time periods at different location along the tube for Re = 1000. We again observe similar behavior as seen in the previous case i.e. for Re = 1500, but the values of bulk and average interface temperature is higher than that seen in the previous case (Re = 1500) and also the same trend is followed by the average heat flux as seen in figure 4.16 for 5 seconds of heating and subsequent cooling stages. Figure 4.17 shows the variation of average Nusselt number at various locations along the length of the microchannel for different time periods. the trend followed is similar but for the fact the jump in the value of average Nusselt number at the middle of each heating (t=0.5 sec) time (t=4 sec) and cooling process (t= 2 sec) is significantly higher which can be explained by the fact that the fluid velocity is much lower than in the previous cases.

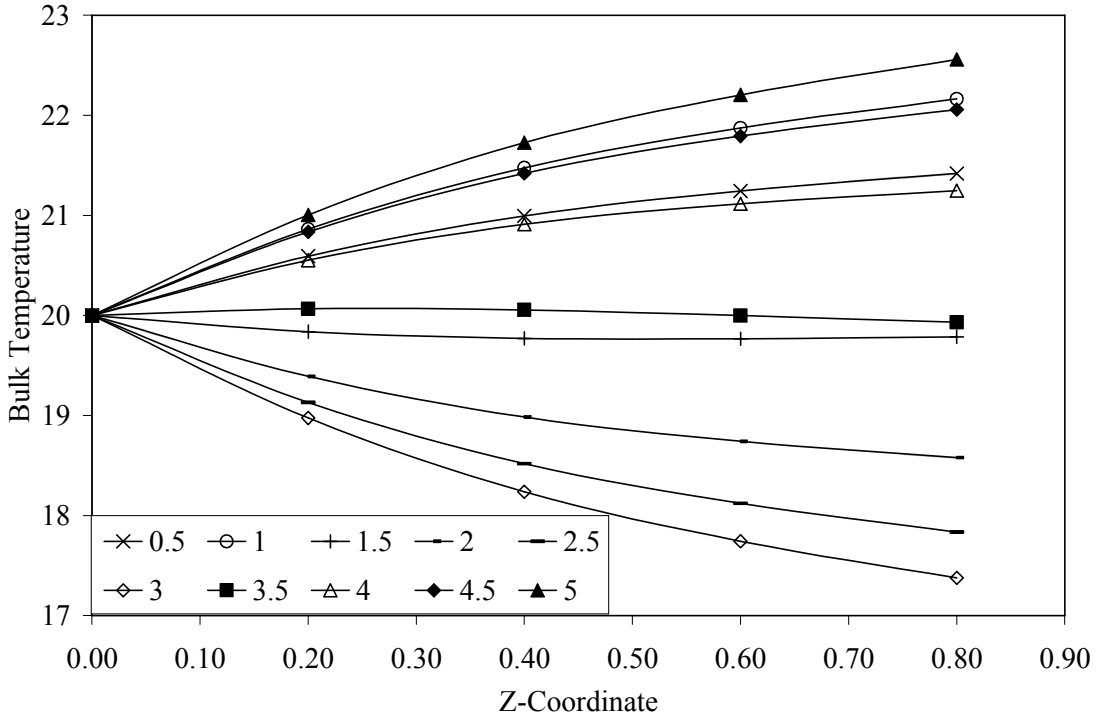

Figure 4.14 Bulk temperature at different axial locations for different time periods for Re = 1000 (G = 5 T, H_{fl} = 0.03 cm).

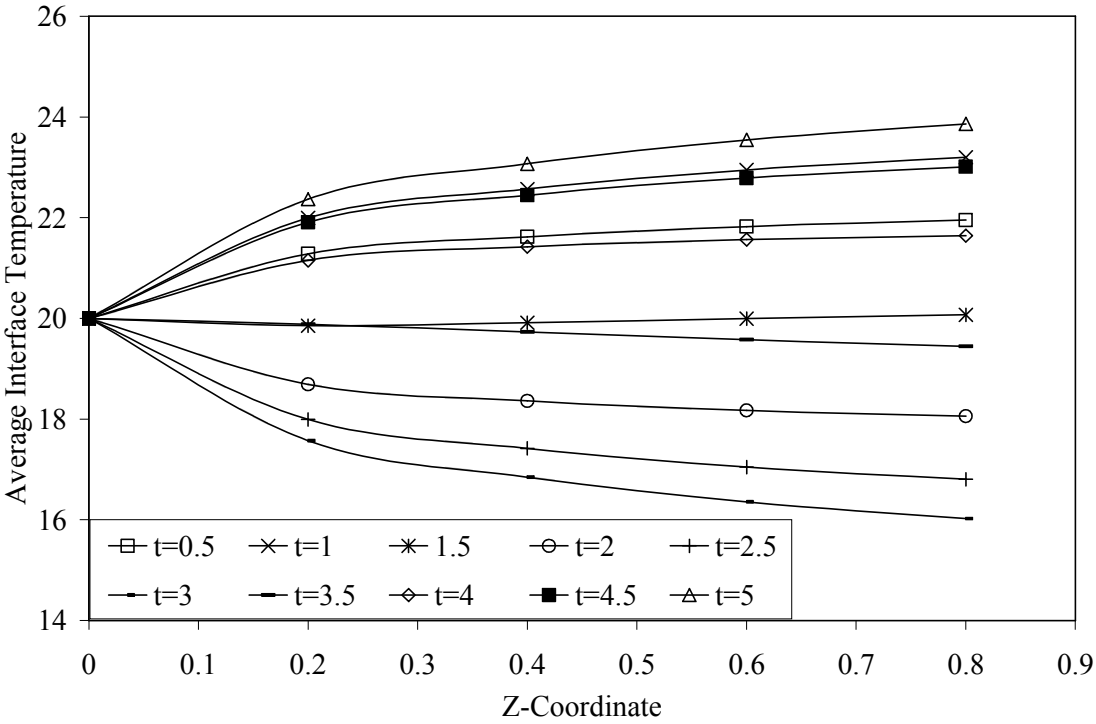

Figure 4.15 Peripheral average interface temperature at different axial locations for different time periods for Re = 1000 (G = 5 T, H_{fl} = 0.03 cm).

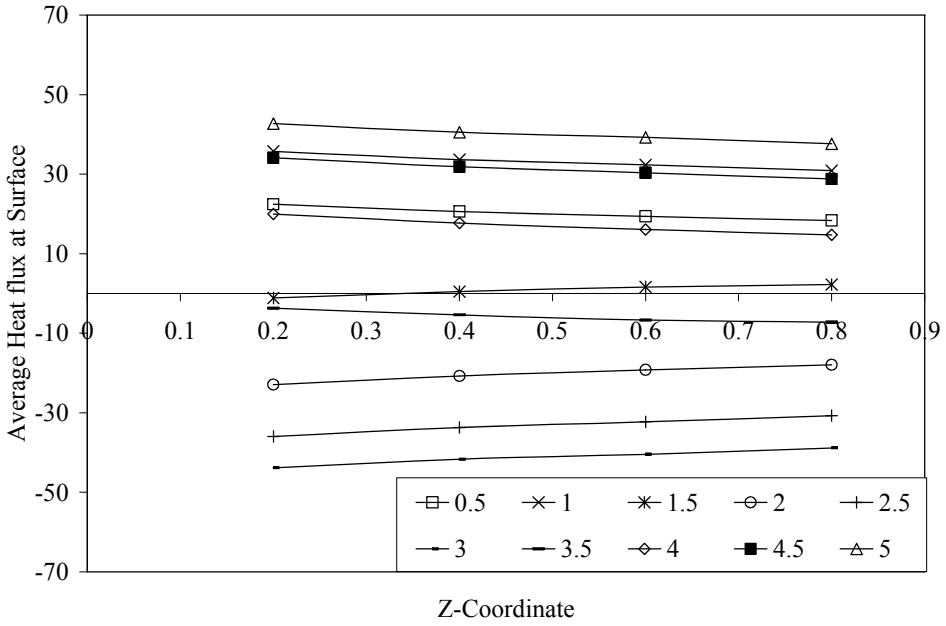

Figure 4.16 Average heat flux at surface at different axial locations for different time periods for Re = 1000 (G = 5 T, H_{fl} = 0.03 cm).

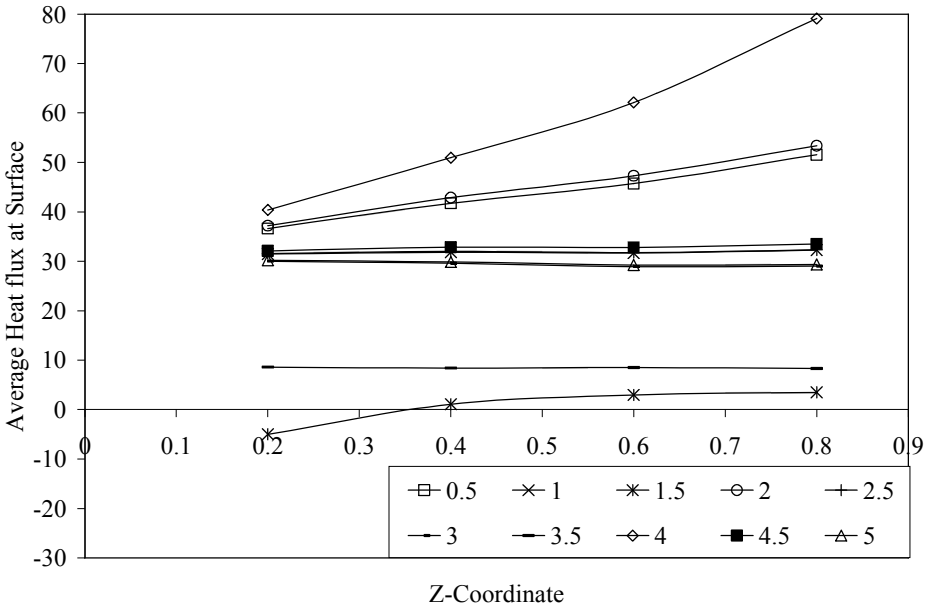

Figure 4.17 Peripheral average Nusselt number at different axial locations for different time periods for Re = 1000 (G = 5 T, H_{fl} = 0.03 cm).

4.3.2 Magnetic field

For the above results we varied the Reynolds number by varying the inlet velocity of the working fluid. Now we keep the inlet velocity constant, therefore keeping Re =

2000 and varying the magnetic field which was originally alternating between +5 T to -5 T is changed to be alternating between +10 T to -10 T and also from +2 T to -2T. Figures 4.18 and 4.19 show the bulk temperature and average interface temperature at different axial locations for different time periods. The bulk and interface temperatures reach higher values when heating and lower values when cooling than those of the base case. This is because of the larger magnetic field applied during heating and cooling. Figure 4.20 shows the average heat flux at different axial locations for different times. The heat flow rate is higher when heating and lower when cooling compared to the previous case. This is because of the higher heat source and sink caused by higher magnetic field in both processes. Figure 4.21 shows the average Nusselt number at different axial locations for different times at the fluid-solid interface with magnetic field alternates between +10 and -10. Our experience from previous work tells us that the change in the magnetic field does not affect the Nusselt number. The figure shows very close results to those of the original base case.

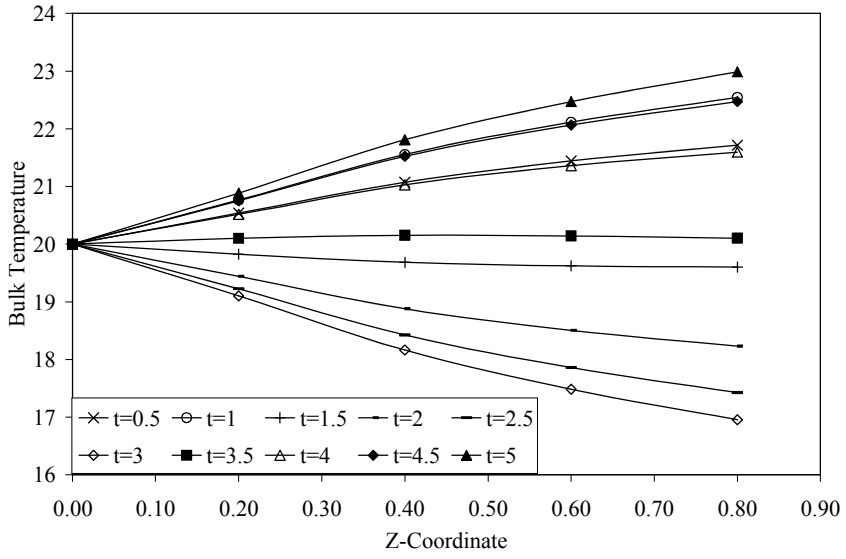

Figure 4.18 Bulk temperature at different axial locations for different time periods for G = 10 T (Re = 2000, H_{fl} = 0.03 cm).

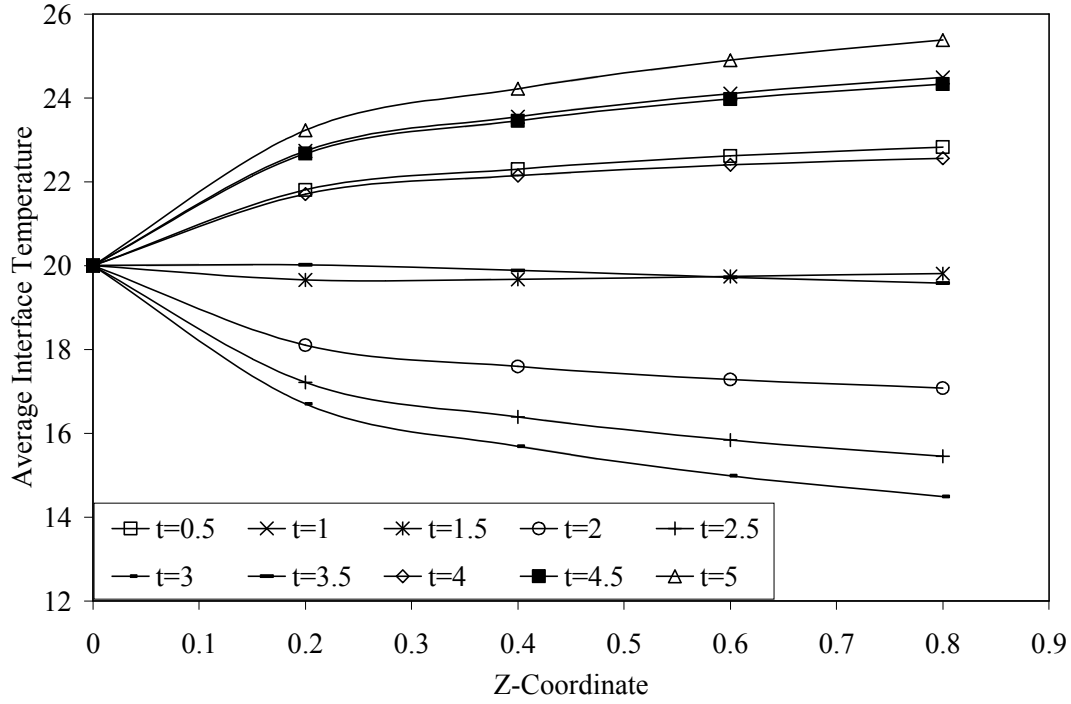

Figure 4.19 Peripheral average interface temperature at different axial locations for different time periods for G = 10 T (Re = 2000, H_{fl} = 0.03 cm).

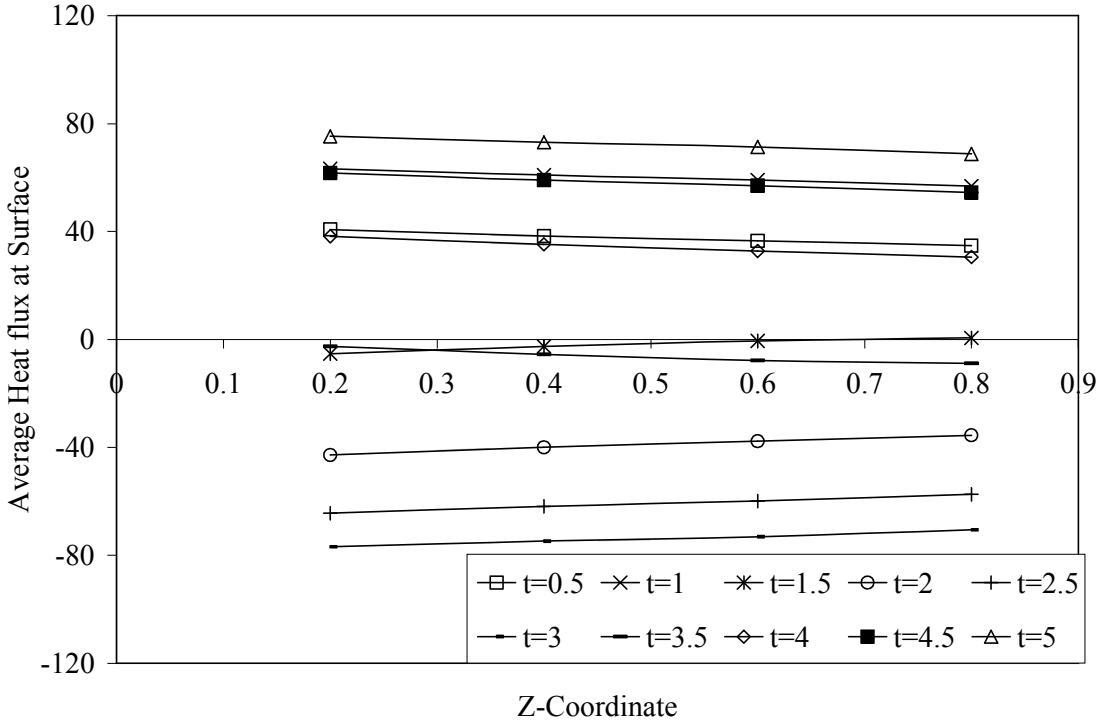

Figure 4.20 Average heat flux at surface at different axial locations for different time periods for G = 10 T (Re = 2000, H_{fl} = 0.03 cm).

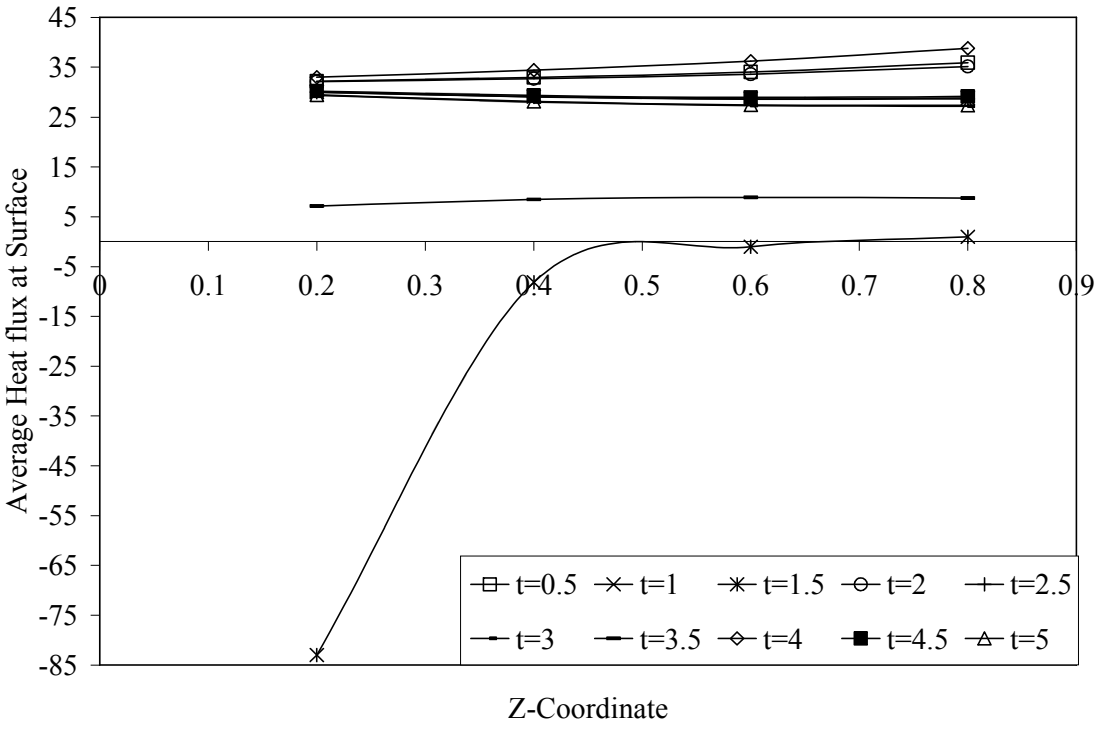

Figure 4.21 Peripheral average Nusselt number at different axial locations for different time periods for G = 10 T (Re = 2000, H_{fl} = 0.03 cm).

Now we change the magnetic field to be alternating from +2 T to -2 T, and keep the other parameters constant from the base case. Figures 4.22 and 4.23 show the bulk temperature and the average interface temperature at different axial locations for different times with magnetic field alternating between +2 T and -2 T. The bulk and the interface temperatures are lower when heating and higher when cooling than that of the previous case and also the base case. This is because of the smaller magnetic field applied during heating and cooling. Figure 4.24 shows the average heat flux at different axial locations for different times. The heat flux is again lower when heating and higher when cooling compared to the base and also the previous case similar to the bulk and interface temperature variation. This is because of the lower heat source and sink caused by lower magnetic field at both processes.

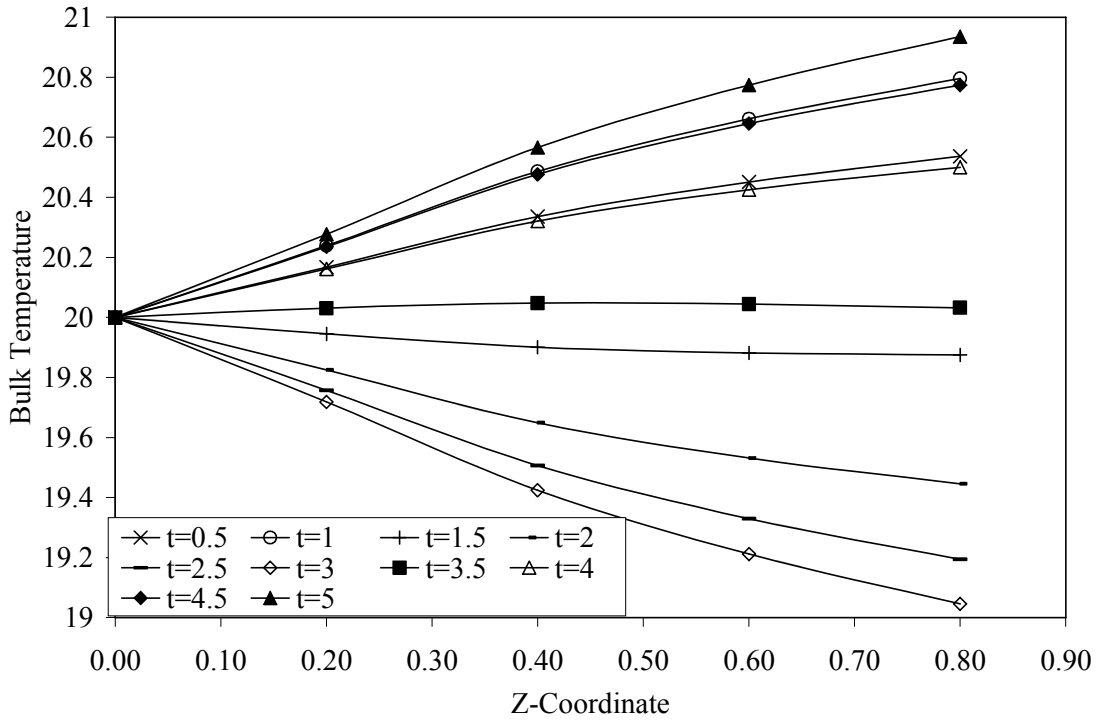

Figure 4.22 Bulk temperature at different axial locations for different time periods for G = 2 T (Re = 2000, H_{fl} = 0.03 cm).

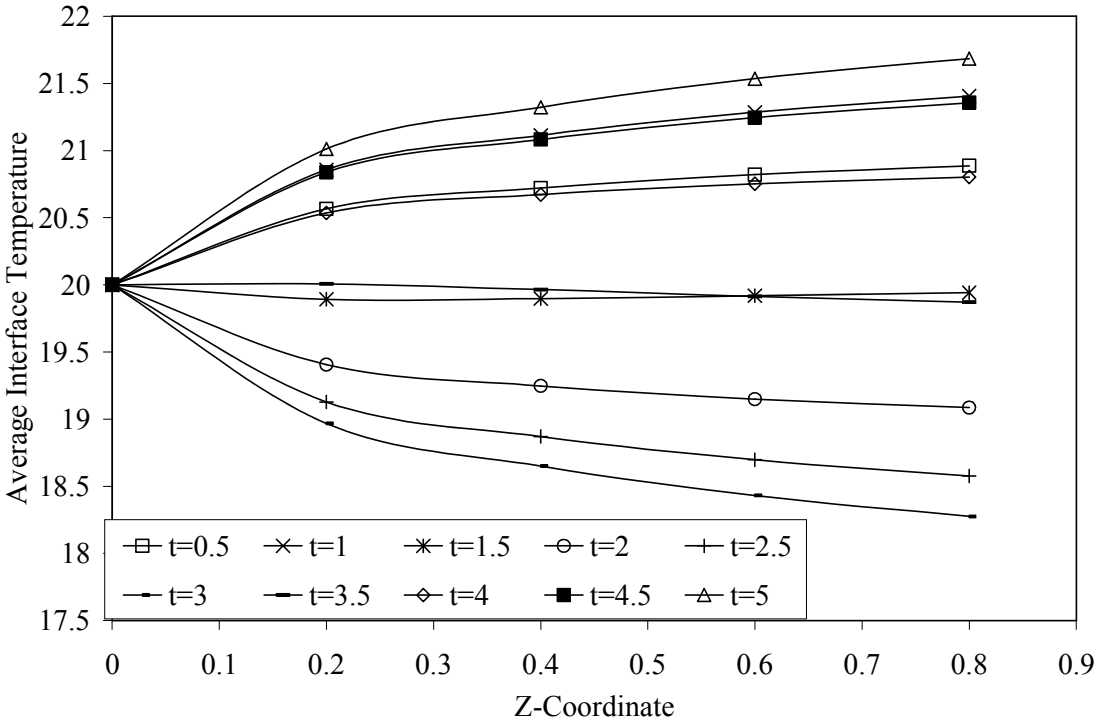

Figure 4.23 Peripheral average interface temperature at different axial locations for different time periods for G = 2 T (Re = 2000, H_{fl} = 0.03 cm).

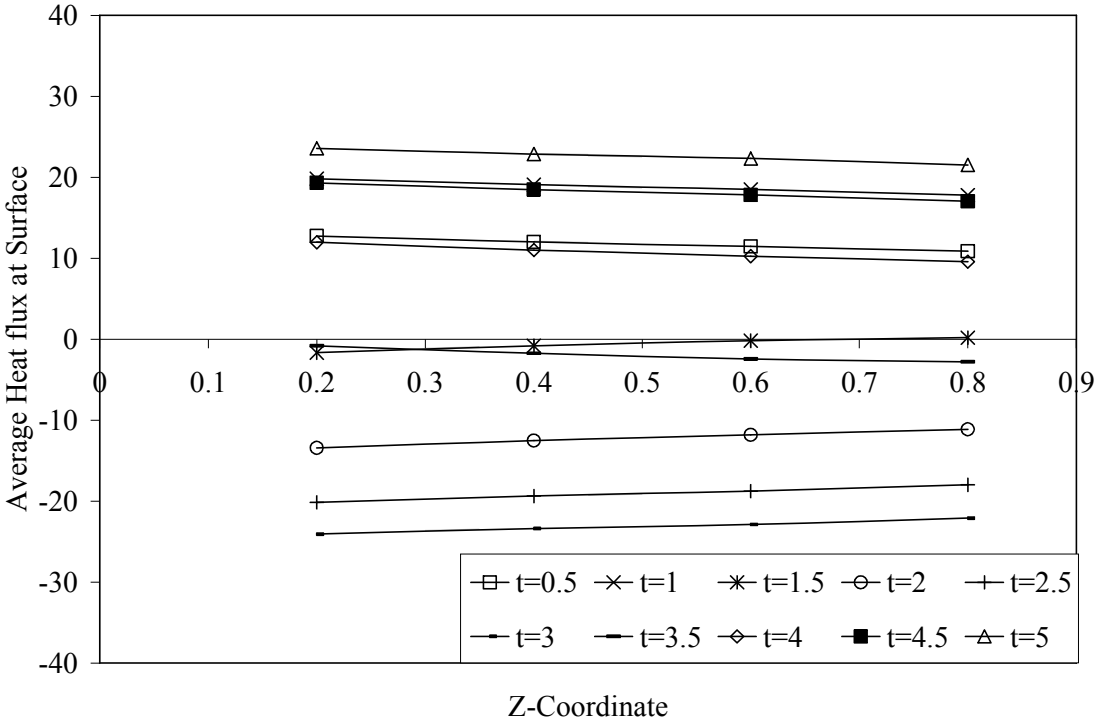

Figure 4.24 Average heat flux at surface at different axial locations for different time periods for G = 2 T (Re = 2000, H_{fl} = 0.03 cm).

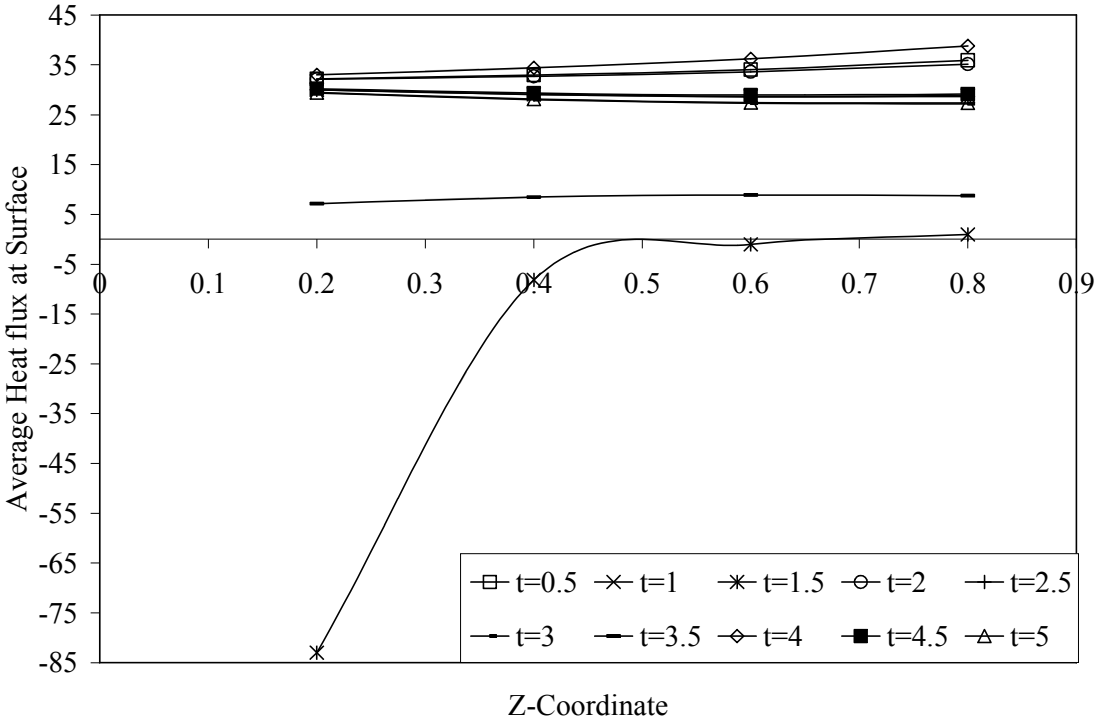

Figure 4.25 Peripheral average Nusselt number at different axial locations for different time periods for G = 2 T (Re = 2000, H_{fl} = 0.03 cm).

Figure 4.25 shows the average Nusselt number at different axial locations for different times with magnetic field alternating between +2 T and -2 T. The change in the magnetic field does not affect the Nusselt number as seen in the previous case where the magnetic field was alternating between +10 T and -10 T. The figure shows very close results to those of the base case and also the previous case.

4.3.3 Size of the microchannel

Now we keep the Reynolds number, the magnetic field same as the base case and vary the height of the trapezoidal microchannel from 0.03cm to 0.02cm (300 μm to 200 μm). Figures 4.26 to 4.27 show the effect of using smaller channel height on the heating and cooling performance of the trapezoidal microchannel system. Figure 4.26 shows the bulk temperature at different axial locations for different times for H_{fl} = 0.02 cm. Compared to figure 4.6, the interface temperature is a little higher for smaller channel height. This is because smaller channel with same Reynolds number have higher axial velocity which enhances the convection heat transfer to the fluid. This result is higher interface temperatures during the heating process and lower interface temperature during the cooling process as seen in figure 4.27, and thus the bulk temperature is higher during heating process and lower during the cooling process when compared to the base case. The value of heat flux is higher for smaller channels as shown in figure 4.28. This is because the temperature gradient in the solid is higher due to higher fluid velocity.

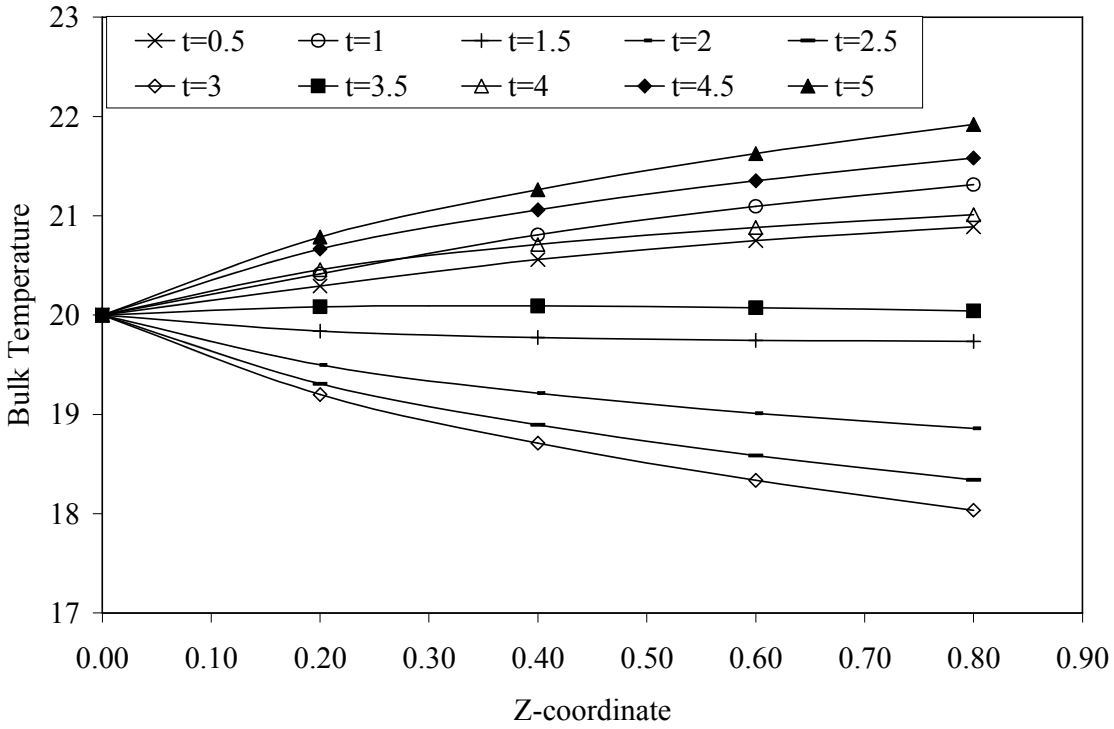

Figure 4.26 Bulk temperature at different axial locations for different time periods for H_{fl} = 0.02 cm (Re = 2000, G = 5 T).

Figure 4.29 shows the average Nusselt number at different axial locations for different times at the fluid-solid interface with H_{fl} = 0.02 cm. It shows more irregular Nusselt number than the base case. When the heating process takes over, the solid has higher temperature than the interface. When the cooling process takes place the interface temperature becomes higher than the solid. This switch between values takes place at the beginning of every time period, t=1.5 sec for the heating phase and t=3.5 sec. for the cooling phase. Higher fluid velocity that enhances the heat flow rate and results in earlier temperature gradient switch in the solid might be the reason behind the reason for having low Nusselt numbers. Compared to the original case, Nusselt number is lower with smaller channel height.

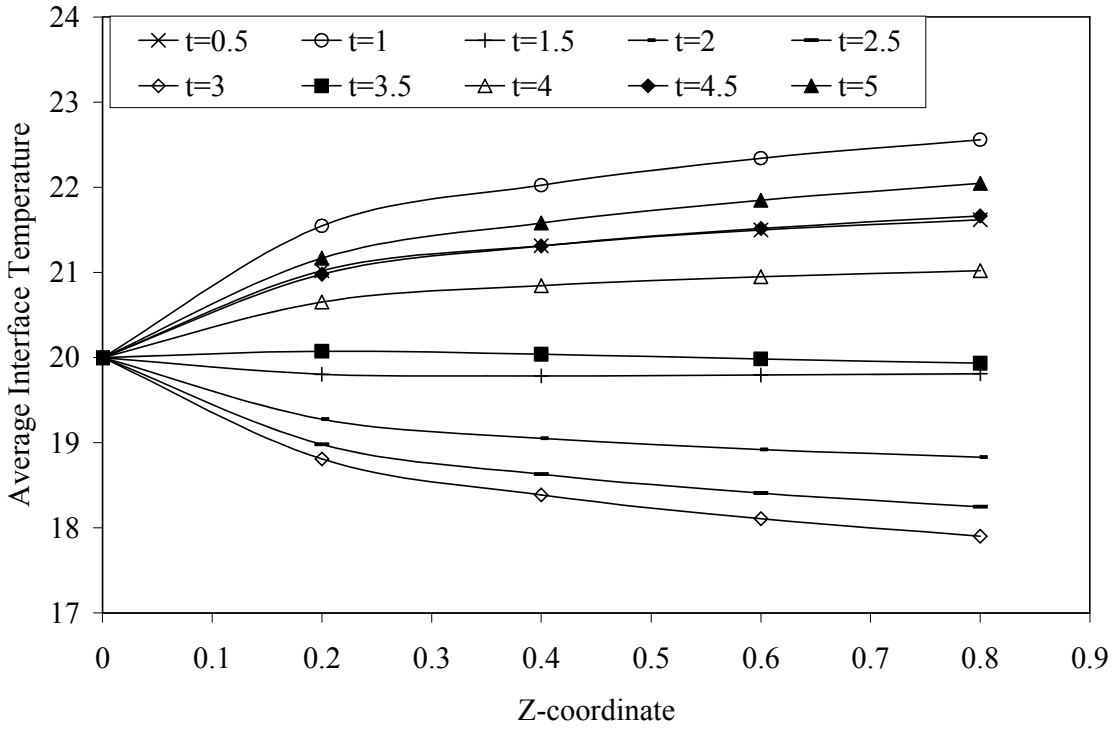

Figure 4.27 Peripheral average interface temperature at different axial locations for different time periods for H_{fl} = 0.02 cm (Re = 2000, G = 5 T).

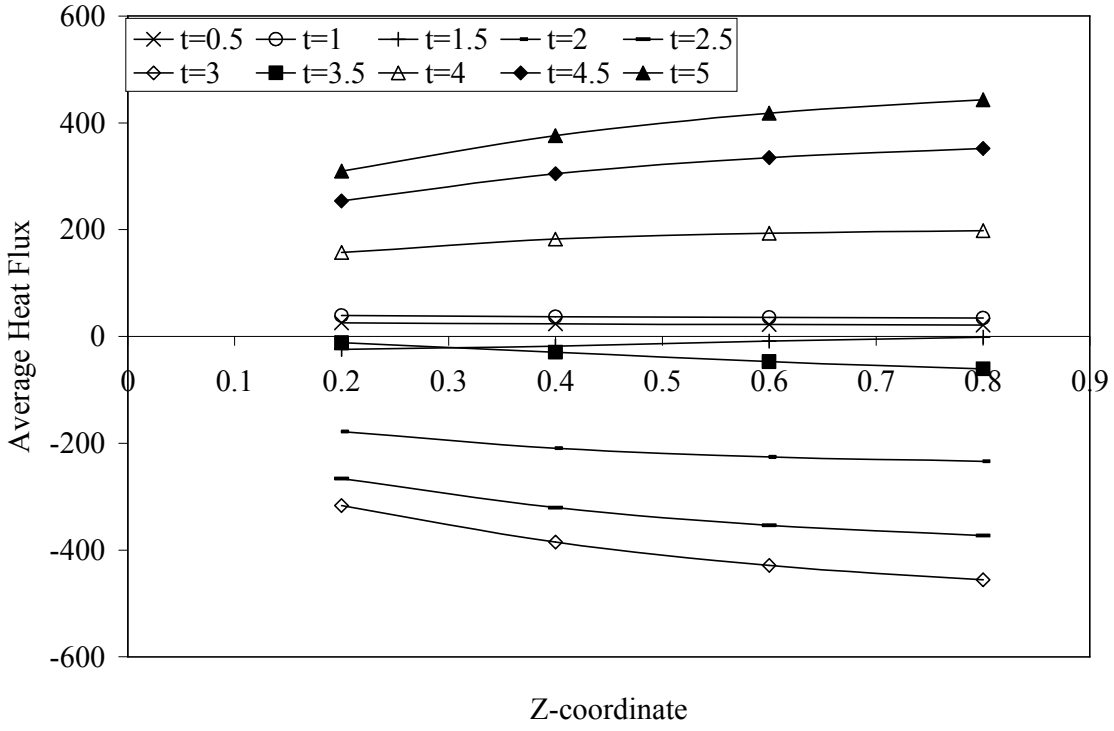

Figure 4.28 Average heat flux at surface at different axial locations for different time periods for H_{fl} = 0.02 cm (Re = 2000, G = 5 T).

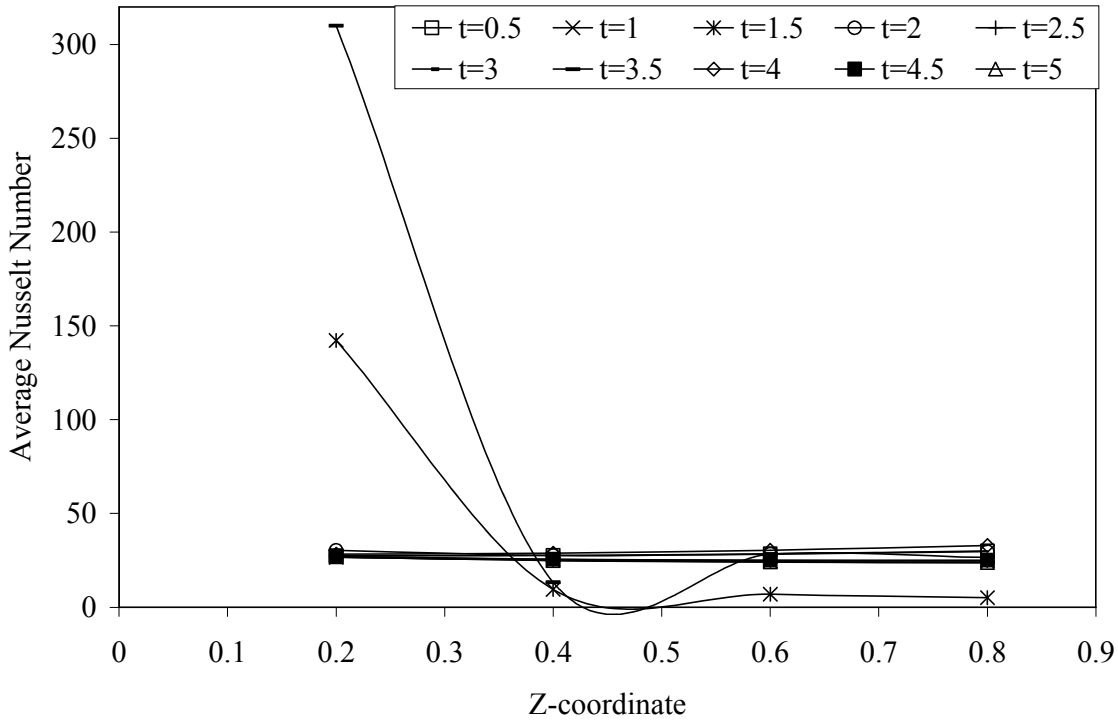

Figure 4.29 Peripheral average Nusselt number at different axial locations for different time periods for H_{fl} = 0.02 cm (Re = 2000, G = 5 T).

Now we change the width of micro channel from 0.15 cm to 0.13 cm and all other parameters are kept constant from the base case. Here figures 4.30 and 4.31 show the variation of bulk temperature and average interface temperature at different axial locations for different times for W_{fl} = 0.13 cm. Here we see that there is a slight reduction in the value of maximum and minimum average interface temperatures attained compared to the base case. The same behavior is seen in the case of the variation of heat flux also as shown in figure 4.32. This is due to the fact the hydraulic diameter is varied and the Reynolds number is kept constant for which the inlet velocity of the fluid is higher and hence the cause of the above mentioned behavior. Figure 4.33 shows the average Nusselt number at different axial locations for different times at the fluid-solid

interface with W_{fl} = 0.13 cm. The maximum value reached in this case is lower than that of in the base case.

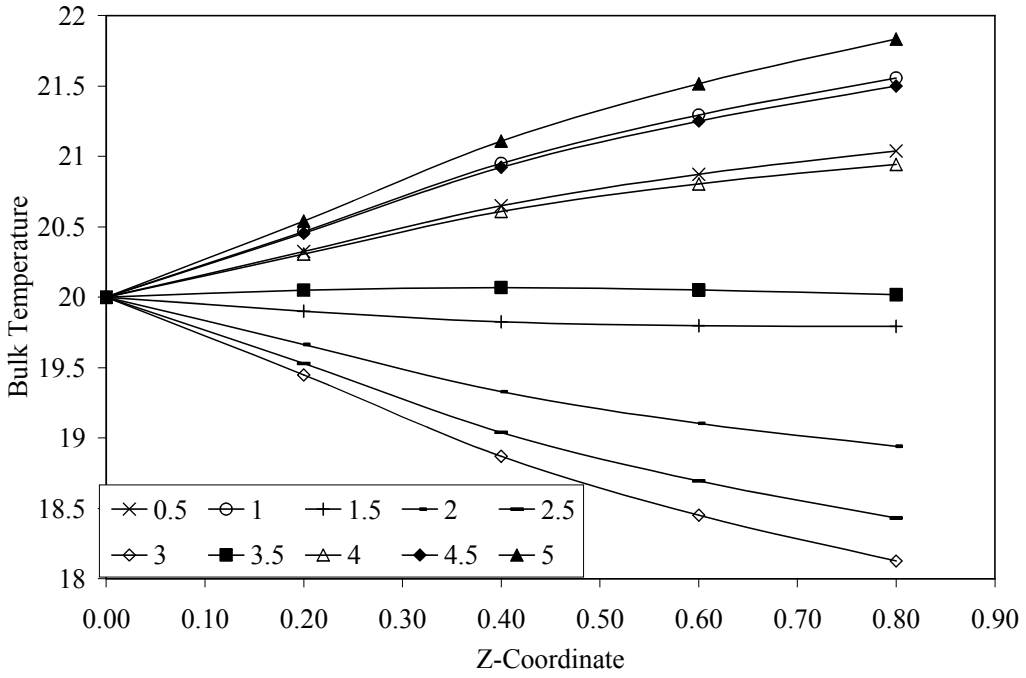

Figure 4.30 Bulk temperature at different axial locations for different time periods for H_{fl} = 0.13 cm (Re = 2000, G = 5 T).

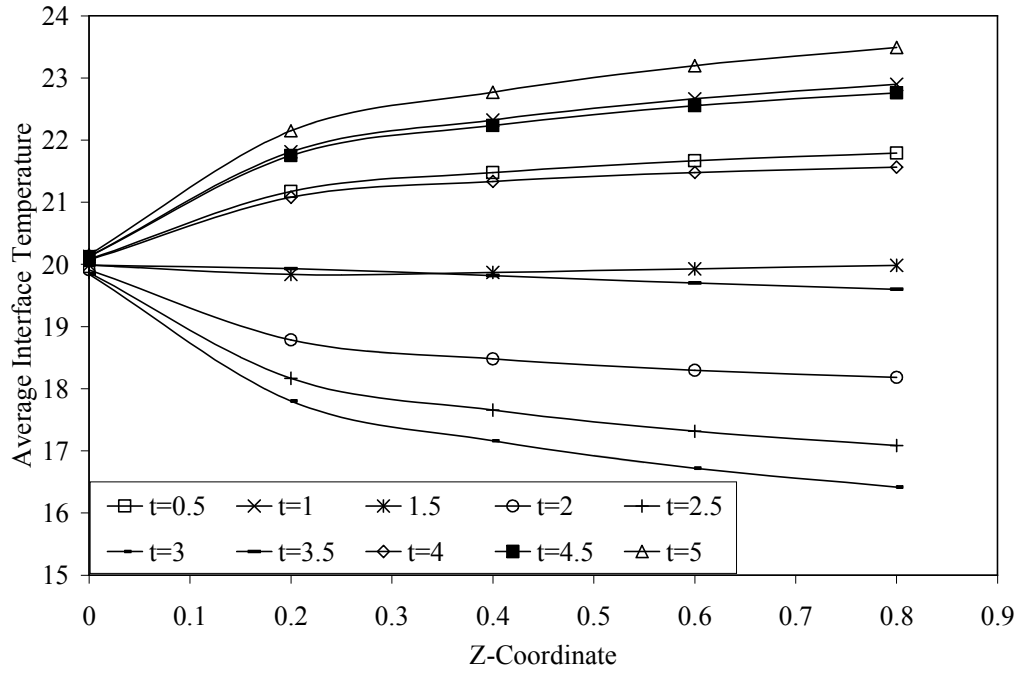

Figure 4.31 Peripheral average interface temperature at different axial locations for different time periods for H_{fl} = 0.13 cm (Re = 2000, G = 5 T).

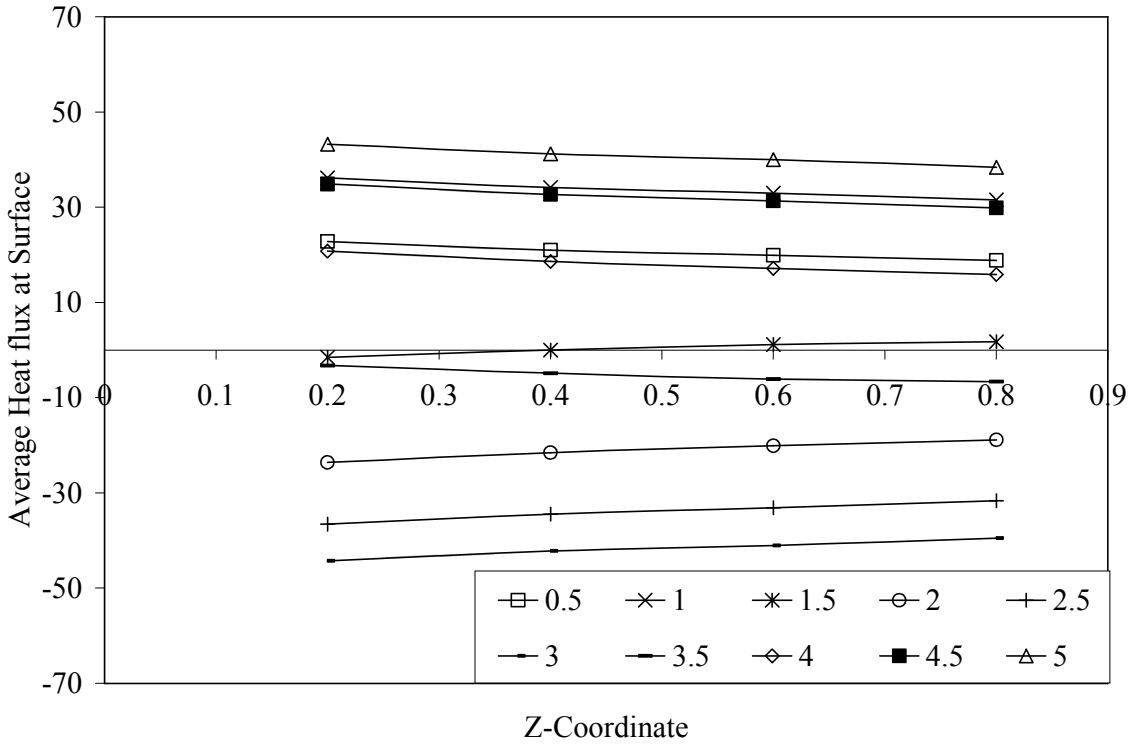

Figure 4.32 Average heat flux at surface at different axial locations for different time periods for H_{fl} = 0.13 cm (Re = 2000, G = 5 T).

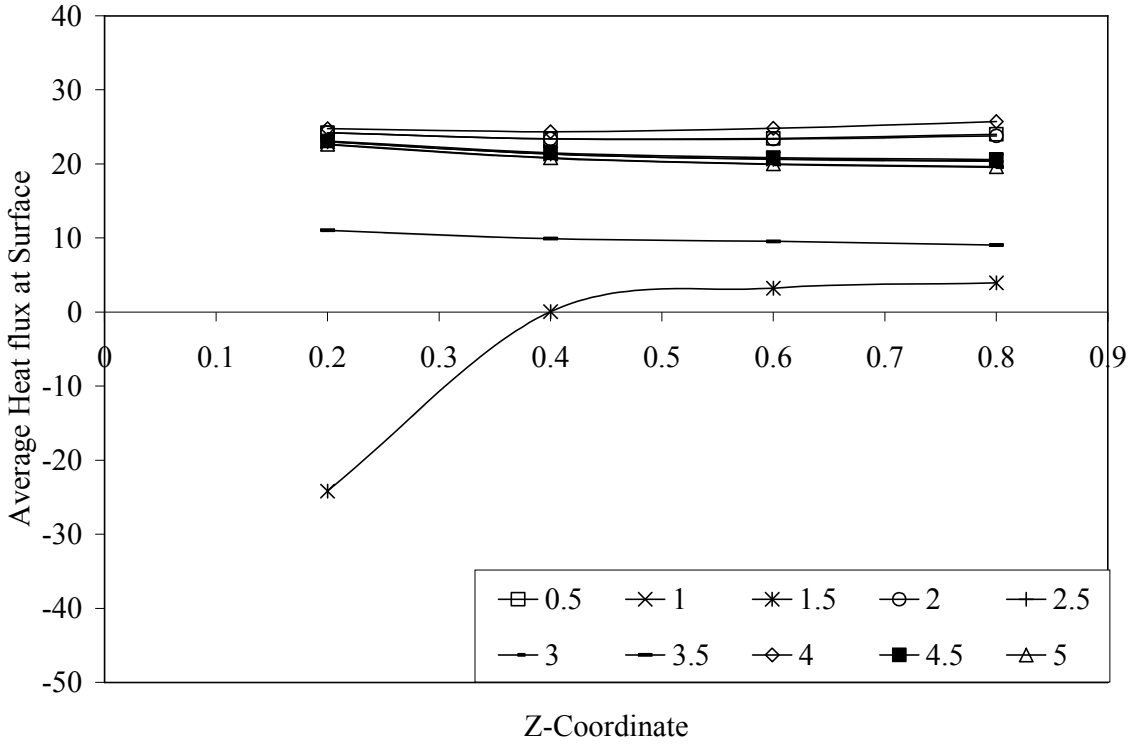

Figure 4.33 Peripheral average Nusselt number at different axial locations for different time periods for W_{fl} = 0.13 cm (Re = 2000, G = 5 T).

4.3.4 Working fluid

All the above results were obtained with water as the working fluid which as a Prandtl number of 7 now we change the working fluid to a fluid which has a Prandtl number lesser than 7, refrigerant R=134a (Pr = 4.8). The Reynolds number was kept at the same value as in the base case which was 2000 and the applied magnetic field was also kept constant at 5 T and the inlet temperature of the fluid was changed to -30^{o}C. Figures 4.34 and 4.35 show the variation of bulk temperature and average interface temperature at the fluid-gadolinium interface different axial locations for different times for working fluid R-134a. Here we see temperature variation is different when compared to the previous cases, this can be explained by the fact that the inlet temperature is much lesser than in the case of water. Hence we see that in first time period there is a steady decrease in temperature at the wall and in the second time period that is when the cooling takes place, there is a drastic decrease in the temperature to a value just greater than that of the inlet temperature. Again the temperature increases due to the heating cycle, in the next time period. Then again similar trend is seen in the case of the average heat flux as seen in figure 4.36.

Figure 4.37 shows the variation of average Nusselt number variation different location along the length of the microtube for various times. The average value of Nusselt number is lower that that of in the case of water which can be explained as the Prandtl number effect as R-134a has a lower Prandtl number than that of water.

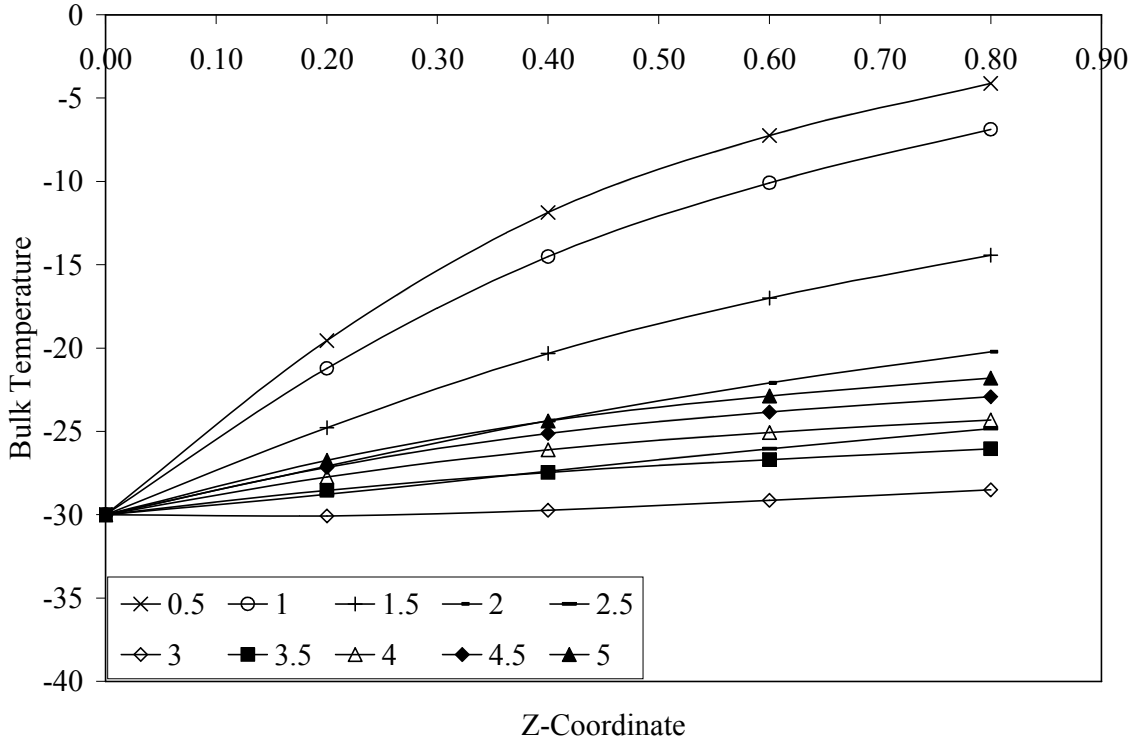

Figure 4.34 Bulk temperature at different axial locations for different time periods for R-134a (Re = 2000, G = 5 T).

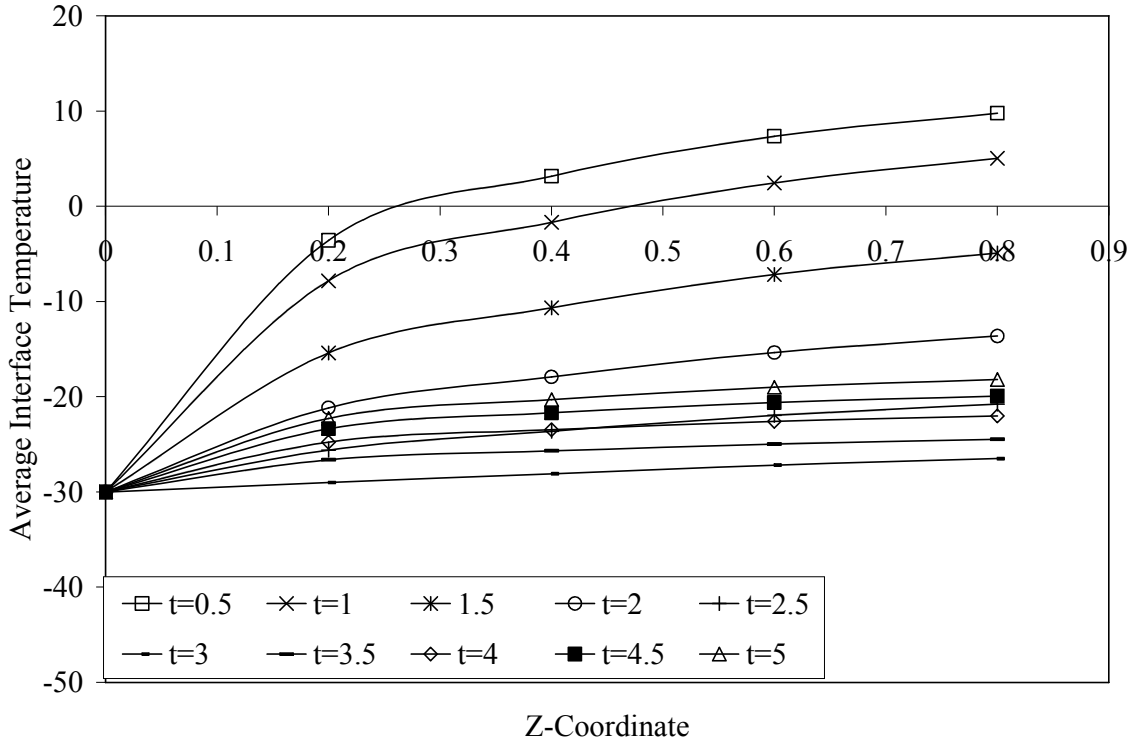

Figure 4.35 Peripheral average interface temperature at different axial locations for different time periods for R-134a (Re = 2000, G = 5 T).

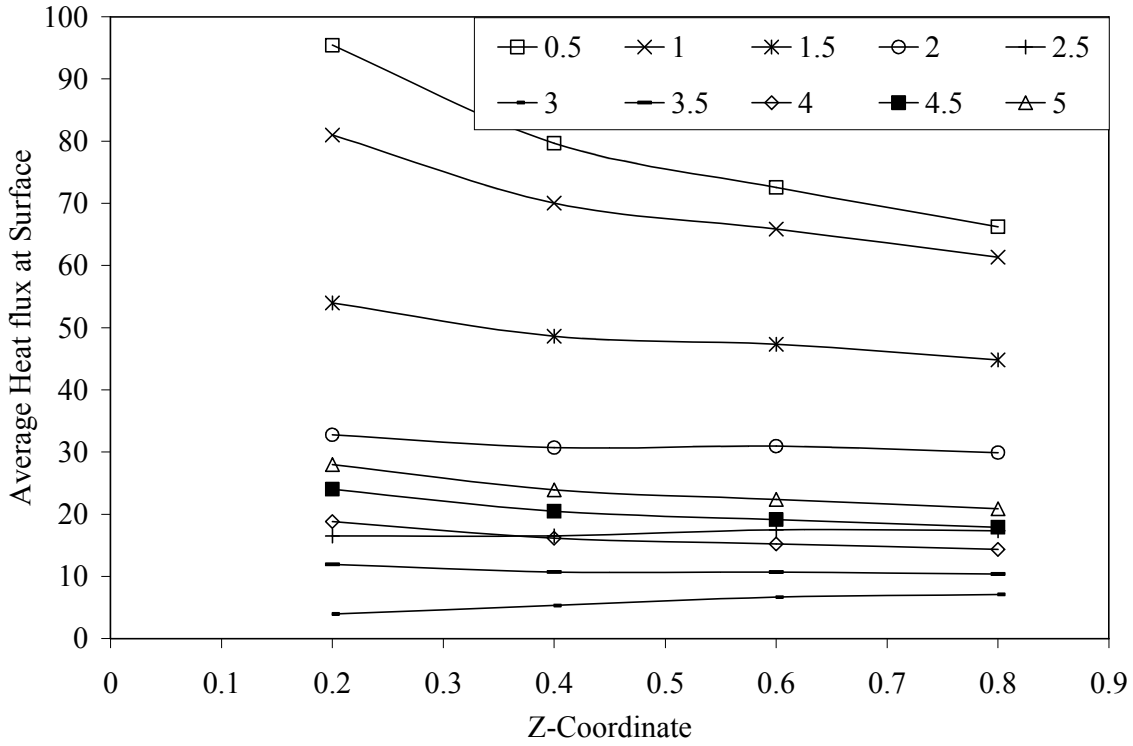

Figure 4.36 Average heat flux at surface at different axial locations for different time periods for R-134a (Re = 2000, G = 5 T).

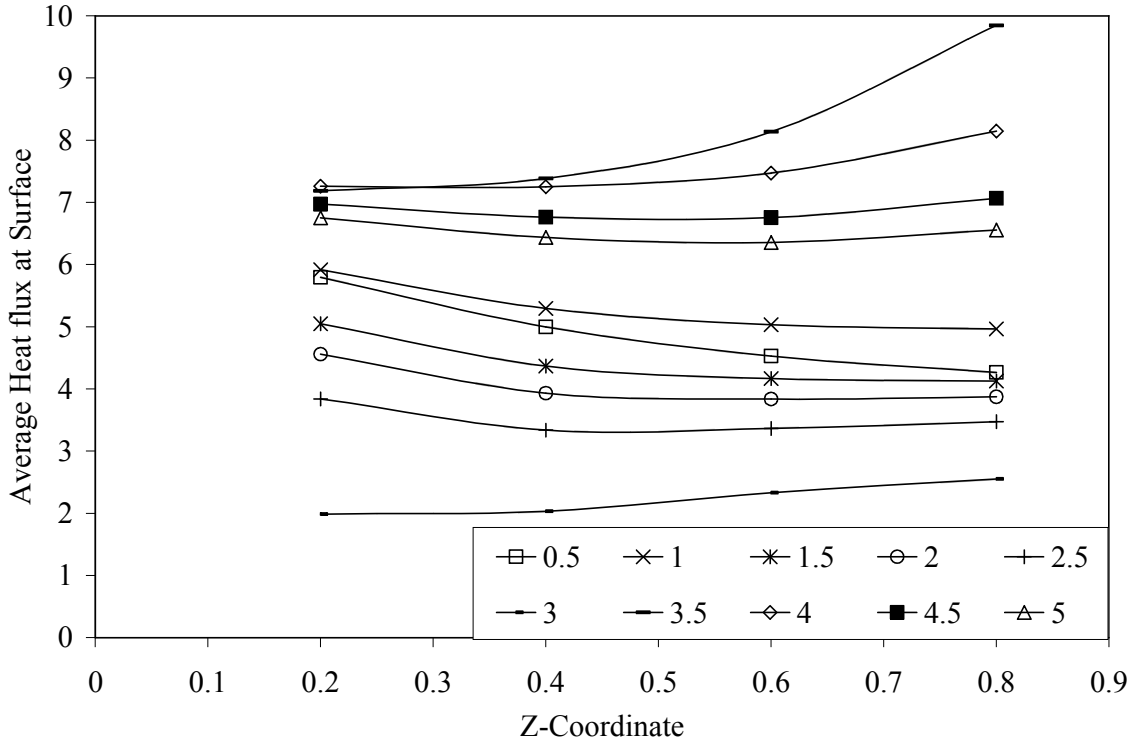

Figure 4.37 Peripheral average Nusselt number at different axial locations for different time periods for R-134a (Re = 2000, G = 5 T).

Chapter 5 Conclusions and Recommendations

5.1 Conclusions

Different types and designs of microchannels were studied in this project. Transient as well as steady state cases with different boundary conditions were implemented in this study to understand the microchannel cooling performance under different conditions and designs. Numerical simulation models were developed for this project with the desired designs and boundary conditions. Computer software was used to solve the conservation equations for the velocity and temperature distribution.

5.1.1 Analysis of convection around a restricted flow passage in a microchannel

The effects of flow restriction on the local and global heat transfer coefficient have been investigated for circular microtube and two-dimensional microchannel. The Nusselt number is sensitive to both the geometry of the duct and the restriction. For a rectangular restriction, we noticed a large increase in local Nusselt number value at the beginning of the restriction due to the start of a new thermal boundary layer. For other restriction shapes, a gradual increase in Nusselt number along the restriction happens until minimum flow area is reached and then a gradual decrease happens further downstream. When the height of the restriction was increased the value of local Nusselt Number at the start of the restriction also increased. Compared to water, refrigerant R-134a (which has lower Prandtl number) yielded a lower value of both local as well as

global Nusselt number. In the circular tube with restriction case we noticed a reduction in global Nusselt number when compared to the smooth tube. The single restriction configuration has the lowest average Nusselt number value when compared to the three restriction and the five restriction configurations for the microtube. On the other hand, in the two-dimensional microchannel case we noticed an increase in global value of Nusselt number when compared to the smooth microchannel. The single restriction configuration has the highest global value of Nusselt number when compared to the three and five restriction configurations in microchannels. The pumping power required for the five restriction case is the largest and the values for that of the three restrictions case is less than that and greater than that of the single restriction cases. The computed results compared well with the previous studies. Flow restrictions can be conveniently used to enhance local heat transfer rate even though the global performance of the device may enhance or diminish based on geometry and flow conditions.

5.1.2 Protrusions in a microtube for conjugate heat transfer with uniform or discrete heating

Effects of obstructions on the heat transfer in microtubes and microchannels of size of 700 μm were investigated. The Nusselt number is sensitive to the wall thickness, the shape, and size of the obstruction. For a rectangular protrusion, we noticed a sudden jump in local Nusselt number value at the beginning of the obstruction due to the start of a new thermal boundary layer when the heat flux was applied at the location of the protrusion, the jump in local Nusselt number was lesser when the heat flux was applied away from the protrusion. For other protrusion shapes, a gradual increase in Nusselt number along the obstruction happens until minimum flow area is reached and then a gradual decrease happens further downstream. When the height of the protrusion was

increased the value of local Nusselt Number at the start of the obstruction also increased. The same trend was seen in the case of microchannel, but the value of the Nusselt number is relatively higher that that observed in the microtube. As the thickness of the wall is increased the jump in the local Nusselt number also decreases due to the distance traveled by the heat is larger which causes the temperature gradient at the inner wall i.e. the solid-fluid interface to be lower than in case II causing the reduction in the value of local Nusselt number. Similar trend of the reduction of local Nusselt number was observed when the working fluid was changed from water to low Prandtl number fluid refrigerant R-134a. In the circular microtube with obstruction case we noticed a reduction in average Nusselt number when compared to the smooth tube. The single protrusion configuration has the lowest average Nusselt number value when compared to the three protrusion and the five protrusion configurations for the micro tube. On the other hand, in the two-dimensional microchannel case we noticed an increase in global value of Nusselt number when compared to the smooth microchannel. As the Reynolds number increases we notice a decrease in C_f. Among the single protrusion cases the triangular protrusion has the highest value, and five protrusion configuration has the highest values of all the configurations for both C_f. and required pumping power. The pumping power required for the five restriction case is the largest and the values for that of the three restrictions case is less than that and greater than that of the single restriction cases. In the single restriction case we see that with increase in Reynolds number the percentage increase in the pumping power required is quite drastic. We also observe that at lower Reynolds numbers we the percentage increase in average Nusselt number is larger that that of the percentage increase in the required pumping power. But at higher the percentage increase

in the required pumping power becomes much larger than the augmentation see in heat transfer.

5.1.3 Transient heat transfer in trapezoidal microchannels under time varying heat source

The transient heat transfer for laminar flow inside a trapezoidal microchannel embedded in a rectangular substrate with time varying heat generation due to magnetic field was investigated. The Nusselt number was higher when the Reynolds number was decreased. The average peripheral interface temperature was higher when the magnetic field was increased but the Nusselt number value did not vary. The average peripheral interface temperature was lower when the magnetic field was decreased. With decrease in the channel height and width there was an increase in the average Nusselt number in the channel. When the R-134a was used as the working fluid which has a lower Prandtl number the average value of Nusselt number was lower that that of in the case of water.

5.2 Recommendations for Future Research

Researchers could continue studying different designs for microchannels. Other channel geometries or parameters that are not included in this work could be good material for future studies. Only one composite material was studied in this work. There are many other combinations of other composite material and design that could be used in an effort to find the optimum design. Steady state parametric study was done on the effect of restrictions/protrusions in microtubes and two-dimensional microchannels. Transient problem was not considered for this research as well as other solids and working fluids could be considered. The Reynolds numbers which were considered were in the laminar region, turbulent convective heat transfer can be included in future studies.

References

[1] Morini, G.L., "Single-phase convective heat transfer in microchannels: a review of experimental results," *International Journal of Thermal Science*, Vol. 43, 2004, pp. 631-651.

[2] Kandlikar, S.G., and Grande, W.J., "Evolution of microchannel flow passages-thermohydraulic performance and fabrication technology," *Heat Transfer Engineering*, Vol. 24, 2003, pp. 3-17.

[3] Adams, T.M., Abdel-Khalik, S.I., Jeter, S.M., Qureshi, Z.H., "An experimental investigation of single-phase forced convection in microchannels," *International Journal of Heat and Mass Transfer*, Vol. 41, 1998, pp. 851-857.

[4] Owhaib, and W, Palm B, "Experimental investigation of single phase convective heat transfer in circular microchannels", *Experimental Thermal Fluid Science*, Vol. 28, 2004, pp. 105-110.

[5] Guo, Z-Y., and Li, Z-X., "Size effect on microscale single-phase flow and heat transfer," *International Journal of Heat and Mass Transfer*, Vol. 46, 2003, pp. 149-159.

[6] Harms, T.M., Kazmierczak, and M., Gerner, F.M., "Developing convective heat transfer in deep rectangular microchannels," *International Journal of Heat and Fluid Flow*, Vol. 20, 1999, pp. 149-157.

[7] Quadir, G.A., Mydin. A., and Seetharamu, K.N., "Analysis of microchannel heat exchangers using FEM," *International Journal of Numerical Methods for Heat and Fluid Flow*, Vol. 11, 2001, pp. 59-75.

[8] Bendib, S., and Olivier, F., "Analytical study of microchannel and passive microvalve application to micropump simulator," *SPIE*, Vol. 4593, 2001, pp. 283-291.

[9] Tunc, G., and Bayazitoglu, Y., "Heat transfer in micro channels," *International Journal of Heat and Mass Transfer*, Vol. 45, 2002, pp. 765-773.

[10] Kroeker, C.J., Soliman, H.M., and Ormiston, S.J., "Three-dimensional thermal analysis of heat sinks with circular cooling micro-channels," *International Journal of Heat and Mass Transfer*, Vol. 47, 2004, pp. 4733-4744.

[11] Lelea, D., Nisho, S., and Takano, K., "The experimental research on microtube heat transfer and fluid flow of distilled water," *International Journal of Heat and Mass Transfer*, Vol. 47, 2004, pp. 2817-2830.

[12] Liu, J-T., Peng, X-F., and Yan, W-M., "Numerical study of fluid flow and heat transfer in microchannel cooling passages," *International Journal of Heat and Mass Transfer*, Vol. 50, 2007, pp. 1885-1864.

[13] Chen, Y-M., and Wang, K-C, "Experimental study on forced convective flow in a channel with heated blocks in tandem," *Experimental Thermal and Fluid Science*, Vol. 16,1998, pp. 286-298.

[14] Mahapatra, T.R., Layek, G.C., and Maiti, M.K., "Unsteady laminar separated flow through constricted channel," *International Journal of Non-Linear Mechanics*, Vol. 37, 2002, pp. 443–454.

[15] Chang, C-C., and Yang, R-J., "Computational analysis of electrokinetically driven flow mixing in microchannels with patterned blocks," *Journal of Micromechanics and Microengineering*, Vol. 14, 2004, pp. 550-558.

[16] Lee, P-S., and Garimella, S.V., "Hot-spot thermal management with flow modulation in a microchannel heat sink," *Proceedings of 2005 ASME International Mechanical Engineering Congress and Exposition Orlando FL American Society of Mechanical Engineers*. NY US.

[17] Korichi, A., and Oufer, L., "Numerical heat transfer in rectangular channel with mounted obstacles on upper and lower walls," *International Journal of Thermal Sciences*, Vol. 44, 2005, pp. 644-655.

[18] Croce, G., and D'Agaro, P., "Numerical simulation of roughness effect on microchannel heat transfer and pressure drop in laminar flow," *Journal of Physics D: Applied Physics*, Vol. 38, 2005, pp. 1518-1530.

[19] Lee, P-S., Garimella, S.V. and Liu, D., "Investigation of heat transfer in rectangular microchannels, *International Journal of Heat and Mass Transfer*," Vol. 48, 2004, pp. 1688-1704.

[20] Pfund, D., Rector, D., Shekarriz, A., Popescu, A., and Welty, J., "Pressure drop measurements in microchannel," *AIChE Journal*, Vol. 46, 2000, pp. 1496-1507.

[21] Rahman, M.M., "Measurements of heat transfer in microchannel heat sinks," *International Communications in Heat and Mass Transfer*, Vol. 27, 2000, pp. 495-506.

[22] Ambatipudi, K.K., and Rahman, M.M., "Analysis of conjugate heat transfer in microchannel heat sinks," *Numerical Heat transfer, Part A*, Vol. 37, 200, pp. 711-731.

[23] Qu, W., Mala, G.M., and Li, D., "Heat Transfer for water flow in trapezoidal silicon microchannels," *International Journal of Heat and Mass Transfer*, Vol. 43, no. 21 2000, pp. 3925-3936.

[24] Fedorov, A. G., and Viskanta, R., "Three-dimensional conjugate heat transfer in the microchannel heat sink for electronic packaging," *International Journal of Heat and Mass Transfer*, Vol. 43, 2000, pp. 399-415.

[25] Celata, G. P., Cumo, M., and Zummo, G., "Thermal-hydraulic characteristics of single-phase flow in capillary pipes," *Experimental Thermal and Fluid Science*, Vol. 28, 2004, pp. 87-95.

[26] Van Male, P., de Croon, M.H.J.M., Tiggelaar, R.M., Van den Berg, A., and Schouten, J.C., "Heat and mass transfer in a square microchannel with asymmetric heating," *International Journal of Heat and Mass Transfer*, Vol. 47, 2004, pp. 87-99.

[27] Rao, P.S.C., Rahman, M.M., and Soliman, H. M., "Numerical simulation of steady-state conjugate heat transfer in circular microtube inside a rectangular substrate," *Numerical Heat Transfer, Part A*, Vol. 49, 2006, pp. 635-654.

[28] Nilson, R., Tchikanda, S., Griffiths, S., and Martinez, M., "Steady state evaporating flow in rectangular microchannels," *International Journal of Heat and Mass Transfer*, Vol. 49, 2006, pp. 1603-1608.

[29] Kim, D.K., and Kim, S.J., "Average approach for microchannel heat sinks subject to the uniform wall temperature condition," *International Journal of Heat and Mass Transfer*, Vol. 49,, 2006, pp. 695-706.

[30] Ji, L., and Peterson, G.P., "Geometric optimization of a micro heat sink with liquid flow," *IEEE Transactions on Components and Packaging Technologies*, Vol. 29, 2006, pp. 145-154.

[31] Celata, G.P., Cumo, M., Marconi, V., McPhail, S.J., and Zummo, G., "Microtube liquid single-phase heat transfer in laminar flow," *International Journal of Heat and Mass Transfer*, Vol. 49, 2006, pp. 3538-3546.

[32] Shevade, S.S., and Rahman, M.M., "Heat transfer in rectangular microchannels during volumetric heating of the substrate," *International Communications in Heat and Mass Transfer*, Vol. 34, 2007, pp. 661-672.

[33] Yang, R-J., Wu, C-H., Tseng, T-I., Huang, S-B., and Lee, G-B., "Enhancement of electrokinetically-driven flow mixing in microchannel with added side channels," *Japanese Journal of Applied Physics*, Vol. 44, no. 10, 2005, pp. 7634-7642.

[34] Shen, S., Xu, J., Zhou, J., and Chen, Y., "Flow and heat transfer in microchannels with rough wall surface," *Energy Conversion and Management*, Vol. 47, 2006, pp. 1311-1325.

[35] Hibara, A., Iwayama¸ S., Matsuoka, S., Ueno, M., Kikutania, Y., Tokeshi, M., and Kitamori, T., "Surface modification method of microchannels for gas-liquid two-phase flow in microchips," *Analytical Chemistry*, Vol. 77, no. 3, 2005, pp. 943-947.

[36] Peng, X. F., and Peterson, G. P., "Convective Heat Transfer and Flow Friction for Water Flow in Microchannel Structures," *International Journal of Heat and Mass Transfer*, Vol. 39, 1996, pp. 2599-2608.

[37] Papautsky, I., Gale, B., Mohanty, S., Ameel, T., and Frazier B., "Effects of Rectangular Microchannel Aspect Ratio on Laminar Friction Constant," *Proceedings of SPIE, The Int. Society of Optical Engineering*, Vol. 3877, 1999, pp. 147-158.

[38] Rahman, M.M., and Shevade, S.S., "Flow in Microchannel with Time Varying Heat Source," *Proceedings of IMECE, ASME International Mechanical Engineering Congress and Exposition*, Washington, D. C., November 16-21, 2003.

[39] Kohl, M.J., Abdel-Khalik, S I., Jeter, S.M., and Sadowski, D.L., "An Experimental Investigation of Microchannel Flow with Internal Pressure Measurements," *International Journal of Heat and Mass Transfer*, Vol. 48, 2005, pp. 1518-1533.

[40] Koo, J., and Kleinstreuer, C., "Viscous Dissipation Effects in Microtubes and Microchannels," *International Journal of Heat and Mass Transfer*, Vol. 47, No. 14/16, 2004. pp. 3159-3169.

[41] Rahman, M.M., and Shevade, S.S., "Fluid Flow and Heat Transfer in a Composite Trapezoidal Microchannel," *2005 ASME Summer Heat Transfer Conference*, San Francisco, California, July 17-22, 2005.

[42] Rao, P.S.C., and Rahman, M.M., "Transient conjugate heat transfer model for circular tubes inside a rectangular substrate," *Journal of Thermophysics and Heat Transfer*, vol. 20, pp. 122-134, 2006.

[43] Ozisik, M.N., 1993, *Heat Conduction*, 2nd ed., John Wiley and Sons, Inc, New York, USA.

[44] Kays, W.M., Crawford, M.E., and Weigand, B., 2005, *Convection Heat and Mass Transfer*, 4th ed., McGraw-Hill, Inc, New York, USA.

[45] Incropera, F.P., Dewitt, D.P., Bergman, T.L., and Lavine, A.S., 2007, *Fundamentals of Heat and Mass Transfer*, 6th ed., John Wiley and Sons, Inc, New York, USA.

Appendices

Appendix A: FIDAP Program for Analysis of Convection Around a Restricted Flow Passage in a Microchannel

```
FIPREP
PROBLEM( AXI-SYMMETRIC, NONL, ENERGY, MOMENTUM )
PRESSURE( MIXED, DISC )
SOLUTION( N.R. = 100, VELC = 0.000001, RESC = 0.000001, ACCF = 0.5 )
/
EXECUTION( NEWJ )
DATAPRINT( NONE )
PRINTOUT( NONE )
OPTIONS( UPWI )
POSTPROCESS( RESIDUAL )
/
DENSITY( SET = 1, CONS = 1 )
SPECIFICHEAT( SET = 1, CONS = 1 )
CONDUCTIVITY( SET = 1, CONS = 0.00143 )
CONDUCTIVITY( SET = 2, CONS = 0.5664 )
VISCOSITY( SET = 1, CONS = 0.01 )
/
ENTITY( NAME = "fluid", FLUID, PROP = "1" )
/ENTITY( NAME = "solid", SOLID, PROP = "2" )
ENTITY( NAME = "inlet", PLOT )
ENTITY( NAME = "wall", PLOT )
ENTITY( NAME = "outlet", PLOT )
ENTITY( NAME = "sym", PLOT )
ENTITY( NAME = "sub", PLOT )
/
BCNODE( UX, ENTI = "inlet", CONS = 28.6 )
BCNODE( UY, ENTI = "inlet", ZERO )
BCNODE( VELO, ENTI = "wall", ZERO )
BCNODE( TEMP, ENTI = "wall", CONS = 40 )
BCNODE( TEMP, ENTI = "inlet", CONS = 20 )
BCNODE( UY, ENTI = "sym", ZERO )
/
CLIPPING( ADD, MAXI )
   0,    0,    0,    0,   40,    0
CLIPPING( ADD, MINI )
   0,    0,    0,    0,   20,    0
/
END
CREATE( FISO )
RUN( FISOLV, BACK )
```

Appendix B: FIDAP Program for Effects of Protrusions in a Microchannel for Conjugate Heat Transfer with Uniform or Discrete Heating

```
FIPREP
PROBLEM( AXI-SYMMETRIC, NONL, ENERGY, MOMENTUM )
PRESSURE( MIXED, DISC )
SOLUTION( N.R. = 100, VELC = 0.000001, RESC = 0.000001, ACCF = 0.5 )
//
EXECUTION( NEWJ )
DATAPRINT( NONE )
PRINTOUT( NONE )
OPTIONS( UPWI )
POSTPROCESS( RESIDUAL )
/
DENSITY( SET = 1, CONS = 1 )
SPECIFICHEAT( SET = 1, CONS = 1 )
CONDUCTIVITY( SET = 1, CONS = 0.00143 )
VISCOSITY( SET = 1, CONS = 0.01 )
CONDUCTIVITY( SET = 2, CONS = 0.5664 )
DENSITY( SET = 2, CONS = 2.707 )
/
ENTITY( NAME = "fluid", FLUID, PROP = "1" )
ENTITY( NAME = "solid", SOLID, PROP = "2" )
ENTITY( NAME = "inlet", PLOT )
ENTITY( NAME = "wall", PLOT )
ENTITY( NAME = "outlet", PLOT )
ENTITY( NAME = "sym", PLOT )
ENTITY( NAME = "surface1", PLOT )
ENTITY( NAME = "surface2", PLOT )
ENTITY( NAME = "surface3", PLOT )
ENTITY( NAME = "surface4", PLOT )
ENTITY( NAME = "surface5", PLOT )
ENTITY( NAME = "sub", PLOT )
/
BCNODE( UX, ENTI = "inlet", CONS = 28.6 )
BCNODE( UY, ENTI = "inlet", ZERO )
BCNODE( VELO, ENTI = "wall", ZERO )
BCFLUX( HEAT, ENTI = "surface1", CONS = 0.047801147 )
/BCFLUX( HEAT, ENTI = "surface2", CONS = 0.047801147 )
BCFLUX( HEAT, ENTI = "surface3", CONS = 0.047801147 )
/BCFLUX( HEAT, ENTI = "surface4", CONS = 0.047801147 )
BCFLUX( HEAT, ENTI = "surface5", CONS = 0.047801147 )
BCNODE( TEMP, ENTI = "inlet", CONS = 20 )
BCNODE( UY, ENTI = "sym", ZERO )
/
```

Appendix B: (Continued)

```
CLIPPING( ADD, MAXI )
   0,    0,    0,    0,   40,    0
CLIPPING( ADD, MINI )
   0,    0,    0,    0,   20,    0
/
END
CREATE( FISO )
RUN( FISOLV, BACK )
```

Appendix C: FIDAP Program for Transient Heat Transfer in Trapezoidal Microchannels Under Time Varying Heat Source

```
FIPREP

/=========================================
/                          MATERIAL PROPERTIES
/=========================================

CONDUCTIVITY( ADD, SET = "si", CONS = 0.29637, ISOT )
DENSITY( ADD, SET = "si", CONS = 2.329 )
SPECIFICHEAT( ADD, SET = "si", CONS = 0.16778 )

CONDUCTIVITY( ADD, SET = "fl", CONS = 0.0014435, ISOT )
DENSITY( ADD, SET = "fl", CONS = 0.9974 )
SPECIFICHEAT( ADD, SET = "fl", CONS = 0.9988 )
VISCOSITY( ADD, SET = "fl", CONS = 0.0098 )

CONDUCTIVITY( ADD, SET = "gd", CONS = 0.0250956, ISOT )
DENSITY( ADD, SET = "gd", CONS = 7.895 )
SPECIFICHEAT( ADD, SET = "gd", CONS = 0.054971 )

/=========================================
/                          ENTITY NAMES
/=========================================

ENTITY( ADD, NAME = "si1", SOLI, PROP = "si" )
ENTITY( ADD, NAME = "si2", SOLI, PROP = "si" )
ENTITY( ADD, NAME = "si3", SOLI, PROP = "si" )
ENTITY( ADD, NAME = "fl", FLUI, PROP = "fl" )
ENTITY( ADD, NAME = "gd", SOLI, PROP = "gd" )

ENTITY( ADD, NAME = "si1-in", PLOT )
ENTITY( ADD, NAME = "si1-out", PLOT )
ENTITY( ADD, NAME = "si1-bot", PLOT )
ENTITY( ADD, NAME = "si1-right", PLOT )
ENTITY( ADD, NAME = "si1-top", PLOT )
ENTITY( ADD, NAME = "si1-left", PLOT )

ENTITY( ADD, NAME = "si2-in", PLOT )
ENTITY( ADD, NAME = "si2-out", PLOT )
ENTITY( ADD, NAME = "si2-bot", PLOT )
ENTITY( ADD, NAME = "si2-right", PLOT )
ENTITY( ADD, NAME = "si2-int", PLOT, ATTA = "fl", NATTA = "si2" )
```

Appendix C: (Continued)

```
ENTITY( ADD, NAME = "si3-in", PLOT )
ENTITY( ADD, NAME = "si3-out", PLOT )
ENTITY( ADD, NAME = "si3-bot", PLOT )
ENTITY( ADD, NAME = "si3-axi", PLOT )
ENTITY( ADD, NAME = "si3-int", PLOT, ATTA = "fl", NATTA = "si3" )

ENTITY( ADD, NAME = "fl-in", PLOT )
ENTITY( ADD, NAME = "fl-out", PLOT )
ENTITY( ADD, NAME = "fl-axi", PLOT )
ENTITY( ADD, NAME = "fl-int", PLOT, ATTA = "fl", NATTA = "gd"  )

ENTITY( ADD, NAME = "gd-in", PLOT )
ENTITY( ADD, NAME = "gd-out", PLOT )
ENTITY( ADD, NAME = "gd-axi", PLOT )
ENTITY( ADD, NAME = "gd-top", PLOT )
ENTITY( ADD, NAME = "gd-left", PLOT )

/=========================================
/                        BOUNDARY CONDITION COMMANDS
/=========================================
BCNODE( ADD, UX, ENTI = "fl-in", ZERO )
BCNODE( ADD, UY, ENTI = "fl-in", ZERO )
BCNODE( ADD, UZ, ENTI = "fl-in", CONS = 403.91)
BCNODE( ADD, TEMP, ENTI = "fl-in", CONS = 20 )

BCNODE( ADD, VELO, ENTI = "si2-int", ZERO )
BCNODE( ADD, VELO, ENTI = "si3-int", ZERO )
BCNODE( ADD, VELO, ENTI = "fl-int", ZERO )
BCNODE( ADD, UX, ENTI = "fl-axi", ZERO )

SOURCE( ADD, HEAT, CONS = 5.12, ENTI = "gd" )

ICNODE( ADD, TEMP, CONS = 20, ENTI = "si1" )
ICNODE( ADD, TEMP, CONS = 20, ENTI = "si2" )
ICNODE( ADD, TEMP, CONS = 20, ENTI = "si3" )
ICNODE( ADD, TEMP, CONS = 20, ENTI = "fl" )
ICNODE( ADD, TEMP, CONS = 20, ENTI = "gd" )
/=========================================
/                        EXECUTION COMMANDS
/=========================================
DATAPRINT( ADD, CONT )
EXECUTION( ADD, NEWJ )
PRINTOUT( ADD, NONE )
```

Appendix C: (Continued)

```
OPTIONS( ADD, UPWI )
PROBLEM( ADD, 3-D, INCO, TRAN, LAMI, NONL, NEWT, MOME, ENER, FIXE,
SING )
SOLUTION( ADD, N.R. = 100, VELC = 0.001)
/
/TIME LENGTH = 1s
TIMEINTEGRATION( ADD, BACK, NSTE = 20, TSTA = 0.0, DT = 0.05, FIXE)
POSTPROCESS( ADD, NBLO = 1, NOPT, NOPA )
5, 20, 5
END
/
CREATE( FISO )
RUN( FISOLV, BACK )
```